Draft version September 11, 2026
Typeset using LaTeX **twocolumn** style in AASTeX7.0.1

SPURS: An Ultra-deep View Inside the Compact, Nitrogen-Enriched Nuclei of Little Red Dots

Mengtao Tang ,[1,2,3] Daniel P. Stark ,[4] Charlotte A. Mason ,[5,6] Zuyi Chen ,[5,6] Tucker Jones ,[7]
Sarah Searle Grannis,[5,6] Peter Senchyna ,[8] Lily Whitler ,[9,10] Keerthi Vasan G. C. ,[8] and
Viola Gelli [5,6]

[1] *Tsung-Dao Lee Institute, Shanghai Jiao Tong University, 1 Lisuo Road, Shanghai 201210, People's Republic of China*
[2] *School of Physics and Astronomy, Shanghai Jiao Tong University, 800 Dongchuan Road, Shanghai 200240, People's Republic of China*
[3] *State Key Laboratory of Dark Matter Physics, Shanghai Jiao Tong University, 1 Lisuo Road, Shanghai 201210, People's Republic of China*
[4] *Department of Astronomy, University of California, Berkeley, Berkeley, CA 94720, USA*
[5] *Cosmic Dawn Center (DAWN)*
[6] *Niels Bohr Institute, University of Copenhagen, Jagtvej 128, 2200 Copenhagen N, Denmark*
[7] *Department of Physics and Astronomy, University of California, Davis, 1 Shields Avenue, Davis, CA 95616, USA*
[8] *The Observatories of the Carnegie Institution for Science, 813 Santa Barbara Street, Pasadena, CA 91101, USA*
[9] *Kavli Institute for Cosmology, University of Cambridge, Madingley Road, Cambridge, CB3 0HA, UK*
[10] *Cavendish Laboratory, University of Cambridge, JJ Thomson Avenue, Cambridge, CB3 0US, UK*

ABSTRACT

We present the first ultra-deep rest-UV spectroscopy of four UV-bright Little Red Dots (LRDs), obtained from the SPURS Cycle 4 Large Program. The spectra reveal broad C IV (FWHM $\approx 2700-2800$ km s^{-1}) in two LRDs, alongside narrow-line densities elevated above star-forming galaxies ($n_e \sim 10^4-10^5$ cm^{-3}, reaching 10^6 cm^{-3} in the most extreme source) and nitrogen-enhancements in all four LRDs. We detect broad He II emission (FWHM ≈ 930 km s^{-1}) in one LRD, and two others with fast P-Cygni absorption ($\gtrsim 2200$ km s^{-1}). Strong interstellar absorption lines and Lyα damping wings reveal the UV continuum is deeply embedded in neutral gas ($N_{\rm HI} \gtrsim 10^{22}$ cm^{-2}) in all four LRDs. Detections of fluorescent Fe II and O I emission and fine-structure absorption indicate this gas lies close to the UV-emitting region. In archival $z > 4$ samples, we find nitrogen and strong C III] emission are significantly more common in LRDs than in the galaxy population. The transmission of broad C IV, tracing the broad-line region or cocoon, depends on rest-optical color within our sample, consistent with an orientation-dependent picture in which bluer, less obscured sightlines offer a more direct, polar view of the central engine and its outflows. We find several potential signatures of very massive stars, whose winds may contribute to nitrogen enhancement. We investigate other abundance patterns expected from supermassive stars but our results are inconclusive. Our results place the UV-emitting region within $\lesssim 8$ pc of the LRD nucleus, consistent with an actively assembling nuclear star cluster. Dynamical interactions in this extremely dense environment, including tidal disruption of stars, may explain the high incidence of nitrogen enhancements in LRDs.

Keywords: Active galactic nuclei (16) — High-redshift galaxies (734)

1. INTRODUCTION

JWST (J. P. Gardner et al. 2023; J. Rigby et al. 2023) has opened a new window onto the growth of supermassive black holes in the early universe. Deep spectroscopy has enabled the identification of broad-line (BL) active galactic nuclei (AGN) out to very high redshifts, revealing black hole growth already underway within the first billion years of cosmic history. Much of the early work in this area has focused on Little Red Dots (LRDs), a population of compact sources identified by the combination of red rest-frame optical colors and bluer rest-frame ultraviolet (UV) colors (L. J. Furtak et al. 2023; D. D. Kocevski et al. 2023; I. Labbé et al. 2023; J. E. Greene et al. 2024; J. Matthee et al. 2024). Following their discovery in JWST/Near Infrared Camera (NIRCam; M. J. Rieke et al. 2023) imaging (G. Barro et al. 2024; V. Kokorev et al. 2024; D. D. Kocevski et al. 2025;

Email: mengtao.tang@sjtu.edu.cn

I. Labbé et al. 2025), LRDs were shown to exhibit broad Balmer lines ($\gtrsim 1000$ km s^{-1}) alongside narrow forbidden lines ($\simeq 300$ km s^{-1}), a combination characteristic of broad-line AGN (J. E. Greene et al. 2024; M. Killi et al. 2024; R. Maiolino et al. 2024a; J. Matthee et al. 2024; R. E. Hviding et al. 2025).

Application of standard virial relations (J. E. Greene & L. C. Ho 2005; A. E. Reines & M. Volonteri 2015) to the broad Balmer lines suggested that LRDs host black holes with large masses ($\simeq 10^6 - 10^8$ $M_\odot$; e.g., J. E. Greene et al. 2024; X. Lin et al. 2024; R. Maiolino et al. 2024a; J. Matthee et al. 2024; D. D. Kocevski et al. 2025). Under the assumption that the rest-frame UV emission is dominated by the host galaxy, the inferred stellar masses were found to be relatively small ($\simeq 10^8 - 10^9$ $M_\odot$), implying black hole-to-stellar mass ratios in excess of local scaling relations (e.g., R. Maiolino et al. 2024a; D. D. Kocevski et al. 2025). These findings led to the conclusion that LRDs trace a population of galaxies with overmassive black holes. While it has been shown that LRDs only represent a subset of the high-z AGN JWST has discovered (K. N. Hainline et al. 2025; A. J. Taylor et al. 2025; D. D. Kocevski et al. 2026), their space density is large enough to suggest that they may represent an important channel of early black hole growth (e.g., G. Barro et al. 2024; V. Kokorev et al. 2024; H. B. Akins et al. 2025; I. Labbé et al. 2025).

As more data on LRDs arrived, evidence began to mount that they differed in several important ways from lower redshift broad-line AGN. Deep stacking experiments revealed that LRDs are X-ray weak (e.g., T. T. Ananna et al. 2024; M. Yue et al. 2024; H. B. Akins et al. 2025; R. Maiolino et al. 2025; M. Brazzini et al. 2026), suggesting either heavy gas obscuration or an intrinsically weak corona. Observations with MIRI and ALMA revealed little evidence of dust emission (e.g., P. G. Pérez-González et al. 2024; C. C. Williams et al. 2024; H. B. Akins et al. 2025), indicating the red colors are unlikely to be dominated by reddening. High ionization lines were found to be rare (e.g., M. Tang et al. 2025; E. Lambrides et al. 2026; B. Wang et al. 2026), perhaps indicating a softer ionizing spectrum. Deep rest-frame optical spectroscopy revealed Balmer line absorption and Balmer breaks, both suggesting very dense gas absorption by a population of hydrogen atoms in the $n = 2$ level (e.g. I. Juodžbalis et al. 2024; A. de Graaff et al. 2025a; K. Inayoshi & R. Maiolino 2025; X. Ji et al. 2025; R. P. Naidu et al. 2026).

These observations have motivated new theoretical frameworks for LRDs. Some have argued that LRDs are black holes embedded in a dense gas cocoon that thermalizes the accretion disk spectrum into a pseudo-blackbody (so-called "black hole stars"; A. de Graaff et al. 2025a; R. P. Naidu et al. 2026). More recently, radiative transfer models have shown that the red optical continuum of LRDs can be explained as Paschen free-bound nebular emission from the ionized cocoon (A. Sneppen et al. 2026a) without requiring full thermalization of the spectrum. In this and related frameworks, electron scattering broadens the Balmer lines as photons traverse the dense gas. The intrinsic line widths are therefore narrower than the observed profiles, implying correspondingly lower black hole masses. Recent work has demonstrated that these lower masses bring LRDs into closer agreement with the local black hole-to-stellar mass scaling relations (e.g., V. Rusakov et al. 2026; A. Torralba et al. 2026a). Whether these new frameworks provide the correct interpretation of the LRDs remains debated in the literature, with some groups arguing that LRDs can be more naturally explained as overmassive black holes in small galaxies (e.g., R. Maiolino et al. 2024a; M. Brazzini et al. 2025; I. Juodžbalis et al. 2026a; J. Scholtz et al. 2026a).

Progress on this debate has relied almost entirely on rest-frame optical and longer-wavelength observations. The rest-frame UV of LRDs remains comparatively unexplored, leaving key questions open. The UV continuum and narrow emission lines in LRDs are generally attributed to the host galaxy (e.g., A. de Graaff et al. 2025b; P. Rinaldi et al. 2025; K. Inayoshi et al. 2026; A. Torralba et al. 2026b), but it is possible that emission from the AGN or gas cocoon may contribute significantly to both (e.g., G. C. K. Leung et al. 2025; M. Ando et al. 2026). Studying the host galaxy via narrow emission lines in the optical is challenging owing to the underlying LRD continuum. The UV continuum offers a cleaner alternative, and it contains a suite of emission lines that are sensitive to the physical conditions of the ionized gas, the hardness of the ionizing spectrum, and the chemical abundance pattern. By benchmarking these UV narrow line diagnostics against the broader galaxy population, we can test whether LRD hosts are typical, or whether the narrow lines give indication of conditions rarely seen in galaxies. For example, several LRDs have been shown to have UV nitrogen lines that point to the same nitrogen-enhanced abundances seen in a subset of early galaxies (I. Labbé et al. 2024; R. Tripodi et al. 2025a; S. Mascia et al. 2026; T. Morishita et al. 2026; C. Papovich et al. 2026). Whether the nitrogen lines are common in LRDs is not known, nor is it clear what mechanism produces the peculiar abundances in LRDs.

The rest-frame UV also tests the broad-line region (BLR) and the dense gas cocoon directly, through both

Table 1. Basic properties of the four LRDs.

ID	RA (deg)	Dec (deg)	$z_{\rm spec}$	m_H	$M_{\rm UV}$
SPURS-GN-2	189.083481	+62.202583	7.1863	26.3	−20.7
SPURS-GN-2004	189.032464	+62.216423	6.7110	25.7	−21.1
SPURS-GN-29	189.019240	+62.243537	7.0374	26.6	−20.4
CEERS-7902	214.983030	+52.956010	6.9842	26.5	−20.4

Note—H-band magnitudes are computed from JWST/NIRCam F150W photometry.

emission and absorption. Existing, shallower spectra have not detected the broad permitted UV lines (C IV, He II, Mg II) expected from a standard broad-line region (M. Tang et al. 2025; E. Lambrides et al. 2026), but whether this reflects absorption by dense gas or an intrinsically softer ionizing spectrum remains unclear. A dense gas envelope around the UV continuum should leave its own signature: strong damped Lyα absorption and a forest of metal absorption lines. The kinematics and covering fraction recovered from these lines constrain both the structure of the cocoon and the origin of the UV continuum itself.

The SPectroscopic Ultra-deep Reionization-era Survey (SPURS; GO 9214, PIs: C. Mason, D. Stark) Cycle 4 Large Program is providing the first ultra-deep, moderate-resolution grating spectra covering the rest-frame UV of LRDs. In M. Tang et al. (2026b), we presented 29 hours G140M observations of two LRDs in Abell 2744, including the gravitationally lensed source Abell2744-QSO1 at $z = 7.04$ (discovered by L. J. Furtak et al. 2023). In this paper, we extend this work to four new LRDs (Table 1) observed with SPURS in the GOODS-North (GOODS-N; SPURS-GN-2, SPURS-GN-2004, SPURS-GN-29) and the Extended Groth Strip (EGS; CEERS-7902) fields. Using these observations, we characterize the density, temperature, and abundance pattern of the narrow-line gas; search for broad permitted UV lines (C IV, He II, Mg II) that trace the broad-line region; look for signatures of massive stars in the UV continuum; and measure the interstellar absorption lines that constrain the covering fraction, kinematics, and abundance pattern of the gas surrounding the UV-emitting source. An independent analysis of the abundances in these LRDs has been presented in Kokorev et al. (2026b).

The organization of this paper is as follows. In Section 2, we summarize what was previously known about the four LRDs, describe the new SPURS observations, present their basic physical properties with a focus on the rest-frame optical, and characterize the NIRCam images. We then characterize the rest-frame UV emission lines of the four LRDs in Section 3 and the interstellar absorption lines in Section 4. In Section 5, we discuss the narrow UV emission line properties of LRDs in the context of broader galaxy population. We discuss the implications for LRDs with SPURS spectra in Section 6. Finally, we summarize our conclusions in Section 7. Throughout the paper we adopt a Λ-dominated, flat universe with $\Omega_\Lambda = 0.7$, $\Omega_{\rm M} = 0.3$, and $H_0 = 70$ km s^{-1} Mpc^{-1}. All magnitudes are quoted in the AB system (J. B. Oke & J. E. Gunn 1983) and all equivalent widths (EWs) are quoted in the rest frame.

2. SPURS SPECTROSCOPY OF LRDS

Our sample consists of four LRDs, each selected to be bright in the rest-frame UV. Three of the LRDs are in GOODS-N (SPURS-GN-2, SPURS-GN-2004, SPURS-GN-29) and one is in EGS (CEERS-7902). We introduce the original observations of the LRDs in Section 2.1, describe the SPURS observations (Figure 1) and reduction in Section 2.2, then detail the basic properties of the LRDs in Section 2.3 focusing primarily on the rest-frame optical spectra, and characterize their NIRCam images in Section 2.4.

2.1. *Ancillary Data of LRD Sample*

SPURS-GN-2 (hereafter GN-2) has been imaged with JWST/NIRCam through the FRESCO (P. A. Oesch et al. 2023), CONGRESS (GO 3577, PIs: E. Egami, F. Sun), and JADES (D. J. Eisenstein et al. 2026) programs. It is bright in the rest-frame UV continuum ($H = 26.3$; Figure 2). Its redshift was first identified using the NIRCam F444W grism spectrum obtained from the FRESCO survey and reported in R. A. Meyer et al. (2024). The GO 4762 (PIs: S. Fujimoto, G. Brammer) program obtained a deep F410M grism spectrum (their ID 2756), which reveals broad Hβ emission and narrow [O III] emission lines (M. Xiao et al. 2025).

The other two LRDs in GOODS-N were also imaged by NIRCam as part of the JADES, CONGRESS, and

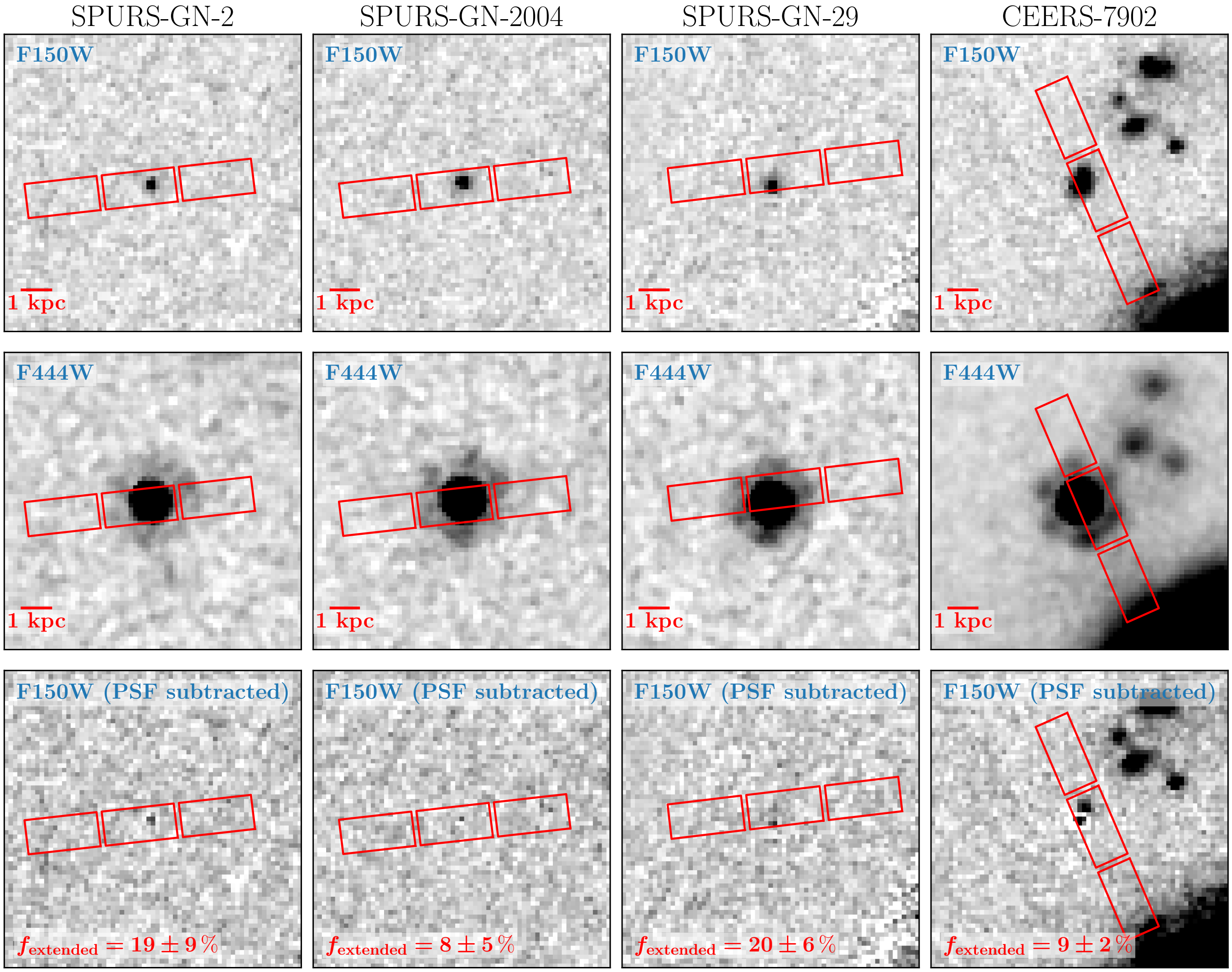

Figure 1. JWST/NIRCam F150W (top), F444W (middle), and PSF-subtracted F150W images (bottom) of GN-2, GN-2004, GN-29, and CEERS-7902. Each image is presented with a size of $2'' \times 2''$. For the top and middle rows, we show the scale bar of 1 kpc in the bottom left of each panel. For the bottom row, we note the light fraction from residual components after subtracting the point source in F150W. In each panel, we also overplot our NIRSpec shutters (red boxes) in SPURS observations.

FRESCO surveys. Among the four LRDs in this paper, SPURS-GN-2004 (hereafter GN-2004) is the brightest in the rest-frame UV continuum ($H = 25.7$; Figure 2). The SPURS observations provide the first spectroscopic confirmation of GN-2004. The redshift of SPURS-GN-29 (hereafter GN-29) was identified using the FRESCO F444W grism spectrum and reported in R. A. Meyer et al. (2024). The GO 4762 F410M grism spectrum (their ID 9094) reveals broad Hβ emission and narrow [O III] emission lines, as expected for broad-line AGN (M. Xiao et al. 2025). This LRD has the faintest rest-frame UV continuum magnitude in our sample ($H = 26.6$; Figure 2) but is still UV-bright when compared to the full population of LRDs.

CEERS-7902 was first classified as an LRD by its NIRCam photometry (I. Labbé et al. 2023; D. D. Kocevski et al. 2025), obtained via the CEERS Early Release Science program (S. L. Finkelstein et al. 2025). A low-resolution prism spectrum (0.8 hrs) and a medium-resolution G395M/F290LP spectrum (0.8 hrs) were obtained from the RUBIES program (A. de Graaff et al. 2025c), revealing the presence of a broad Hβ emission line with narrow rest-frame optical forbidden lines (B. Wang et al. 2024; D. D. Kocevski et al. 2025). The Cycle 2 GO 4287 program (PIs: C. Mason, D. Stark) observed the LRD again with NIRSpec medium resolution G395M/F290LP (1.0 hrs) and for the first time, the rest-frame UV was observed at high resolution ($R \sim 2700$) with the G140H/F100LP grating (3.9 hrs).

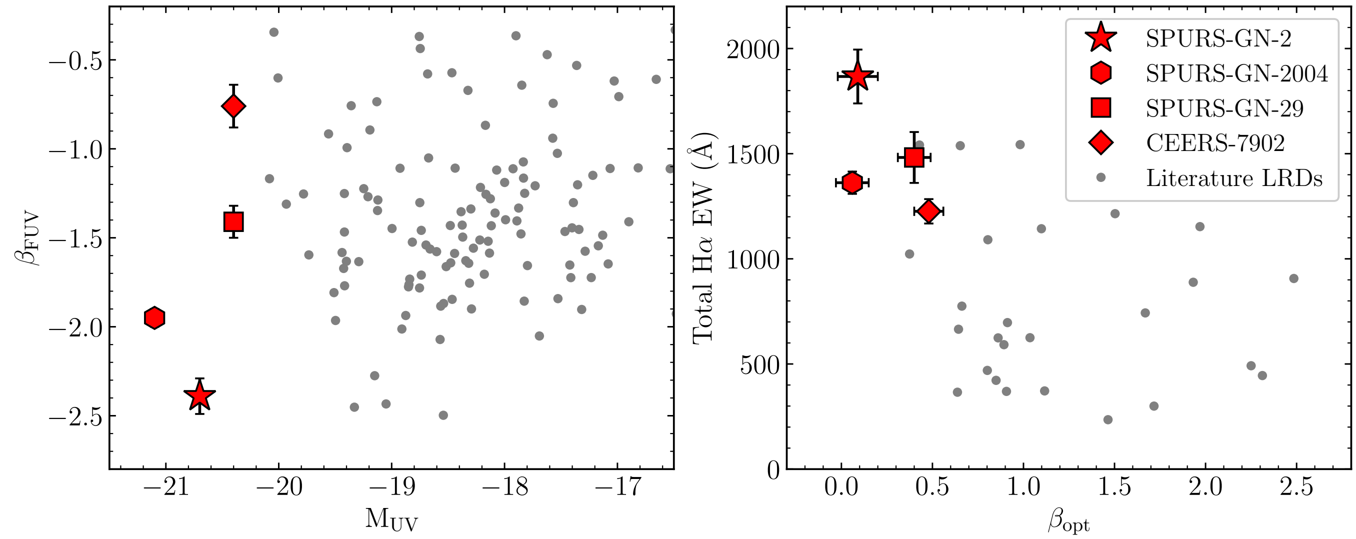

Figure 2. GN-2 (red star), GN-2004 (red hexagon), GN-29 (red square), and CEERS-7902 (red diamond) on the demographics of LRDs. Left panel: absolute UV magnitude versus rest-frame FUV continuum slope. Right panel: rest-frame optical continuum slope versus total Hα EW. In each panel, we overplot LRDs in literature (A. de Graaff et al. 2025b; R. E. Hviding et al. 2025; D. D. Kocevski et al. 2025) as grey circles for comparison.

2.2. *SPURS Observations and Reduction*

The SPURS NIRSpec (P. Jakobsen et al. 2022; T. Böker et al. 2023) observations were conducted using the medium-resolution ($R \simeq 1000$, corresponding to $\simeq 300$ km s^{-1} per resolution element) grating/filter pairs G140M/F100LP, G235M/F170LP, and G395M/F290LP. We used the three-shutter nod pattern for dithering, which is appropriate for compact high redshift targets. The total on-target integration time is 29 hours, 7.9 hours, and 2.9 hours for G140M, G235M, and G395M, respectively.

We reduced the 2D NIRSpec spectra using the latest version of `msaexp`[11] package (G. Brammer 2023) which is based on the standard JWST data reduction pipeline[12] (H. Bushouse et al. 2024), following the procedures and setup described in A. de Graaff et al. (2025c) and K. E. Heintz et al. (2025). We assumed a point source pathloss correction, motivated by the compact morphology of the four LRDs (Figure 1). The 1D spectra were extracted from the reduced 2D spectra using an optimal extraction (K. Horne 1986). Throughout this reduction, we utilize the extended wavelength extraction available as part of `msaexp` (F. Valentino et al. 2025) to achieve wavelength coverage beyond the nominal limits of each grating. This is made by picking up the full wavelength range covered by the detector, which may be contaminated by second-order spectra. However, we only focus on extended G395M spectra (up to 5.5 μm) to cover Hα line at $z \simeq 7$, which is not affected by higher-order contamination as contamination begins at wavelengths longer than 5.6 μm. Finally, we recalibrate the absolute flux of the reduced spectrum to match that of NIRCam by applying a second-order polynomial correction factor as a function of wavelength (Z. Chen et al. 2026a). We derive this correction by fitting the ratio of the NIRCam photometry, where we adopt the CIRC1 photometry available from the JADES DR5 (B. E. Robertson et al. 2026, for GN-2, GN-2004, and GN-29) and the CEERS photometric catalogs (R. Endsley et al. 2025, for CEERS-7902), to that synthesized from the coadded spectrum in broad NIRCam filters (from F115W to F444W).

The G140M observations cover rest-frame wavelengths of 1220 − 2600 Å for GN2, 1250 − 3080 Å for GN-2004 (with a chip gap between 1460 and 1600 Å), 1200 − 2110 Å for GN-29, 1210 − 2750 Å for CEERS-7902. We characterize the remainder of the near-UV (2400 − 3500 Å) by stacking G140M and G235M. For the G140M spectra, the median 3σ limiting flux for an unresolved emission line (in spectral direction) of a point source is 1.4×10^{-19} erg s^{-1} cm^{-2}. Continua of all four LRDs are clearly detected in G140M spectra, with signal-to-noise ratio (S/N) of 5.9 (GN-2), 10.3 (GN-2004), 5.7 (GN-29), and 3.5 (CEERS-7902) per resolution element at rest-frame 1700 Å. These allow us to detect weak emission lines in the rest-frame UV with EWs of 1.3 Å, 0.7 Å, 1.2 Å, and 1.9 Å for GN-2, GN-2004, GN-29, and CEERS-7902, respectively.

[11] https://github.com/gbrammer/msaexp
[12] https://github.com/spacetelescope/jwst

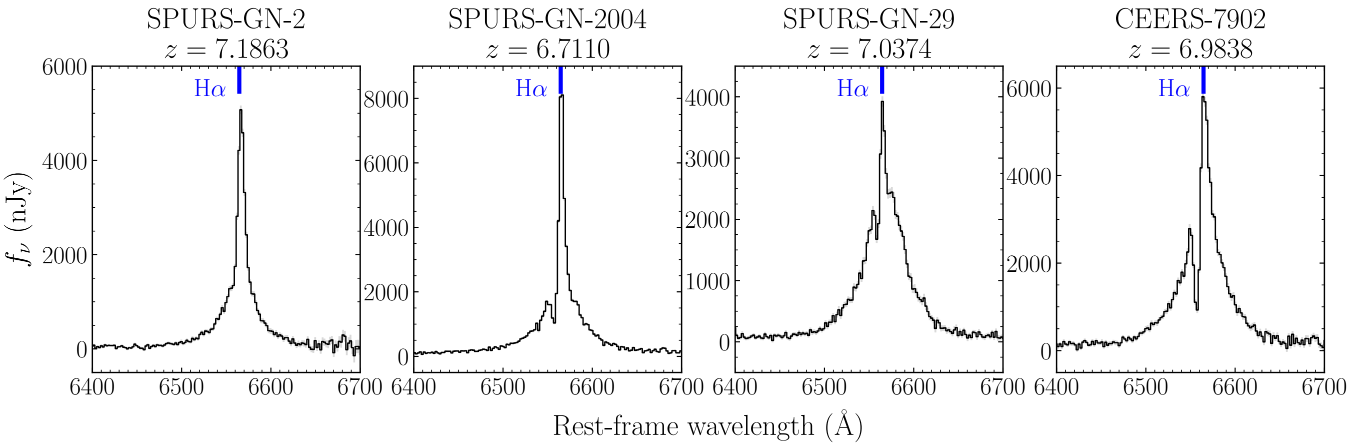

Figure 3. Hα emission lines in SPURS G395M spectra of the four LRDs. For each spectrum, the observed flux density and 1σ uncertainty are shown as black solid line and grey shaded region, respectively.

The median 3σ limiting flux of the G235M spectra is 1.7×10^{-19} erg s^{-1} cm^{-2}. We also detect near-UV continua with S/N of 3.7 (GN-2), 5.7 (GN-2004), 4.3 (GN-29), and 3.1 (CEERS-7902) at rest-frame 2700 Å. These correspond to limiting EWs of 3.4 Å (GN-2), 2.0 Å (GN-2004), 2.9 Å (GN-29), and 4.1 Å (CEERS-7902). For the G395M spectra, the median 3σ limiting flux reaches 2.4×10^{-19} erg s^{-1} cm^{-2}.

For each source, we measure the emission lines as follows. For an emission line detected with S/N > 5, we measure the line flux, centroid, width, and EW by fitting the line profile and nearby continuum with a Gaussian function. For lines that are close in wavelength or a line that shows multiple components, we fit the line profile with multiple Gaussians simultaneously. If a line is detected with lower S/N (< 5), we compute the line fluxes by directly integrating the continuum-subtracted line profile. Finally, the uncertainties of line fluxes and EWs are evaluated as follows. We resample the flux densities of each spectrum 1000 times by taking the observed value as the mean and the error as the standard deviation. Then we compute the line fluxes and EWs from the resampled spectra of each source using the same approach described above. We take the standard deviation of these measurements as the uncertainty.

We derive the systemic redshifts ($z_{\rm sys}$) using strong forbidden oxygen emission lines in the rest-frame optical ([O III] $\lambda\lambda 4959, 5007$). For each LRD, we simultaneously fit the [O III] doublet with Gaussian functions. We use the fitted line centers to compute redshifts, then average them weighted by the emission line signal-to-noise ratio to obtain the final systemic redshift. We obtain systemic redshifts of $z_{\rm sys} = 7.1863$ for GN-2, $z_{\rm sys} = 6.7110$ for GN-2004, $z_{\rm sys} = 7.0374$ for GN-29, and $z_{\rm sys} = 6.9838$ for CEERS-7902.

2.3. *Properties of SPURS LRDs*

Before presenting the rest-frame UV spectra of the four LRDs, we situate the sample within the broader landscape of LRD properties established in recent compilations (A. de Graaff et al. 2025b; R. E. Hviding et al. 2025; D. D. Kocevski et al. 2025). Since the rest-frame UV spectra are presented in later sections, we focus here on the rest-frame optical spectra. Although several of the LRDs have prior observations from other programs (Section 2.1), we adopt the SPURS grating spectra throughout for consistency with our rest-frame UV measurements. We present the rest-frame optical spectroscopic properties of the four LRDs in Table 2. Full details of the rest-frame optical spectra are presented in Appendix D.2.

We identify broad components of the Balmer lines in all four LRDs (Figure 3). We adopt two fitting techniques to recover the Balmer line profiles, one using a combination of a narrow (full width at half maximum FWHM $\lesssim 500$ km s^{-1}) and two broad Gaussian functions, and the other using an exponential function to capture the broad profile. When the Balmer line shows an absorption component, we fit the absorption line with an additional Gaussian. The methodology and fits are described in Appendix B, where we demonstrate that both methods are able to recover the Balmer profiles equally well. The results derived from triple Gaussian fits are presented in Table 2. With these models, the broad component of Hα of each LRD is described by the sum of a component with FWHM ranging from 3523 to 4336 km s^{-1} and an intermediate component (FWHM ranging from 1275 to 1679 km s^{-1}). For each LRD, the broad FWHMs of the two components span the range of those derived from single Gaussian fits to broad Balmer lines (e.g., J. E. Greene et al. 2024; J.

Table 2. Continuum and optical spectroscopic properties of the four LRDs.

Properties	SPURS-GN-2	SPURS-GN-2004	SPURS-GN-29	CEERS-7902
$\beta_{\rm FUV}$	-2.39 ± 0.10	-1.95 ± 0.05	-1.41 ± 0.09	-0.76 ± 0.12
$\beta_{\rm NUV}$	-2.34 ± 0.18	-2.10 ± 0.16	-1.34 ± 0.17	-1.05 ± 0.32
$\beta_{\rm opt}$	0.09 ± 0.11	0.06 ± 0.09	0.40 ± 0.09	0.48 ± 0.08
$f_{\nu,4050}/f_{\nu,3670}$	1.39 ± 0.39	1.75 ± 0.33	1.90 ± 0.34	2.16 ± 0.47
FWHM$_{\rm H\alpha,narrow}$ (km s^{-1})	353 ± 9	277 ± 7	276 ± 8	329 ± 7
EW$_{\rm H\alpha,narrow}$ (Å)	504 ± 18	331 ± 11	156 ± 33	104 ± 7
FWHM$^{\rm a}_{\rm H\alpha,broad}$ (km s^{-1})	1395 ± 101	1505 ± 55	1639 ± 90	1275 ± 61
	3523 ± 228	4336 ± 140	3664 ± 154	3679 ± 97
EW$^{\rm b}_{\rm H\alpha,broad}$ (Å)	1363 ± 127	1120 ± 52	1466 ± 116	1266 ± 58
FWHM$_{\rm H\alpha,abs}$ (km s^{-1})	–	356 ± 41	258 ± 85	337 ± 20
EW$_{\rm H\alpha,abs}$ (Å)	–	-89 ± 11	-113 ± 30	-144 ± 11
$\Delta v_{\rm H\alpha,abs}$ (km s^{-1})	–	-293 ± 50	-140 ± 48	-317 ± 48
$F_{\rm H\alpha,narrow}/F_{\rm H\beta,narrow}$	11 ± 1	5.9 ± 0.5	5.2 ± 1.3	7.2 ± 1.0
$F_{\rm H\alpha,broad}/F_{\rm H\beta,broad}$	12 ± 2	10 ± 1	14 ± 2	11 ± 1
O3	3.0 ± 0.3	7.6 ± 0.5	11.3 ± 1.6	9.0 ± 1.1
O32	29 ± 6	36 ± 3	17 ± 2	16 ± 3
Ne3O2	4.9 ± 1.1	2.0 ± 0.2	1.0 ± 0.1	1.7 ± 0.4

Note—Hα properties are derived from Gaussian fits to the line profile, where the narrow Hα emission is fitted by a Gaussian and the broad Hα emission is described by the sum of two Gaussian functions for each LRD. More details of Gaussian fits and exponential fits are presented in Appendix B.

a: FWHMs of two broad Gaussian functions of each LRD. When adopting exponential fits, the broad FWHMs are 1180 ± 95 km s^{-1} (GN-2), 1690 ± 74 km s^{-1} (GN-2004), 1233 ± 70 km s^{-1} (GN-29), and 1485 ± 59 km s^{-1} (CEERS-7902).

b: EW of the sum of the two broad Hα components of each LRD.

Matthee et al. 2024; R. E. Hviding et al. 2025; D. D. Kocevski et al. 2025). When fitting the broad Hα lines with an exponential function, we find narrower FWHMs ($1180-1690$ km s^{-1}, Table B.1), as is expected for electron scattering broadening scenarios (A. Sneppen et al. 2026b). We also find absorption features in the Hα lines of GN-2004, GN-29, and CEERS-7902, with no Balmer line absorption in GN-2 (Figure 3). The Hα absorption lines of the three LRDs are narrow (FWHM $= 258 - 356$ km s^{-1}) and blueshifted ($\Delta v = -317$ to -140 km s^{-1}) with respect to the line center.

We characterize the continuum of the four LRDs using our spectra, measuring the rest-frame optical and UV slopes. For the rest-frame optical continuum slope ($\beta_{\rm opt}$), we fit the spectra at rest-frame wavelengths of $3700 - 6300$ Å after masking out the regions containing emission lines following A. de Graaff et al. (2025b); R. E. Hviding et al. (2025). By definition, the four LRDs are all red in their rest-frame optical colors, but the continuum slopes span a wide range. GN-2 ($\beta_{\rm opt} = 0.09 \pm 0.11$) and GN-2004 ($\beta_{\rm opt} = 0.06 \pm 0.09$) are on the bluer side of the LRD color distribution (right panel of Figure 2), both approaching the colors often seen in the LBD population (M. Brazzini et al. 2026). GN-29 ($\beta_{\rm opt} = 0.40 \pm 0.09$) and CEERS-7902 ($\beta_{\rm opt} = 0.48 \pm 0.08$) are somewhat redder, yet we note LRD optical colors extend as red as $\beta_{\rm opt} = 2.5$ (Figure 2).

We measure UV continuum slope in the far-UV (FUV) and in the near-UV (NUV), as different physical processes may dominate in the different wavelength regimes. For example, damped Lyα absorption will contribute primarily to the FUV slopes, whereas the Balmer free-bound nebular continuum emission will contribute primarily to the NUV slopes. The far-UV slope is measured between 1400 Å and 2400 Å, and the near-UV slope is measured between 2400 Å and 3500 Å. We again mask out the regions containing emission lines or absorption lines when deriving the UV continuum slopes. The four LRDs also span a wide range of UV slopes. GN-2 ($\beta_{\rm FUV} = -2.39 \pm 0.10$) and GN-2004 ($\beta_{\rm FUV} = -1.95 \pm 0.05$) have very blue FUV slopes in the context of the full the LRD population (left panel of Figure 2). GN-29 ($\beta_{\rm FUV} = -1.41 \pm 0.09$) and CEERS-7902 ($\beta_{\rm FUV} = -0.76 \pm 0.12$) have much redder FUV continuum slopes. We find that the NUV continuum slope of each LRD is similar to its FUV slope. We derive blue NUV slopes in GN-2 ($\beta_{\rm NUV} = -2.34 \pm 0.18$) and GN-2004 ($\beta_{\rm NUV} = -2.10 \pm 0.16$), and red NUV slopes in GN-29 ($\beta_{\rm NUV} = -1.34 \pm 0.17$) and CEERS-7902 ($\beta_{\rm NUV} = -1.05 \pm 0.32$).

We quantify the amplitude of the Balmer break as $f_{\nu,4050}/f_{\nu,3670}$, following recent literature studies (e.g., A. de Graaff et al. 2025c). GN-2 (1.4 ± 0.4), GN-2004 (1.8 ± 0.3), and GN-29 (1.9 ± 0.3) show moderately strong breaks, comparable to the median for the full LRD population (1.5; A. de Graaff et al. 2025b). CEERS-7902 (2.2 ± 0.5) shows the strongest break in our sample, though we note that LRD Balmer breaks can reach as large as $\simeq 8$ (e.g., A. de Graaff et al. 2025a; R. P. Naidu et al. 2026).

We identify narrow components (FWHM $\simeq$ 300 km s^{-1}) in the Balmer lines, and we find that the four LRDs in our sample exhibit different Hα narrow-to-broad luminosity ratios. GN-2 and GN-2004 have comparatively strong narrow components relative to broad (broad-to-narrow ratios of 2.7 and 3.4), while GN-29 and CEERS-7902 are broad-dominated, with ratios of 9.4 and 12. If the narrow-to-broad flux ratio reflects the relative contribution of star-forming host versus AGN (or dense gas cocoon emission), GN-2 and GN-2004 should show correspondingly different UV line and continuum properties than GN-29 and CEERS-7902.

In all four LRDs, the narrow Hα/Hβ flux ratios ($5.2 - 11$) depart significantly from expectations from case B recombination (2.76 for $T = 2 \times 10^4$ K; D. E. Osterbrock & G. J. Ferland 2006). The narrow line spectra additionally constrain the ratio of [O III]/[O II] (O32) and [Ne III]/[O II] (Ne3O2), both of which are sensitive to the ionization parameter and electron density in the narrow line-emitting gas. For the four LRDs, we measure elevated O32 ratios ($16 - 36$) and similarly large Ne3O2 ratios ($1.0 - 4.9$), comparable to the typical O32 ($\simeq 25$) and Ne3O2 ($\simeq 1$) ratios found in LRDs (e.g., G. P. Nikopoulos et al. 2026). We find that the two bluer LRDs, GN-2 and GN-2004, also have the largest O32 ($29 - 36$) and Ne3O2 ($2.0 - 4.9$) ratios in the sample, roughly a factor of ~ 2 and up to ~ 5 higher, respectively, than GN-29 and CEERS-7902 (O32 $= 16 - 17$; Ne3O2 $= 1.0 - 1.7$).

The gas-phase metallicity of the narrow line gas can be constrained from the narrow line flux ratios. The four LRDs have narrow [O III] λ5007/Hβ (O3) flux ratios between 3.0 and 11, as expected for low to moderate metallicity ionized gas. For reference, these are much larger than the O3 ratio of the very low metallicity LRD Abell2744-QSO1 ($\simeq 1$; F. D'Eugenio et al. 2026; M. Tang et al. 2026b) but consistent with the O3 values spanned by the full population of LRDs, where the $16 - 50 - 84$ percentile is $4.9 - 7.5 - 8.6$ (G. P. Nikopoulos et al. 2026). In the SPURS rest-frame optical spectra of all the four LRDs, we detect the auroral [O III] λ4363 emission line (Figure D.1) allowing a calculation of the electron temperature and metallicity via the direct method. We characterize the temperatures and gas-phase oxygen abundances of the four LRDs following the methodology commonly used in the literature (e.g., Y. Isobe et al. 2025; G. P. Nikopoulos et al. 2026). We use the `Python` package `PyNeb` (V. Luridiana et al. 2015) and our methods are described in Appendix C. We derive high electron temperatures ($1.8 - 4.0 \times 10^4$ K) from the [O III]λ4363/[O III]λ5007 ratios (Table 5). The direct method indicates the narrow line gas is moderately metal poor in all four LRDs ($12 + \log{\rm (O/H)} = 7.21 - 8.13$), corresponding to $Z = 0.03 - 0.28\ Z_\odot$, assuming solar oxygen abundance $12 + \log {\rm O/H} = 8.69$ in M. Asplund et al. 2021). The inferred metallicities of our sample appear consistent with those derived for the narrow line gas in the majority of LRDs (e.g., Y. Isobe et al. 2025; G. P. Nikopoulos et al. 2026).

The rest-frame optical spectrum also reveals a broad component in the [O III] $\lambda\lambda$4959, 5007 profile in each of the LRDs, suggesting the presence of ionized outflow. Following our methods in Appendix A, we fit simultaneously to the [O III] doublet, considering both the single Gaussian fit and the double Gaussian fit with a narrow as well as a broad component. We evaluate the goodness of fit using the Bayesian Information Criterion (BIC; G. Schwarz 1978; A. R. Liddle 2007). We find the double Gaussian fit yields significantly better results than the single Gaussian fit in all four sources, with BIC differences of ΔBIC = BIC(double) − BIC(single) = -39 to -621. We present these double Gaussian fits in Figure D.2. We measure the largest width for the broad component in GN-2 (FWHM $= 1627 \pm 181\,{\rm km\,s^{-1}}$), which contributes $25 \pm 2\%$ of the total [O III] line flux. The other three sources have slightly smaller broad component FWHM ($1130 - 1285\,{\rm km\,s^{-1}}$), which still contribute $13 - 21\%$ of the total line flux.

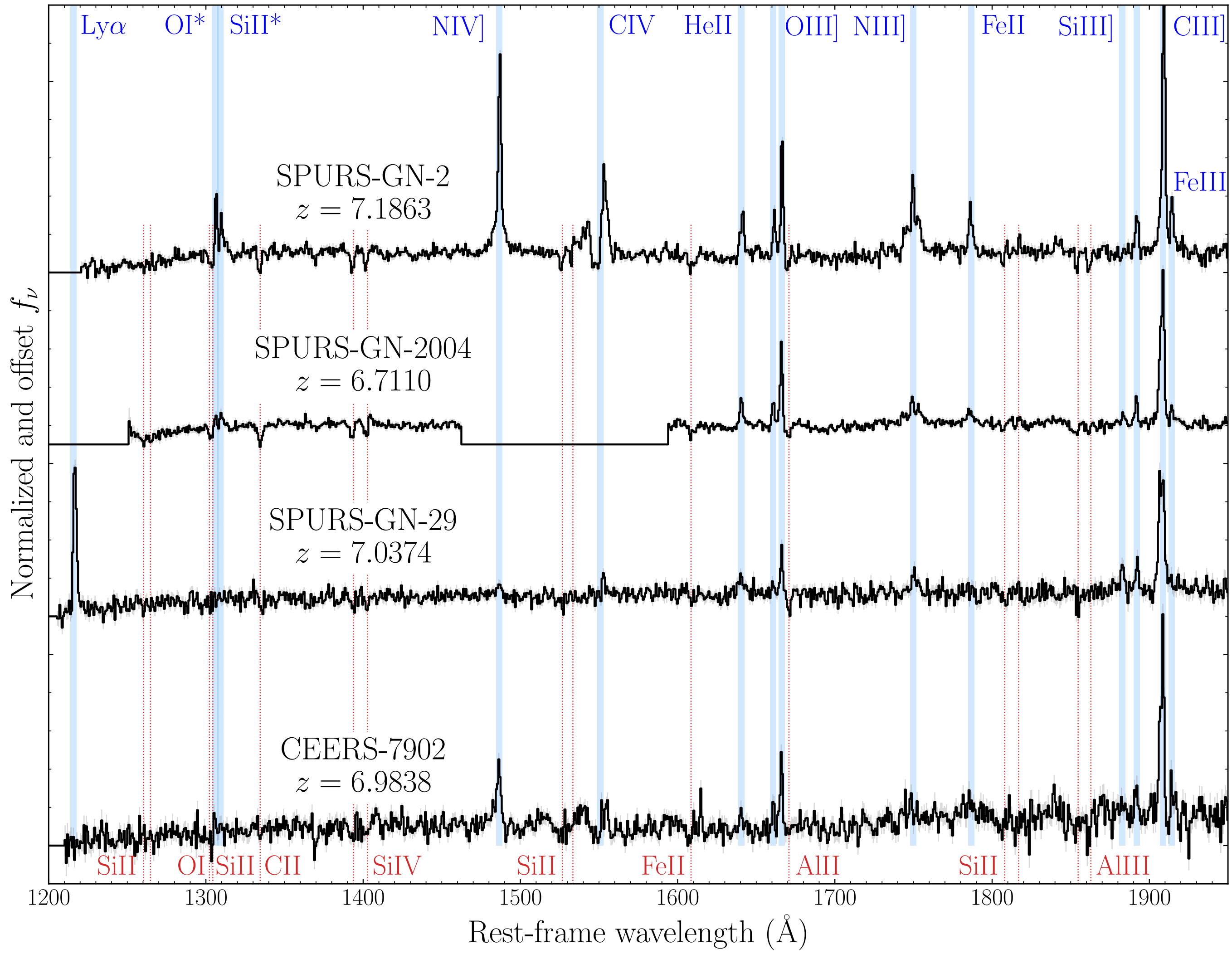

Figure 4. SPURS G140M (rest-frame far-UV) spectra of GN-2, GN-2004, GN-29, and CEERS-7902. Observed fluxes are shown as black solid lines and 1σ uncertainties are shown as grey shaded regions. We highlight UV emission lines and interstellar absorption lines as blue shaded regions and red dotted lines, respectively.

2.4. *NIRCam PSF Decomposition*

While the rest-frame UV NIRCam images of all four LRDs appear to be dominated by a single compact object, we quantify whether there may be a contribution from an additional extended component that could correspond to the host galaxy. To do so, we use the NIRCam F150W images of GOODS-N and EGS reduced following the procedures described in R. Endsley et al. (2025), together with the empirical point spread functions (PSFs) constructed from isolated stars in the same mosaics (R. Endsley et al. 2025). To decompose the point source from any possible extended component, we fit the light profile of each source with `pysersic` (I. Pasha & T. B. Miller 2023), assuming both a point-source and a Sérsic component whose positions, fluxes, and structural parameters are allowed to vary. For SPURS-GN-2004, where the light profile is well fit with a single point-source component, we instead use the fit assuming a point source only. We then subtract the fitted point-source component from the NIRCam images to obtain the PSF-subtracted images shown in the bottom panels of Figure 1.

We find no evidence for extended components in GN-2 and GN-2004 ($< 3\sigma$) and conclude the vast majority of their UV emission is unresolved. We detect extended components in GN-29 and CEERS-7902 and compute SNRs of 3.2 and 4.9 based on the residual flux measured with $r = 0.15''$ apertures centered at the point source positions (masking the central 3×3 pixels to exclude the PSF core), respectively. However, these additional components comprise only $20 \pm 6\%$ (GN-29) and $9 \pm 2\%$ (CEERS-7902) of the total F150W flux, respectively.

Table 3. Rest-frame UV emission line fluxes (10^{-19} erg s^{-1} cm^{-2}), EWs (Å), and FWHMs (km s^{-1}) of the four LRDs.

	SPURS-GN-2			SPURS-GN-2004			SPURS-GN-29			CEERS-7902		
Line	Flux	EW	FWHM	Flux	EW	FWHM	Flux	EW	FWHM	Flux	EW	FWHM
Lyα	–	–	–	–	–	–	31.1 ± 2.1	26.4 ± 1.8	495 ± 28	< 2.9	< 2.3	–
N V λ1239	< 1.4	< 2.8	–	–	–	–	< 2.1	< 1.8	–	< 2.5	< 2.0	–
N V λ1243	< 1.5	< 2.8	–	–	–	–	< 2.0	< 1.7	–	< 2.4	< 2.0	–
O I* λ1306	8.9 ± 0.5	6.8 ± 0.4	353 ± 30	3.4 ± 0.9	1.3 ± 0.4	360 ± 113	< 1.7	< 1.5	–	< 2.2	< 1.8	–
Si II* λ1309	6.7 ± 0.6	5.1 ± 0.4	416 ± 78	5.5 ± 0.9	2.0 ± 0.3	475 ± 107	< 1.5	< 1.3	–	< 2.6	< 2.2	–
N IV]$_{total}$	33.3 ± 0.8	26.5 ± 0.6	–	–	–	–	2.1 ± 0.7	1.9 ± 0.7	–	13.2 ± 1.0	11.5 ± 0.9	–
[N IV] $\lambda1483_{narrow}$	< 1.0	< 0.8	–	–	–	–	< 2.1	< 1.9	–	3.4 ± 1.0	2.9 ± 0.8	464 ± 56
[N IV] $\lambda1483_{broad}$	< 4.6	< 3.7	–	–	–	–	–	–	–	–	–	–
N IV] $\lambda1486_{narrow}$	18.2 ± 0.9	14.5 ± 0.7	357 ± 13	–	–	–	2.1 ± 1.1	1.9 ± 1.0	524 ± 228	9.8 ± 1.4	8.6 ± 1.2	464 ± 56
N IV] $\lambda1486_{broad}$	15.1 ± 2.4	12.0 ± 1.9	1514 ± 137	–	–	–	–	–	–	–	–	–
C IV λ1548[a]	26.1 ± 2.5	25.6 ± 2.5	–	–	–	–	2.2 ± 0.7	2.1 ± 0.6	318 ± 70	7.9 ± 3.8	8.0 ± 3.9	–
He II λ1640	4.5 ± 1.2	5.6 ± 1.5	468 ± 91	6.2 ± 1.5	3.5 ± 0.8	424 ± 67	4.1 ± 1.2	4.1 ± 1.2	929 ± 211	1.6 ± 0.9	2.0 ± 1.2	291 ± 127
O I] λ1641	1.8 ± 0.7	2.2 ± 0.9	340 ± 16	< 3.0	< 1.6	–	< 1.6	< 1.7	–	< 2.4	< 2.9	–
O III] λ1661	4.2 ± 0.5	5.3 ± 0.6	340 ± 16	5.2 ± 0.7	3.0 ± 0.4	334 ± 17	1.1 ± 0.4	1.1 ± 0.4	319 ± 39	2.1 ± 0.6	2.7 ± 0.7	286 ± 33
O III] λ1666	11.3 ± 0.7	14.6 ± 0.9	340 ± 16	15.6 ± 1.1	9.0 ± 0.7	334 ± 17	3.9 ± 0.6	4.0 ± 0.7	319 ± 39	5.9 ± 0.9	7.4 ± 1.2	286 ± 33
N III]$_{total}$	18.7 ± 0.7	21.8 ± 0.8	–	15.2 ± 0.9	7.9 ± 0.5	–	4.5 ± 0.8	5.0 ± 0.8	–	3.9 ± 1.0	4.1 ± 1.0	–
N III] $\lambda1746 - 1754$[b]	5.4 ± 0.2	6.3 ± 0.2	–	6.9 ± 0.4	3.6 ± 0.2	–	4.5 ± 0.8	5.0 ± 0.8	–	3.9 ± 1.0	4.1 ± 1.0	–
N III]$_{broad}$	13.3 ± 3.0	15.5 ± 3.5	1797 ± 219	8.3 ± 4.0	4.3 ± 2.1	2271 ± 649	–	–	–	–	–	–
Fe II λ1786	5.4 ± 0.5	6.0 ± 0.5	381 ± 60	5.6 ± 0.8	3.1 ± 0.4	789 ± 154	< 1.6	< 1.8	–	5.4 ± 0.9	5.5 ± 1.0	2189 ± 621
Si III] λ1883	< 0.9	< 1.2	–	1.8 ± 0.6	1.1 ± 0.3	302 ± 47	2.6 ± 0.6	3.1 ± 0.7	396 ± 59	< 2.7	< 2.6	–
Si III] λ1892	3.4 ± 0.7	4.7 ± 1.0	373 ± 57	4.1 ± 0.9	2.6 ± 0.6	302 ± 47	2.8 ± 0.6	3.3 ± 0.7	396 ± 59	2.5 ± 1.2	2.5 ± 1.2	410 ± 140
C III]$_{total}$	29.5 ± 0.7	42.5 ± 1.0	–	34.3 ± 0.8	22.5 ± 0.5	–	17.7 ± 0.7	21.5 ± 0.9	–	17.8 ± 0.7	17.8 ± 0.7	–
[C III] $\lambda1907_{narrow}$	< 1.4	< 2.0	–	11.6 ± 0.8	7.6 ± 0.5	312 ± 12	8.5 ± 1.1	10.3 ± 1.3	394 ± 39	6.5 ± 0.7	6.5 ± 0.7	243 ± 13
[C III] $\lambda1907_{broad}$	< 2.7	< 3.9	–	–	–	–	–	–	–	–	–	–
C III] $\lambda1909_{narrow}$	17.8 ± 0.4	25.7 ± 0.6	305 ± 10	22.7 ± 1.2	14.9 ± 0.8	312 ± 12	9.2 ± 1.1	11.2 ± 1.3	394 ± 39	11.3 ± 0.9	11.3 ± 0.9	243 ± 13
C III] $\lambda1909_{broad}$	9.8 ± 2.6	14.1 ± 3.7	2271 ± 371	–	–	–	–	–	–	–	–	–
[Ne IV] λ2422	< 1.2	< 1.9	–	< 1.5	< 1.4	–	< 1.6	< 2.5	–	< 2.5	< 3.7	–
[Ne IV] λ2424	< 1.2	< 1.8	–	< 1.6	< 1.5	–	< 1.4	< 2.3	–	< 2.3	< 3.4	–
Mg II λ2796	2.1 ± 0.4	4.3 ± 0.9	262 ± 65	< 1.6	< 1.6	–	< 1.6	< 2.9	–	< 2.3	< 3.2	–
Mg II λ2803	< 1.3	< 2.7	–	< 1.6	< 1.6	–	< 1.7	< 3.0	–	< 2.7	< 3.7	–
[Ne V] λ3427	< 1.2	< 4.6	–	< 1.4	< 2.5	–	< 1.6	< 4.2	–	< 2.8	< 5.8	–

NOTE—For non-detections, 3σ upper limits of line fluxes and EWs are provided.

a: Integrated line flux and EW of C IV doublet.

b: Integrated line flux and EW of narrow components of N III] quintuplet.

To constrain the size of the unresolved component itself, we repeat the PYSERSIC decomposition with the point source replaced by a PSF-convolved exponential profile ($n = 1$ Sérsic), while retaining the second Sérsic component, if present, so that the extended light (e.g. the neighboring component of CEERS-7902) does not bias the size of the compact component. The recovered effective radii of the compact component are < 80 pc (0.5 pixel) in all four sources, which is below the nominal PSF F150W FWHM of $\simeq 1.6$ pixel listed in JDox, as expected for PSF-convolved fits at high S/N. We therefore conclude that the rest-frame UV emission in the NIRCam images, and thus in our observed spectra, primarily arises from the central point source ($r_e \lesssim 80$ pc) in these LRDs.

3. REST-FRAME UV EMISSION LINES

The SPURS observations provide robust constraints on faint rest-frame UV emission lines across all four LRDs. In this section, we describe the UV emission line properties and their implications for the physical conditions of the LRDs. Figure 4 shows the far-UV spectra of the sample, and we show the UV emission line measurements in Table 3. We will present more detailed views of individual features as they arise in the discussion below.

3.1. *C IV Emission and Absorption*

The C IV $\lambda\lambda1548, 1550$ resonant profile presents a mixture of emission and absorption requiring moderate resolution spectroscopy to disentangle. Three of the four SPURS LRDs (GN-2, GN-29, CEERS-7902) have C IV spectral coverage. We present the C IV profiles of GN-2 and CEERS-7902 in Figure 5 and discuss each of the three LRDs with C IV observations below.

GN-2 provides our most detailed view of the C IV $\lambda\lambda1548, 1550$ profile. The most prominent feature is a narrow emission line (FWHM $= 540 \pm 57$ km s^{-1}) centered at a velocity of $+568 \pm 71$ km s^{-1} relative to the C IV $\lambda1550$ centroid. Such redshifted emission is common in C IV profiles owing to resonant scattering through an outflowing medium (e.g., D. A. Berg et al. 2019; P. Senchyna et al. 2022). There is also an absorption trough spanning 1400 km s^{-1}, between rest-frame wavelengths of $\sim$ 1544 Å and 1550 Å. The absorption lines are blueshifted, with a velocity offset of -353 ± 39 km s^{-1} with respect to the line center of each component of the doublet. This is consistent with there being significant resonant scattering of C IV photons from an outflowing highly ionized medium. At shorter wavelengths (1529 – 1543 Å), we see a blue wing of emission, corresponding to a broad component with a FWHM of 2830$\pm$191 km s^{-1}. Overall, the C IV profile in GN-2 is well fit by a combination of Gaussian functions reproducing the absorption profile and the two emission profiles (left panel of Figure 5). The best-fit parameters are presented in Table 4. The fit suggests that the broad component is slightly blueshifted (-293 ± 71 km s^{-1}) with respect to line center of C IV $\lambda1548$.

We compare the broad C IV profile of GN-2 to the broad Balmer emission line profile. The broad C IV line width appears qualitatively similar to that of Hα (Figure 6). The FWHM of broad C IV (2830 km s^{-1}) is comparable to broad Hα, which is fit as the combination of two broad Gaussians with FWHM of 1395 and 3523 km s^{-1} (Section 2.3). Using the fit described above, we find that the total broad C IV/Hβ flux ratio is 0.71 ± 0.09. However, the C IV absorption trough removes a significant component of the broad C IV line. As a result, the observed broad C IV/Hβ flux ratio is 0.36 ± 0.07. Both derived flux ratios are considerably lower than those of typical BL AGNs ($\sim$ 3; e.g., P. J. Francis et al. 1991; M. S. Brotherton et al. 2001; D. E. Vanden Berk et al. 2001). So while we find evidence of a broad C IV profile in GN-2, it appears to be significantly attenuated relative to the general population of BL AGNs.

The C IV profile of CEERS-7902 (right panel of Figure 5) resembles that of GN-2. It has a broad blue emission wing, an absorption trough, and narrow redshifted emission. We fit this profile with the same model used for the C IV line of GN-2. The broad emission component has a FWHM of 2695 ± 507 km s^{-1} and is centered 571 ± 73 km s^{-1} blueward of C IV $\lambda1548$. The narrow emission component is redshifted by $+417 \pm 73$ km s^{-1} relative to C IV $\lambda1550$. Both absorption components are blueshifted by -497 ± 46 km s^{-1} relative to the line center of their respective doublet component. The observed broad C IV/Hβ flux ratio of CEERS-7902 is 0.04 ± 0.02, a factor of 9 smaller than in GN-2. Excluding the absorption component increases the broad C IV flux, raising the ratio to 0.13 ± 0.03. Even in this case, the ratio is considerably lower than typical for BL AGNs.

The C IV emission is weakest in GN-29 (EW $= 2.1 \pm 0.6$ Å). We detect a narrow (FWHM $= 318 \pm 70$ km s^{-1}) emission line close to the red component of the doublet, with a peak flux redshifted by $+396 \pm 72$ km s^{-1} relative to the line center. We do not detect any emission line close to the blue component, placing a 3σ limiting C IV $\lambda1548$/C IV $\lambda1550$ flux ratio of < 0.9. This is below the theoretical value (2; e.g., D. R. Flower et al. 1979), as expected from resonant scattering through outflowing gas. We do not detect a broad C IV component in GN-29. If the observed broad-to-narrow C IV flux ratio matches that of GN-2, the expected broad-line flux

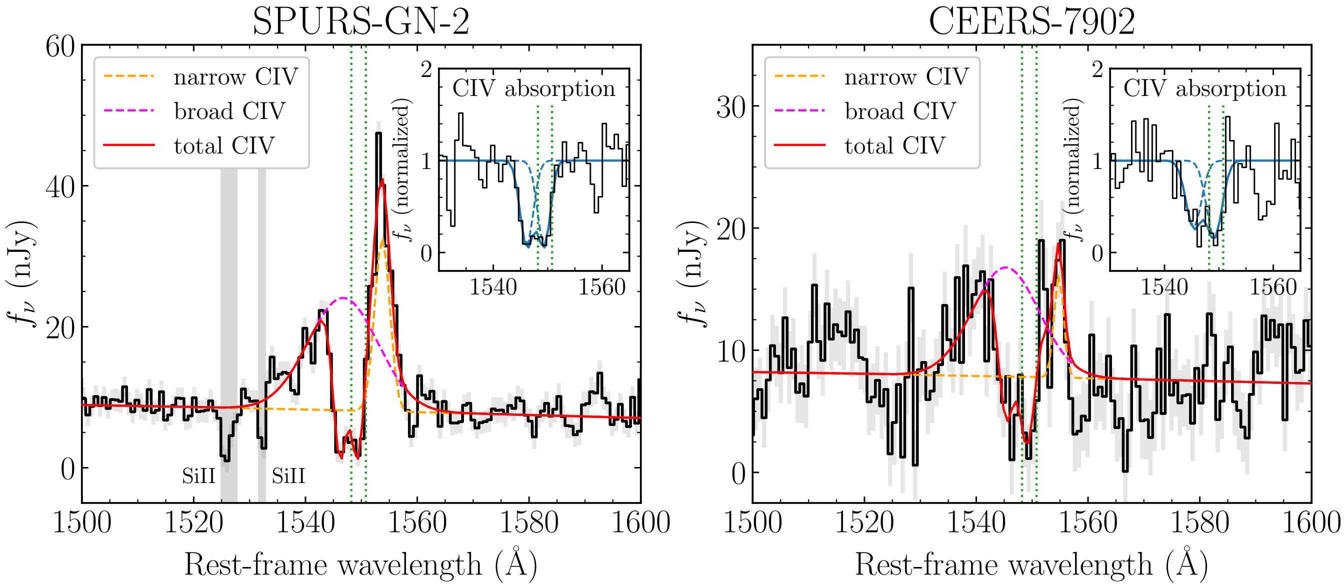

Figure 5. Fits to the C IV profiles of GN-2 (left) and CEERS-7902 (right). Each C IV profile can be fitted by a combination of four Gaussians: a broad emission (magenta dashed line), a narrow emission (orange dashed line), and two absorption components. Each absorption component is shown as the blue dashed line in the upper right corner of each panel, with the sum of the two shown as a blue solid line. The total C IV model profile of each object is shown as a red solid line. Green dotted lines show the line centers of C IV doublet. For GN-2, we mask out the regions containing Si II absorption lines.

Table 4. C IV profile fitting results of GN-2 and CEERS-7902. For each object, we list the line flux (10^{-19} erg s^{-1} cm^{-2}), EW (Å), FWHM (km s^{-1}), and velocity offset (km s^{-1}) of each component.

	SPURS-GN-2				CEERS-7902			
Line	Flux	EW	FWHM	Δv	Flux	EW	FWHM	Δv
C IV$^{a}_{\rm narrow}$	10.4 ± 1.2	10.5 ± 1.2	540 ± 57	$+568 \pm 71$	2.3 ± 1.4	2.4 ± 1.5	389 ± 189	$+417 \pm 73$
C IV$^{b}_{\rm broad}$	31.3 ± 2.5	30.7 ± 2.5	2830 ± 191	-293 ± 71	16.7 ± 3.8	17.0 ± 3.9	2695 ± 507	-571 ± 73
C IV $\lambda1548_{\rm abs}$	-8.0 ± 1.4	-7.9 ± 1.3	513 ± 64	-353 ± 39	-4.7 ± 1.5	-4.8 ± 1.5	570 ± 114	-497 ± 46
C IV $\lambda1550_{\rm abs}$	-7.6 ± 1.3	-7.4 ± 1.3	513 ± 64	-353 ± 39	-6.3 ± 1.5	-6.4 ± 1.5	570 ± 114	-497 ± 46

Note—a: The velocity offset of the narrow emission peak is calculated relative to the line center of C IV λ1550.
b: The velocity offset of the broad emission peak is calculated relative to the line center of C IV λ1548.

is 2×10^{-20} erg s^{-1} cm^{-2} with absorption. Assuming broad C IV shares the FWHM of the broad Balmer lines, our 3σ limiting flux is 3.6×10^{-19} erg s^{-1} cm^{-2}. This expected flux falls below our detection limit, so we cannot rule out broad C IV in GN-29 if it has a broad-to-narrow flux ratio similar to GN-2.

In summary, our results suggest that broad C IV profiles are present in a subset of LRDs, with line widths comparable to the broad Balmer lines. We detect broad C IV most clearly in GN-2, the optically bluest LRD in our sample. The redder LRD CEERS-7902 also shows broad C IV, but with a considerably smaller broad C IV/Hβ flux ratio. The similarity between the C IV and Hα broad-line widths hints at a common broadening origin for the two lines. If so, this suggests that broad C IV is at least partially transmitted in a subset of LRDs, perhaps indicating non-uniform covering of dense neutral gas. While our sample is small, we note that we find the largest broad C IV/Hβ ratio in GN-2, the LRD with the bluest rest-frame optical colors.

3.2. *C III], Si III], O III] Emission*

The rest-frame UV hosts a suite of emission lines sensitive to the physical conditions of the ionized gas. The SPURS observations cover the [C III], C III] $\lambda\lambda1907, 1909$ (hereafter C III]) and Si III] $\lambda\lambda1883, 1892$ (hereafter Si III]) doublets, both of which are sensitive to electron density. The spectra

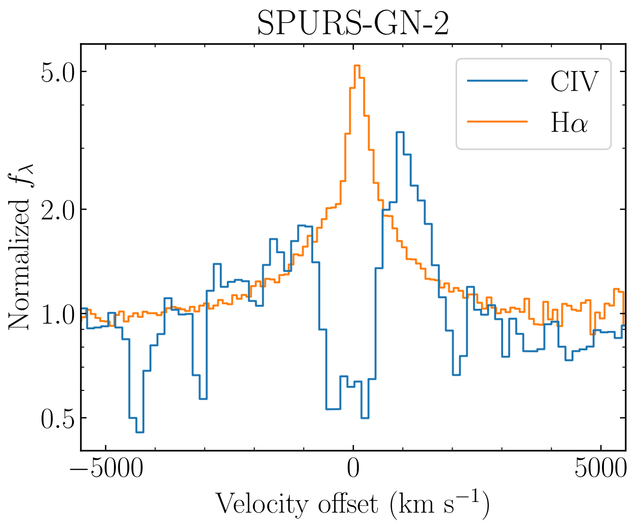

Figure 6. Comparison between broad C IV (blue) and broad Hα (orange) emission line profiles of GN-2. Flux densities are normalized to the peak flux of each broad component.

also probe the auroral O III] λλ1661, 1666 emission lines, which can be combined with [O III] λ5007 to constrain the electron temperature.

We first describe the density-sensitive lines, focusing on GN-2, the optically bluest LRD in our sample. We showed in Section 2.3 that this LRD has the largest narrow-to-broad ratio for the Balmer lines, and in Section 3.1 that it has the most prominent broad C IV. We detect strong narrow emission from C III], centered on the red (λ1909) component of the doublet. Despite the very strong C III] λ1909, we detect no [C III] λ1907 emission. Since the critical density of [C III] λ1907 (7×10^4 cm^{-3}) is lower than that of C III] λ1909 (1×10^9 cm^{-3}), this suggests the narrow-line gas in GN-2 may reach extremely high densities. The Si III] doublet suggests a similar picture: we detect the red component (λ1892), with no emission seen in the blue λ1883 component. The critical density of Si III] λ1883 (4×10^4 cm^{-3}) is lower than that of Si III] λ1892 (3×10^{10} cm^{-3}), so this is again consistent with large electron densities. We will quantify the implied densities below. Finally, we note an additional emission line at rest-frame 1914 Å, consistent with the expected position of Fe III λ1914.

To characterize the doublet line ratios, we model the C III] and Si III] line profiles in GN-2 by fitting multiple Gaussians, with the centroids fixed to the rest-frame wavelengths of each doublet. We first attempt to fit C III] with two narrow lines. We find that there is excess emission on the blue and red side of the doublet which we attribute to a broad C III] component (Figure 7). To capture the broad C III] emission, we refit the line profile with two narrow Gaussians and two broad Gaussians, each with centroids fixed to the rest-frame wavelengths of the doublet components. We mask the Fe III λ1914 line during the fit. We use the Bayesian Information Criterion to quantify whether the addition of the broad components is preferred, as is common in the literature (e.g., F. D'Eugenio et al. 2025; Z. Chen et al. 2026a; J. Matthee et al. 2026). Details of the fits are presented in Appendix A. We do find the model with narrow and broad components is strongly preferred. This model well reproduces the observed C III] profile (Figure 7). The fit to the narrow C III] λ1909 implies a large rest-frame equivalent width (EW $= 25.7 \pm 0.6$ Å), and the non-detection of [C III] λ1907 suggests a large C III]/[C III] flux ratio (> 13 at 3σ). The broad component is centered on the C III] λ1909 component with a FWHM of 2271 ± 371 km s^{-1}. The total EW of the broad component is 14 ± 4 Å, comprising 35% of the total C III] flux. We do not find the broad [C III] λ1907 component, placing a 3σ limiting broad C III]/[C III] flux ratio of > 3.6. We additionally fit the Si III] doublet with two Gaussians. In this case, we do not have the S/N to detect broad components. Our flux measurements indicate a large Si III] λ1892/λ1883 ratio (> 3.7 at 3σ).

We compute electron densities of GN-2 from the doublet ratios using `PyNeb`. Details of the density calculations are provided in Appendix C. Reproducing the C III]/[C III] flux ratios requires very high electron densities in GN-2, suggesting a lower bound of $> 1.0 \times 10^6$ cm^{-3} at 3σ. We find that the Si III] ratio is also consistent with very large densities ($> 5.0 \times 10^5$ cm^{-3}). The C III] density of GN-2 is much higher than that probed by C III] in other star-forming galaxies (left panel of Figure 8; e.g., M. W. Topping et al. 2025a; R. Singh Rai & G. Roberts-Borsani 2026; H. Umeda et al. 2026). One possibility is that we are seeing something akin to Godzilla in the Sunburst Arc, a lensed, compact source where C III] and Si III] similarly imply densities of $\gtrsim 10^6$ cm^{-3} (E. Vanzella et al. 2020; M. Pascale & L. Dai 2024; S. Choe et al. 2025), comparable to the dense Weigelt blobs surrounding the luminous blue variable η Carinae ($\sim 10^7 - 10^8$ cm^{-3}; K. Davidson et al. 1995). Another possibility is that we are seeing narrow emission from gas clouds with densities approaching those commonly found in the broad-line region ($\gtrsim 10^9$ cm^{-3}).

We also detect the C III] doublets in the other three LRDs (Figure 7), each of which reveals large integrated EWs ($18 - 23$ Å). For reference, the median C III] EW in composite spectra of star forming galaxies at $z \simeq 7$ is $\simeq 8$ Å (e.g., G. Roberts-Borsani et al. 2024; R. Singh Rai & G. Roberts-Borsani 2026; M. Tang et al. 2026a), well below what is found in the LRDs in our sample.

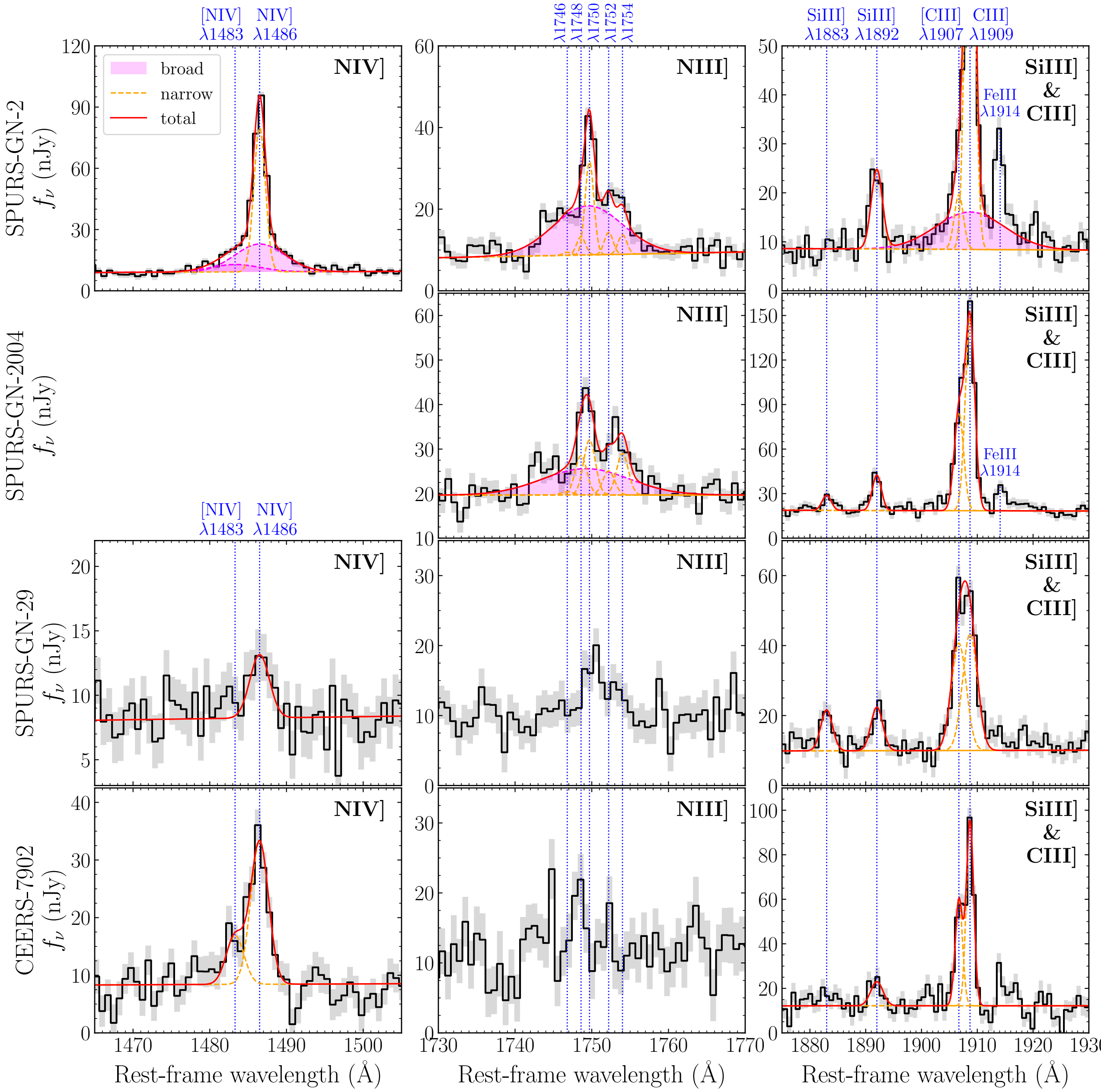

Figure 7. Density-sensitive UV emission lines (N IV], N III], Si III], C III]) of the four LRDs. We overplot the best-fit line profile to each spectrum: the narrow (FWHM < 500 km s^{-1}) components are shown as orange dashed lines, the broad components are shown as magenta shaded regions, and the sum of the best-fit profile is shown as a red solid line. Because the N III] lines of GN-29 and CEERS-7902 have relatively low S/N $(4-6)$, we do not resolve the individual components of their N III] quintuplets.

We fit the C III] line profiles using the same approach as we applied to GN-2. For these three LRDs, we do not find evidence for a broad C III] component. Our fits constrain the C III]/[C III] flux ratios: 2.0 ± 0.2 in GN-2004, 1.1 ± 0.2 in GN-29, 1.7 ± 0.2 in CEERS-7902, none of which reach the extremely large ratio seen in GN-2 (> 13). The three LRDs also reveal detection of the Si III] doublet. We measure Si III] $\lambda1892$/Si III] $\lambda1883$ flux ratios of 2.3 ± 0.9 in GN-2004, 1.1 ± 0.3 in GN-29, and > 0.9 (3σ) in CEERS-7902. Following the same techniques we used for GN-2, we derive electron densities from the doublet ratios. The C III]-based densities are $7.9^{+2.1}_{-1.6} \times 10^4$ cm^{-3} (GN-2004), $4.0^{+1.5}_{-1.0} \times 10^4$ cm^{-3} (GN-29), and $7.9^{+2.1}_{-1.6} \times 10^4$ cm^{-3} (CEERS-7902). The Si III] flux ratios reveal a consistent picture, with derived electron densities of $7.9^{+7.9}_{-2.9} \times 10^4$ cm^{-3} (GN-2004), $2.0^{+2.0}_{-1.2} \times 10^4$ cm^{-3} (GN-29), and $> 2.5 \times 10^4$ cm^{-3} (CEERS-7902). The electron densities of these LRDs

Table 5. Ionized gas properties inferred from narrow emission lines of the four LRDs.

Property	SPURS-GN-2	SPURS-GN-2004	SPURS-GN-29	CEERS-7902
n_e(N IV])/cm^{-3}	$> 2.5 \times 10^6$	–	$> 2.5 \times 10^4$	$4.0^{+1.0}_{-1.5} \times 10^5$
n_e(C III])/cm^{-3}	$> 1.0 \times 10^6$	$7.9^{+2.1}_{-1.6} \times 10^4$	$4.0^{+1.5}_{-1.0} \times 10^4$	$7.9^{+2.1}_{-1.6} \times 10^4$
n_e(Si III])/cm^{-3}	$> 5.0 \times 10^5$	$7.9^{+7.9}_{-2.9} \times 10^4$	$2.0^{+2.0}_{-1.2} \times 10^4$	$> 2.5 \times 10^4$
$T_e(O^{2+})$/K	$3.5^{+0.1}_{-0.2} \times 10^4$	$2.0^{+0.2}_{-0.1} \times 10^4$	$1.8^{+0.2}_{-0.1} \times 10^4$	$4.0^{+1.1}_{-0.9} \times 10^4$
$12 + \log$ (O/H)	$7.21^{+0.04}_{-0.04}$	$7.52^{+0.12}_{-0.10}$	$8.13^{+0.10}_{-0.10}$	$7.41^{+0.10}_{-0.05}$
$Z/Z_\odot$	$0.03^{+0.01}_{-0.01}$	$0.07^{+0.02}_{-0.01}$	$0.28^{+0.08}_{-0.06}$	$0.05^{+0.02}_{-0.01}$
N/O	$0.35^{+0.03}_{-0.02}$	$0.14^{+0.01}_{-0.02}$	$0.25^{+0.06}_{-0.06}$	$0.49^{+0.11}_{-0.09}$
(N/O)/(N/O)$_\odot$	$2.5^{+0.3}_{-0.1}$	$1.0^{+0.1}_{-0.1}$	$1.8^{+0.4}_{-0.4}$	$3.5^{+0.8}_{-0.6}$
N/C	$2.3^{+0.1}_{-0.1}$	$0.9^{+0.1}_{-0.1}$	$0.7^{+0.2}_{-0.1}$	$1.7^{+0.3}_{-0.3}$
(N/C)/(N/C)$_\odot$	$9.9^{+0.5}_{-0.6}$	$4.0^{+0.4}_{-0.3}$	$3.2^{+0.6}_{-0.6}$	$7.1^{+1.3}_{-1.1}$

NOTE—The O^{2+} temperatures provided are derived using the less dust-sensitive [O III] λ4363/[O III] λ5007 flux ratios. Using the O III] λ1666/[O III] λ5007 flux ratios (uncorrected for dust), we derive O^{2+} temperatures of $2.9^{+0.1}_{-0.1} \times 10^4$ K (GN-2), $1.8^{+0.1}_{-0.1} \times 10^4$ K (GN-2004), $1.2^{+0.1}_{-0.1} \times 10^4$ K (GN-29), and $1.6^{+0.1}_{-0.1} \times 10^4$ K (CEERS-7902).

are not as large as GN-2, but they are still elevated with respect to the typical C III] density of $z \sim 7$ galaxies ($\simeq 1 \times 10^4$ cm^{-3}, left panel of Figure 8; e.g., M. W. Topping et al. 2025a; R. Singh Rai & G. Roberts-Borsani 2026; H. Umeda et al. 2026). These results suggest that the physical conditions of the narrow line gas in LRDs are distinct from star forming galaxies at similar redshifts.

The O III] $\lambda\lambda$1661, 1666 doublet allows us to calculate the electron temperatures. We recover the doublet in all four LRDs and measure λ1661 : λ1666 ratios of 0.3 − 0.4, consistent with expectations from theoretical transition probabilities (0.4; C. Froese Fischer & H. P. Saha 1985). We measure electron temperatures from the ratio of the O III] λ1666 and [O III] λ5007 fluxes, assuming the densities derived from C III]/[C III] flux ratios. The temperatures are derived using `PyNeb` (see the Appendix C for more details). In our initial measurements, we do not apply dust correction for the O III] λ1666/[O III] λ5007 flux ratio. For GN-2 and GN-2004, the temperatures derived from O III] ($1.8 - 2.9 \times 10^4$ K) are consistent with that inferred from [O III] λ4363 ($2.0 - 3.5 \times 10^4$ K). For GN-29 and CEERS-7902, the temperatures derived based on O III] ($1.2 - 1.6 \times 10^4$ K) are lower than those inferred from [O III] λ4363 ($1.8 - 4.0 \times 10^4$ K). Since these are the two reddest LRDs in our sample, we suggest that one possible explanation is dust. We can estimate the reddening that would be required to bring the O III]-based temperature in line with the [O III] λ4363 temperature. To do so, we calculate the O III] λ1666 flux that we would have expected using the [O III] λ4363-based temperature. The comparison of this expected value with that which we observe allows us to estimate the dust attenuation required to make the two measurements consistent. Assuming the Small Magellanic Cloud (SMC) extinction law of K. D. Gordon et al. (2003), we find that only modest dust attenuation is required for GN-29 ($A_V = 0.46$) and CEERS-7902 ($A_V = 0.75$). Adopting the flatter extinction law of J. A. Cardelli et al. (1989), however, yields substantially larger attenuation values of $A_V = 0.99$ and 1.62 for GN-29 and CEERS-7902, respectively.

3.3. *N IV] and N III] Emission*

The [N IV], N IV] $\lambda\lambda$1483, 1486 doublet (hereafter N IV]) has been detected in a subset of the galaxies and AGN observed by JWST. Three of the LRDs in our sample (GN-2, GN-29, CEERS-7902) have spectra that cover N IV]. All four LRD spectra cover the lower-ionization N III] quintuplet, comprising five emission lines in the range 1746 − 1754 Å.

We first consider the N IV] complex in GN-2, given its distinct spectral properties within our sample (see Section 2.3, 3.1, and 3.2). N IV] emission is well detected in its spectrum (Figure 4). The narrow emission is centered on N IV] λ1486, with no corresponding feature at [N IV] λ1483. A broad N IV] component is also present. We fit the N IV] profile of GN-2 with two narrow and two broad Gaussians (see Appendix A for details). The resulting model reproduces the profile well (Figure 7). The narrow N IV] λ1486 emission is very strong (EW $= 14.5 \pm 0.7$ Å), and the non-detection of the blue component indicates a large N IV]/[N IV] flux ratio (> 18 at 3σ). The broad N IV] component in GN-2 has FWHM

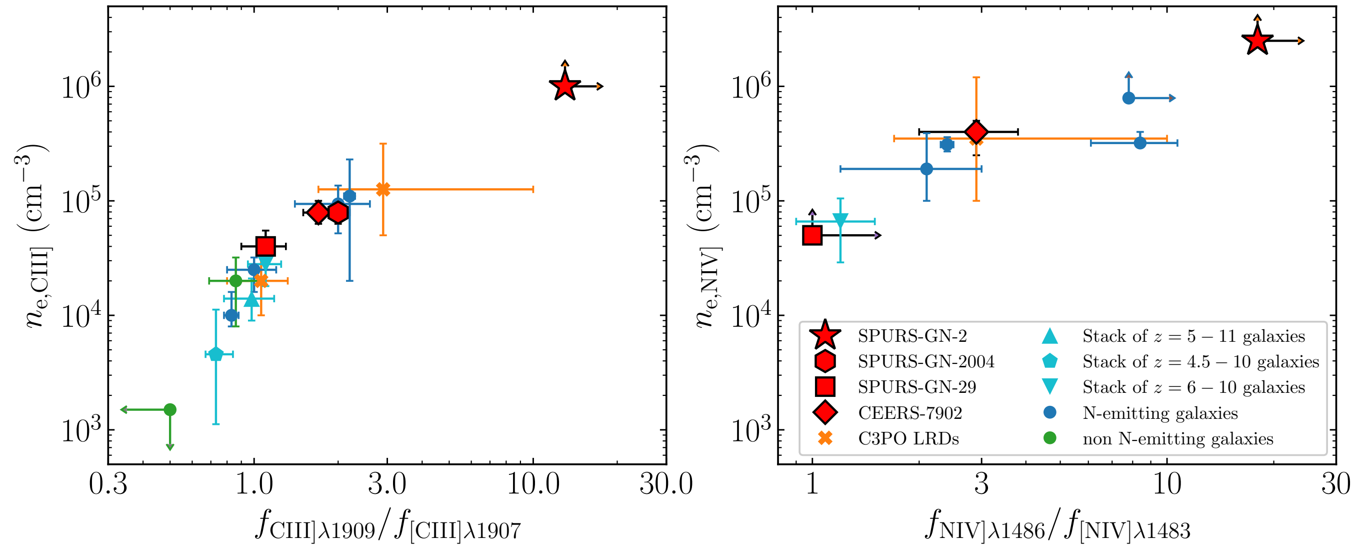

Figure 8. Electron densities ($n_{\rm e}$) of four LRDs (GN-2: red star; GN-2004: red hexagon; GN-29: red square; CEERS-7902: red diamond) inferred from C III] $\lambda1909$/[C III] $\lambda1907$ (left) and N IV] $\lambda1486$/[N IV] $\lambda1483$ (right) flux ratios. For comparison, we overplot C3PO LRDs (C. Papovich et al. 2026, orange cross symbols), average densities inferred from composite spectra of galaxies ($z = 5-11$, M. W. Topping et al. 2025b, cyan triangle; $z = 4.5-10$, H. Umeda et al. 2026, cyan pentagon; $z = 6-10$, R. Singh Rai & G. Roberts-Borsani 2026, cyan upside down triangle), individual N IV] or N III] emitters (blue circles; M. W. Topping et al. 2024, 2025b; Z. Chen et al. 2026a) and non nitrogen emitters (green circles; M. W. Topping et al. 2025b).

$= 1514 \pm 137$ km s^{-1} comprising 45% of the total N IV] flux and is centered on N IV] $\lambda1486$.

We note that similar broad N IV] components were recently discovered in several nitrogen emitters that are not LRDs, including the luminous galaxy GN-z11 (Z. Chen et al. 2026a). The origin of this broad component has been debated, with dense Wolf-Rayet (WR)-like winds from very massive stars and AGN-driven outflows both proposed as possible explanations. Our detection of a comparable broad N IV] component in GN-2 extends this phenomenon to the LRD population, possibly lending support to an AGN-driven origin for the broad N IV] emission, at least in this source.

The N IV]/[N IV] doublet ratio provides an additional constraint on the electron density in GN-2. We compute the density using `PyNeb`, following the methods described in Appendix C. The flux ratio of the narrow lines (> 18 at 3σ) points to an extremely large density ($> 2.5 \times 10^6$ cm^{-3}) for the nitrogen-emitting gas. While UV nitrogen lines commonly trace large densities (M. W. Topping et al. 2024, 2025b; Z. Chen et al. 2026a; R. Singh Rai & G. Roberts-Borsani 2026), this measurement places GN-2 as the highest density yet seen in a narrow N IV] emitter (right panel of Figure 8). Along with the C III] and Si III] constraints in Section 3.2, this result builds on the picture that the narrow rest-frame UV lines in GN-2 emerge from extremely dense gas that has almost never before been seen in typical star forming galaxies.

We also detect N IV] in CEERS-7902 and GN-29. The line properties are measured in the same manner as for GN-2, but in these cases we do not recover broad profiles at the current S/N. CEERS-7902 presents N IV] with an integrated EW of 11.5 ± 0.9 Å and a large N IV]/[N IV] ratio (2.9 ± 0.9). The N IV] in GN-29 is weaker and has a lower S/N. We measure an integrated EW $= 1.9 \pm 0.7$ Å. The emission is centered on the red component, but with our current sensitivity limits, we can only place a rough lower bound on the N IV]/[N IV] ratio (> 1.0 at 3σ). We compute N IV]-based electron densities from the doublet ratios. The results reveal a large density in $4.0^{+1.0}_{-1.5} \times 10^5$ cm^{-3} in CEERS-7902. In GN-29, the limit does not strongly constrain the density ($> 2.5 \times 10^4$ cm^{-3}). While the N IV] density in CEERS-7902 is not as large as that in GN-2, it is larger than the N IV]-based density derived from the composite spectrum of $z = 6-10$ galaxies (7×10^4 cm^{-3}, R. Singh Rai & G. Roberts-Borsani 2026; right panel of Figure 8).

We detect N III] emission in all four LRDs (Figure 4). GN-2 and GN-2004 have high S/N (27 for GN-2, 17 for GN-2004) allowing us to model individual lines within the N III] $\lambda1746-1754$ quintuplet. As discussed in Appendix A, we also find evidence for a broad N III] component in these two objects. We model the observed profiles with five narrow Gaussians and one broad Gaussian. Following Z. Chen et al. (2026a), the five narrow components are centered at the rest-frame wavelengths of the quintuplet lines, share a common line width, and have fixed flux ratios of $f_{\rm NIII]\lambda1746}/f_{\rm NIII]\lambda1752} = 0.14$ and $f_{\rm NIII]\lambda1748}/f_{\rm NIII]\lambda1754} = 0.95$, corresponding to their theoretical values. The centroid and width of the broad component are left free.

We show the resulting model of the N III] quintuplet in Figure 7 and line measurements in Table 3. As described in Appendix A, the fits prefer a broad N III] component in GN-2 (FWHM $= 1797 \pm 219$ km s^{-1}) and GN-2004 (FWHM $= 2271 \pm 649$ km s^{-1}). This suggests a fast-moving component of nitrogen that includes both N IV] and N III]. One complication in interpreting the broad N III] profile is the potential presence of Fe II $\lambda1743$ emission. To test the potential impact of Fe II on our fits, we simultaneously fit the N III] profile with five narrow Gaussians and an additional Gaussian for the Fe II $\lambda1743$ component. We are able to recover the N III] line profile, provided the Fe II $\lambda1743$ component is very strong, with a flux of $3.9 \pm 0.9 \times 10^{-19}$ (GN-2) and $2.6 \pm 0.9 \times 10^{-19}$ erg s^{-1} cm^{-2} (GN-2004). In this scenario, the N III] broad profile would be weaker. However, we consider this unlikely: the implied Fe II $\lambda1743$ emission would be well above the values expected given the measured flux of Fe II $\lambda1786$ and the typical $\lambda1743/\lambda1786$ flux ratios (~ 0.01 based on the ratio between Einstein A coefficients). We thus conclude the broad N III] component is the most likely explanation for the observed profile, but we caution that there remains some uncertainty in its interpretation. Using the narrow line decompositions of the quintuplet, we can constrain the electron density of the N III]-emitting gas. However, in practice we find that the line ratios do not unambiguously constrain the density, and as a result we focus our analysis on densities derived from the doublet ratios discussed above.

Finally, we characterize the N III] emission in the other two LRDs (GN-29, CEERS-7902). These sources, the two redder LRDs in our sample, show weak N III] emission with S/N $= 4 - 6$. The sensitivity of these spectra is not sufficient to meaningfully characterize the presence of broad components. The integrated N III] EWs are 5.0 ± 0.8 Å (GN-29) and 4.1 ± 1.0 Å (CEERS-7902), comparable to those derived for the narrow lines in GN-2 (6.3 ± 0.2 Å) and GN-2004 (3.6 ± 0.2 Å).

The detections of N IV] and N III] together with the other rest-frame UV emission lines allow us to infer the relative nitrogen abundances in the four LRDs. We derive N/O and N/C ratios following the procedures described in Z. Martinez et al. (2025). Here we summarize the results, but our detailed methodology is described in Appendix C. We find that the four LRDs have nitrogen-enhanced abundance patterns, with N/O $= 0.35^{+0.03}_{-0.02}$ (GN-2), $0.14^{+0.01}_{-0.02}$ (GN-2004), $0.25^{+0.06}_{-0.06}$ (GN-29), and $0.49^{+0.11}_{-0.09}$ (CEERS-7902). These correspond to super-solar N/O ratios ($1.0 - 3.5$ N/O$_\odot$). We also derive large N/C ratios, $2.3^{+0.1}_{-0.1}$ (GN-2), $0.9^{+0.1}_{-0.1}$ (GN-2004), $0.7^{+0.2}_{-0.1}$ (GN-29), and $1.7^{+0.3}_{-0.3}$ (CEERS-7902), corresponding to $3.2 - 9.9$ N/C$_\odot$. The relative abundances are comparable to the N IV] emitters in the galaxy population at high redshift (e.g., M. Castellano et al. 2024; D. Schaerer et al. 2024; P. Senchyna et al. 2024; M. W. Topping et al. 2024, 2025b; R. Navarro-Carrera et al. 2025). This suggests some similarity between the LRDs and the broader class of nitrogen emitters. We will come back to generalize this result in Section 5.1.

3.4. *Mg II Emission*

Mg II $\lambda\lambda2796, 2803$ is a resonant doublet which often appears broad in the spectra of AGN. In AGN, it arises in the low-ionization broad-line region alongside the broad Balmer series emission lines (e.g., H. Netzer 1980; D. E. Vanden Berk et al. 2001). Additionally, we may expect to detect narrow Mg II from narrow line regions in the LRDs. As Mg II can be resonantly scattered by dense cool $T \sim 10^4$ K gas, the emergent profile and doublet ratio of narrow lines are sensitive to gas kinematics, dust attenuation and column density (e.g., D. K. Erb et al. 2012; A. Henry et al. 2018; J. Chisholm et al. 2020).

In GN-2, we detect a narrow Mg II $\lambda2796$ emission line along with an absorption feature. The peak flux of Mg II $\lambda2796$ is redshifted by $+300 \pm 66$ km s^{-1}, while the centroid of Mg II absorption is blueshifted by -264 ± 74 km s^{-1} with respect to the line center of Mg II $\lambda2796$, consistent with a P-Cygni profile. We measure a Mg II $\lambda2796$ EW of 4.3 ± 0.9 Å. We do not detect the Mg II $\lambda2803$ component, placing a 3σ lower limit of > 1.5 to the Mg II $\lambda2796$/Mg II $\lambda2803$ flux ratio. A P-Cygni profile indicates continuum radiation is scattered by outflowing, optically thick, Mg II gas (J. X. Prochaska et al. 2011; X. Xu et al. 2023a; S.-J. Chang & M. Gronke 2024).

We do not detect broad Mg II in any of the four LRDs. Assuming the broad Mg II FWHM is the same as the broad Hβ and integrating over $2\times$ FWHM$_{\rm broad}$, we place 3σ limits on the broad Mg II/Hβ flux ratio for the four LRDs ($< 0.06 - 0.10$). These are far below those of typical BL AGNs ($\simeq 1.5$; e.g., P. J. Francis et al. 1991; M. S. Brotherton et al. 2001; D. E. Vanden Berk et al. 2001). The absence of broad Mg II may reflect a combination of factors, reviewed in M. Tang et al. (2026b). In particular, owing to the frequency dependence of the photoionization cross-section, Mg II photons are more likely to be absorbed than C IV photons as they pass through a dense layer of $n = 2$ hydrogen. This wavelength-

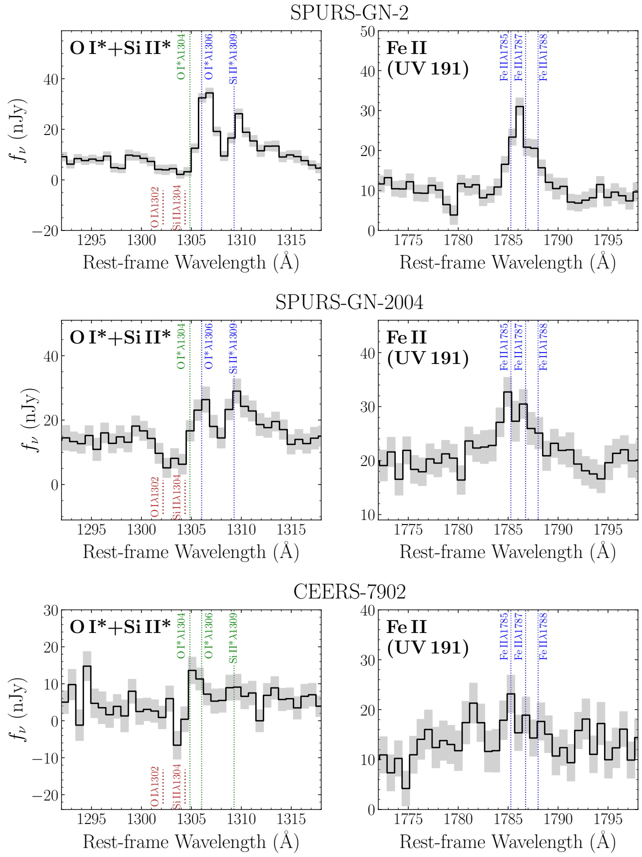

Figure 9. O I* λ1306+Si II* λ1309 (left panels), and Fe II UV 191 (right panels) fluorescent emission lines of GN-2, GN-2004, and CEERS-7902. We mark each detected emission line in blue, undetected emission lines in green, and interstellar absorption in red.

dependent opacity offers a natural explanation for why broad C IV can be partially transmitted through a sightline in which broad Mg II is fully suppressed.

3.5. *O I, Fe II, and Si II Emission*

The LRDs also show a suite of low-ionization UV emission lines that provide evidence for dense neutral gas absorbing UV photons. We detect both O I and Fe II emission lines, that are increasingly detected in LRDs (e.g., I. Labbé et al. 2024; F. D'Eugenio et al. 2025; R. Tripodi et al. 2025b; M. Tang et al. 2026b; A. Torralba et al. 2026a), and report the first detections of Si II fine-structure emission in LRDs. We show the detected lines in Figure 9 and list their derived flux, EW, and FWHM in Table 3.

We detect strong O I emission in two of the four LRDs. GN-2 and GN-2004 both show a O I* λ1306 fine-structure emission line (EW $= 6.8 \pm 0.4$ Å and EW $= 1.3 \pm 0.4$ Å respectively). In GN-2 we also clearly detect the rare semi-forbidden line O I] λ1641 (EW $= 2.2 \pm 0.9$ Å), which we resolve from He II λ1640 emission. O I] λ1641 emission has not, to our knowledge, been previously reported in star-forming galaxies, but is seen in symbiotic star outflows (S. N. Shore & G. M. Wahlgren 2010) and has been detected in the Godzilla cluster in the Sunburst Arc (M. Pascale & L. Dai 2024; S. Choe et al. 2025), and implies extremely high O I column densities. Both O I* λ1306 and O I] λ1641 arise from decays from the $3s\,^3S^0$ state, which is populated by continuum absorption at 1302 Å by oxygen atoms in the ground state, and boosted by Lyβ fluorescence of the $3d\,^3D^0$ excited state – requiring high H I column densities to trap Lyβ (e.g., J. Kwan & J. H. Krolik 1981; Y. Matsuoka et al. 2007; S. N. Shore & G. M. Wahlgren 2010). To estimate the implied column density, we consider the conditions required to detect strong O I] λ1641 emission. The relative rates of spontaneous emission in the two channels differ by $A_{1306}/A_{1641} \sim 10^5$, thus our detection of λ1641 emission at comparable strength to λ1306 emission implies a very high optical depth in the ground state to suppress O I λ1302, 1304, 1306 emission: $\tau \gtrsim 10^5$, consistent with the strong absorption we detect at 1302 Å (see Section 4). Conservatively assuming a Doppler parameter $b = 10$ km s^{-1} this implies a ground state OI column density $N_{\rm OI} \gtrsim 3 \times 10^{18}\,{\rm cm}^{-2}$. Assuming solar abundance ratios and $0.03 - 0.28\,Z_\odot$ metallicity (see Section 2.3) suggests an extremely high H I column density around the Lyβ-emitting region: $N_{\rm HI} \gtrsim 10^{22.5-23.0}\,{\rm cm}^{-2}$.

In GN-2 and GN-2004 we also detect strong Si II* λ1309 fine-structure emission (EW $= 5.1 \pm 0.4$ Å and 2.0 ± 0.3 Å, respectively). This line typically arises from pumping by the UV continuum: photons absorbed by the Si II λ1304 resonance transition preferentially decay to the fine-structure level rather than back to the ground state, producing λ1309 emission. In the optically thick limit, we expect the emission EW to be equal to the absorption EW, however in star-forming galaxies the emission EW is typically weaker, likely due to scattering out of slit spectrographs into an extended halo and absorption by dust (e.g., A. E. Shapley et al. 2003; T. Jones et al. 2012). Strikingly, in GN2, the Si II* λ1309 emission EW is stronger than the resonant line absorption (see Section 4): suggesting low dust opacity and an additional excitation source. One possibility is that photons emitted as O I* λ1304 are absorbed by the ground state Si II λ1304. As the lines are separated by only 100 km s^{-1}, moderately broad O I emission could thus boost the excitation of Si II.

We detect permitted Fe II emission in both the FUV and NUV of the LRD spectra. In the UV, GN-2, GN-2004 and CEERS-7902 all show strong emission

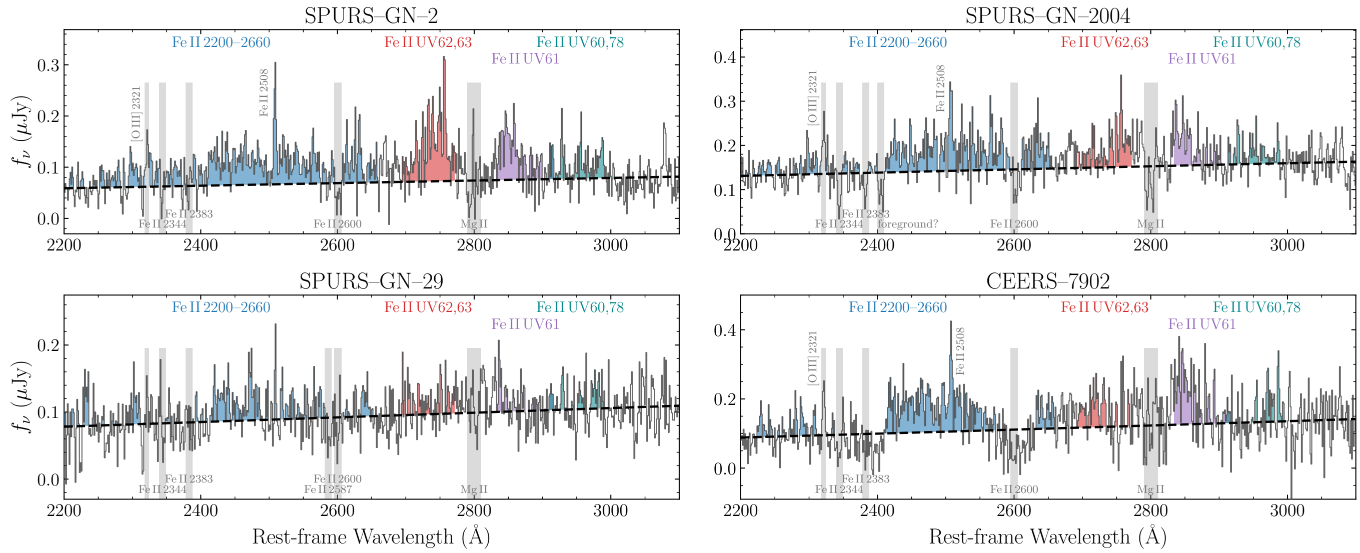

Figure 10. The NUV Fe II complexes of the four LRDs. The colored shaded regions show the emission components associated with the unresolved Fe II $\lambda2200-2600$ blend, and the Fe II UV62,63, Fe II UV61, and Fe II UV60,78 complexes. The black dashed line shows the continuum model from our `fantasy` fit. The gray shaded bands mark individual emission lines and absorption features seen in our spectra.

in the Fe II UV 191 multiplet at 1785, 1787, 1788 Å. The total multiplet flux Fe II λ1786/broad Hβ ratio is 0.11 ± 0.02, 0.08 ± 0.01, and 0.07 ± 0.01 for GN-2, GN-2004, and CEERS-7902, respectively. These ratios are $2-4\times$ larger than the typical type I AGN value of 0.03 (D. E. Vanden Berk et al. 2001). Fe II λ1786 emission can be enhanced by Lyα fluorescence (S. Johansson & C. Jordan 1984), which may explain the high Fe II λ1786/broad Hβ ratio. In GN-2 and GN-2004, we also detect Fe III λ1914 emission, which can also be pumped by Lyα (S. Johansson et al. 2000). This line has previously been reported in η Carinae (S. Johansson et al. 2000) and the Sunburst arc (E. Vanzella et al. 2020). Similarly to the fluorescence excitation channel for O I emission described above, pumping these transitions requires a high H I column density to trap Lyα photons (e.g., T. A. A. Sigut & A. K. Pradhan 2003; T. A. A. Sigut et al. 2004).

We also detect a forest of strong permitted NUV Fe II emission in all four LRDs, which we plot in Figure 10. These lines have previously been reported in prism spectra of LRDs (F. D'Eugenio et al. 2025; M. Ando et al. 2026; P. G. Pérez-González et al. 2026; A. Torralba et al. 2026a), but are resolved here with grating spectroscopy for the first time. Strong NUV Fe II is commonly seen in AGN, where it is linked to high accretion rates and is often accompanied by signatures of outflows in broad C IV (M. Vestergaard & B. J. Wilkes 2001; K. M. Leighly & J. R. Moore 2004), and has also been detected in η Car (e.g., R. Viotti et al. 1989). In both contexts, the emission is thought to be powered by a combination of continuum and Lyα fluorescence, as well as collisional excitation (e.g., S. Johansson & V. S. Letokhov 2001; T. A. A. Sigut & A. K. Pradhan 2003).

In AGN, permitted Fe II is typically broad, and thought to arise in the BLR (e.g. B. J. Wills et al. 1985; M. Vestergaard & B. J. Wilkes 2001; A. J. Barth et al. 2013). However, the emission we detect is significantly narrower than the broad Balmer lines (FWHM$\approx$ $188-464\ \mathrm{km\,s^{-1}}$ for isolated emission lines in GN-2, GN-2004 and CEERS-7902). To characterize the strength of the Fe II emission we measure their EWs by directly integrating their continuum-normalized profiles. We follow M. Ando et al. (2026) and jointly fit the NUV continuum and emission components. Specifically, we fit a power-law continuum, $f_\nu = A\,(\lambda/2500\,)^\alpha$, together with the M. Vestergaard & B. J. Wilkes (2001) UV Fe II template, and the Fe III UV47 template over $2000-3500$ Å using `fantasy` (D. Ilić et al. 2023). We normalize the spectrum by the fitted power-law continuum, and integrate the continuum-normalized spectrum over the windows $2200-2660$ Å, $2692.8-2772.7$ Å, $2833.4-2917.5$ Å, and $2907.9-3002.6$ Å (with Mg II masked over a window of 10 Å) to measure the equivalent widths of the four NUV Fe II complexes: the unresolved Fe II $\lambda2200-2600$ blend, and the Fe II UV62,63, Fe II UV61, and Fe II UV60,78 multiplet groups, where we adopt the extents of each multiplet in the line list of D. Ilić et al. (2023). We report the measured EW in Table D.1 in Appendix D.1.

GN-2 and CEERS-7902 show exceptionally strong NUV Fe II emission, with total equivalent widths of 356 ± 24 Å and 194 ± 26 Å, respectively, placing them

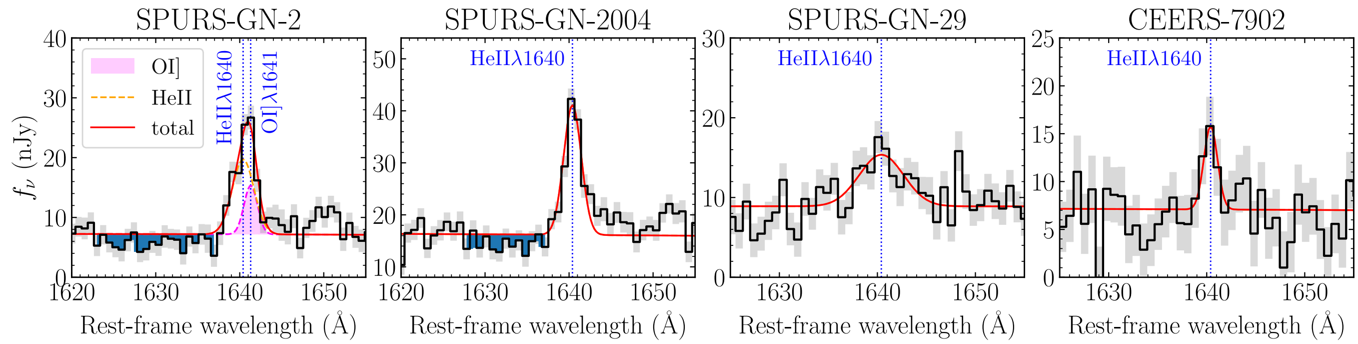

Figure 11. He II emission line profiles of the four LRDs. In GN-2, we also detect the O I] λ1641 emission line, which is shown as the magenta shaded region. The He II emission can be described by a single narrow Gaussian except for GN-29, where we measure a significantly broader line width (FWHM $= 929 \pm 211$ km s^{-1}). We find tentative blueshifted He II absorption features in GN-2 and GN-2004, which are highlighted by blue shaded regions.

among the strongest NUV Fe II emission reported in LRDs to date (e.g., I. Labbé et al. 2024; M. Ando et al. 2026; A. Torralba et al. 2026a). The remaining two LRDs show weaker NUV Fe II emission, with total equivalent widths of 141 ± 12 Å for GN-2004 and 72 ± 16 Å for GN-29. Three of the LRDs (GN-2, GN-2004, and CEERS-7902) also show extremely strong narrow Fe II λ2508 emission (EW $= 6 - 10$ Å), a feature which has also been detected in η Car (K. Davidson et al. 1995). This line can also be pumped by Lyα emission, however, the relevant Fe II transition is offset from the Lyα resonance by $+630$ km s^{-1} (S. Johansson & C. Jordan 1984; S. Johansson & F. W. Hamann 1993; F. Hamann 2012): the detection of this line implies broad Lyα emission reaches a dense region containing Fe II in these three LRDs.

3.6. *He II Emission*

The He II λ1640 line provides a sensitive measure of the ionizing spectrum associated with LRDs. Above we have shown that broad C IV is present in several LRDs, suggesting that if the ionizing spectrum is hard enough, we might also see hints of comparably broad He II emission. Additionally, we may expect strong emission from the ionizing sources in the narrow line regions of LRDs. While previous work has constrained the strength of He II λ4686 (F. D'Eugenio et al. 2025; M. Brazzini et al. 2026; X. Ji et al. 2026a; B. Wang et al. 2026), the UV line is $\simeq 8\times$ stronger, making it easier to constrain in individual sources. We detect He II λ1640 in all four LRDs and describe the range of line profiles below.

GN-2 displays a complex asymmetric He II profile (Figure 11) due to the blending with the O I] λ1641 emission line presented in Section 3.5. To decompose the He II and O I] emission, we fit the entire emission line profile with two Gaussians. We fix the centroids to the rest-frame wavelengths of He II and O I], and we fix the line width of O I] equal to that of O III] λ1666. We find the model reproduces the emission well and is significantly preferred over a single Gaussian including only He II (Appendix A). We derive a He II λ1640 EW of 5.6 ± 1.5 Å from the deblended fit. We find the He II is broader (FWHM $= 468 \pm 91$ km s^{-1}) than (semi-)forbidden UV emission lines (FWHM $\simeq 340$ km s^{-1}), but much narrower than the broad C IV or broad Balmer emission lines. We also note tentative evidence for blueshifted He II λ1640 P-Cygni absorption (EW $= -3.3 \pm 0.8$ Å) extending to ≈ 1624 Å (Figure 11), corresponding to a velocity of ≈ -2900 km s^{-1}, which suggests the presence of a high-velocity wind. While Fe II* transitions falling in this window may contribute weakly, these discrete, unresolved features can reproduce neither the full velocity extent nor the smooth, continuous shape of the blueshifted He II absorption we find.

In the other three LRDs, we do not find evidence for a significant contribution from O I] λ1641, so we characterize their lines with single Gaussian fits. We find none of the LRDs have He II emission with line widths approaching the broad components of the Balmer emission lines or C IV. GN-29 (EW $= 4.1 \pm 1.2$ Å) presents the broadest He II emission line in the sample, with a FWHM of 929 ± 211 km s^{-1}, though its He II emission is still significantly narrower than its broad Balmer emission lines. Such a broad He II profile has also been seen in several $z \sim 6 - 11$ galaxies (e.g., Z. Chen et al. 2026a; D. Yang et al. 2026) and can be explained via a significant contribution from strong stellar winds in WR or very massive star (VMS) populations (e.g., D. Schaerer 1996; R. Chandar et al. 2004; J. Brinchmann et al. 2008; T. Nanayakkara et al. 2019; P. Senchyna et al. 2021), which we discuss further in Section 6.3. GN-2004 (EW $= 3.5 \pm 0.8$ Å) has a He II FWHM of 424 ± 67 km s^{-1}, which is slightly broader than its forbidden emission lines (FWHM $\simeq$ 330 km s^{-1}). As in GN-2, it shows a tentative blueshifted P-Cygni absorption (rest-frame EW $= -1.6 \pm 0.8$ Å), though extending to a lower maximum velocity of $\approx$ 2200 km s^{-1} ($\approx$ 1628 Å). We additionally see a broad redshifted excess over the single-Gaussian model (up to 1648 Å; Figure 11), suggestive of P-Cygni emission, although the BIC still favors the single Gaussian over the narrow+broad two-component fit. In CEERS-7902, He II is marginally detected (EW $= 2.0 \pm 1.2$ Å), but it also has a narrow profile with FWHM ($= 291 \pm 127$ km s^{-1}) similar to that of forbidden lines (FWHM $\simeq$ 290 km s^{-1}). The range of narrow He II λ1640 EWs in the four LRDs ($2.0 - 5.6$ Å) is larger than the average He II EW measured in the composite spectrum of $6 - 10$ galaxies (1.7 Å; R. Singh Rai & G. Roberts-Borsani 2026). Such strong He II has been identified in a few individual galaxies (e.g., A. J. Bunker et al. 2023; M. W. Topping et al. 2024, 2025b; Z. Chen et al. 2026a).

While we do not detect broad He II with similar FWHMs to the broad Balmer lines in the four LRDs, the deep SPURS spectra allow us to place upper limits on broad He II emission. To derive upper limits, we assume the broad He II emission FWHM is the same as broad Hβ (FWHM$_{\rm broad} = 3000 - 4000$ km s^{-1}) and integrate the error spectrum in quadrature over a spectral window spanning 2$\times$ FWHM$_{\rm broad}$. We place 3σ limiting fluxes of $3.1 - 5.1 \times 10^{-19}$ erg s^{-1} cm^{-2} for broad He II emission for the four LRDs. These correspond to broad He IIλ1640/Hβ flux ratios of $< 0.036 - 0.070$, significantly below the typical value seen in type I AGNs ($\simeq 0.5$; e.g., P. J. Francis et al. 1991; M. S. Brotherton et al. 2001; D. E. Vanden Berk et al. 2001). Given the detection of broad C IV, the absence of broad He II may suggest a soft ionizing spectrum.

3.7. *Lyα Emission*

Due to its high cross-section for resonant scattering, Lyα emission is a particularly sensitive tracer of the column density and kinematics of the neutral hydrogen through which it scatters, as well as of dust attenuation (e.g., D. A. Neufeld 1990; A. Verhamme et al. 2006). Broad Lyα emission is commonly seen in AGN, arising in the same region as broad Balmer lines. Broad Lyα has been reported in two LRDs with deep grating spectroscopy (T. Morishita et al. 2026; M. Tang et al. 2026b), but most LRDs observed to date show narrow Lyα emission, more consistent with formation outside of a BLR (A. Torralba et al. 2026b; Y. Kageura et al. 2026; S. Geris et al. 2026). Our observations do not cover Lyα in two of the LRDs (GN-2, GN-2004). We do not detect Lyα in CEERS-7902, which also shows among the strongest Lyα-pumped Fe II emission features in the sample, however, we do recover it in GN-29.

The rest-frame UV spectrum of GN-29 reveals a strong Lyα emission line (S/N = 15, EW $= 26 \pm 2$ Å). The Lyα peak flux is redshifted by $+284 \pm 92$ km s^{-1} with respect to the line center, as commonly seen in Lyα-emitting galaxies at $z \sim 7$ (e.g., M. Tang et al. 2024; G. C. Jones et al. 2025). The FWHM of Lyα (495 ± 28 km s^{-1}) is wider than that of narrow (semi-)forbidden emission lines (FWHM $\simeq$ 320 km s^{-1}), but significantly narrower than the broad Balmer lines. We estimate the Lyα escape fraction ($f_{\rm esc,Ly\alpha}$) using the dust-corrected narrow Hα line to predict the intrinsic Lyα luminosity ($L^{\rm int}_{\rm Ly\alpha} = 8.7 \times L_{\rm H\alpha}$; e.g., M. Hayes 2015; A. Henry et al. 2015). The narrow Hα/Hβ flux ratio (5.2 ± 1.3) is larger than the intrinsic value assuming case B recombination (2.76 for $T = 2{\times}10^4$ K; D. E. Osterbrock & G. J. Ferland 2006). This suggests substantial dust attenuation to the narrow-line gas assuming the SMC extinction law ($A_V =$ 1.7). We then derive a Lyα escape fraction of 0.010 ± 0.002. If we assume the modest dust attenuation derived in Section 3.2 ($A_V = 0.46$), we will obtain a Lyα escape fraction of 0.024 ± 0.006.

3.8. *Very High Ionization Line Emission*

Very high ionization emission lines in the rest-frame UV (N V, [Ne IV], [Ne V]) are often seen in the spectra of AGN, probing hard radiation fields with ionizing photon energies $> 64 - 97$ eV. These lines have been identified in a handful of LRDs (I. Labbé et al. 2024; M. Tang et al. 2025, 2026b; H. Treiber et al. 2025), but remain undetected in the majority of the LRD population. The SPURS dataset provides our most stringent constraints yet on very high ionization lines in LRDs. We search for N V $\lambda\lambda$1239, 1243, [Ne IV] $\lambda\lambda$2422, 2424, and [Ne V] λ3427 emission in the deep G140M and G235M spectra of the four LRDs.

We do not detect any of the [Ne IV] or [Ne V] emission lines in the SPURS spectra of the four LRDs. With the G140M spectra, we place 3σ limiting EWs of $< 1.4 - 3.7$ Å for each individual component of [Ne IV]. [Ne V] is shifted to G235M spectra. We place 3σ limiting EWs of $< 2.5 - 5.8$ Å for the [Ne V] λ3427 emission lines. These EW limits are similar to those measured from a handful of LRDs with the deepest rest-frame UV NIRSpec grating coverage (M. Tang et al. 2025).

The N V doublet falls within the G140M spectra of all four LRDs. For GN-2 and GN-29, we do not detect N V, placing 3σ limiting EWs of $< 1.7 - 2.8$ Å on each individual component of the doublet. However, GN-2 shows a tentative (S/N = 2.1) emission line peaked at rest-frame 1248 Å, offset by $+1320$ km s^{-1} from N V λ1243, with a broad FWHM of 1258 ± 530 km s^{-1} and an EW of 1.5 ± 0.7 Å (adopting the continuum from the power-law fit of the FUV continuum). As we will discuss below (see Section 4.2), this wavelength region is strongly impacted by damped Lyα absorption from high column density H I gas, requiring this feature to have a very large intrinsic EW ($\approx$ 8 Å) and a very broad profile extending to $\approx$ 2000 km s^{-1} from the line center if it corresponds to N V. The N V lines of GN-2004 fall at the short-wavelength end of the G140M spectrum, where the sensitivity is very low (Figure 13), so we are unable to place any constraint on them. Previously, an emission feature near the position of N V λ1239 was reported in CEERS-7902 from the Cycle 2 GO 4287 program (EW = 27.9 ± 3.4 Å; M. Tang et al. 2025). No such emission line is found in the SPURS G140M spectrum; the non-detection yields a 3σ limiting EW ($<$ 2.0 Å) well below the previously reported value. It is possible that the slightly varied spatial positions covered between the Cycle 2 and Cycle 4 observations account for the difference. Alternatively, it is conceivable that the emission feature in the earlier program is spurious. By checking the individual exposures of the GO-4287 data, reprocessed following the procedures described in Section 2.2, we find that the emission feature previously seen is present only in the last of the three exposures, while the same spatial position is saturated in the second exposure. This suggests that it may be possible that the emission feature was due to persistence from a saturated cosmic-ray hit.

4. INTERSTELLAR ABSORPTION LINES

The SPURS spectra provide the first constraints on UV interstellar absorption lines and resolved Lyα damping wings in LRDs. These absorption features trace the interstellar medium (ISM) and the circumgalactic medium (CGM) gas surrounding the UV emitting regions in the LRDs. In Section 4.1, we describe our measurements of the UV absorption lines. We describe the Lyα damping wings and constraints on the absorbing gas column density in Section 4.2. We discuss the implications of fine-structure absorption line detections for the size of the absorbing region in Section 4.3, and explore constraints on aluminum abundances in Section 4.4.

4.1. *Absorption Line Measurements*

The rest-frame UV continua of all the four LRDs are clearly detected in the SPURS spectra (median S/N = 4 − 6 per resolution element for GN-2, GN-2004, GN-29 and S/N = 2 for CEERS-7902), enabling us to measure multiple absorption lines. We detect a suite of both low- (LIS; Si II λ1260, O I λ1302+Si II λ1304, C II λ1334, Si II λ1526, Fe II $\lambda\lambda$1608, 1611, Al II λ1670, Si II λ1808, Fe II λ2344, Fe II λ2383, Fe II λ2600, Mg II $\lambda\lambda$2796, 2803), intermediate- (Al III $\lambda\lambda$1854, 1862), and high-ionization (HIS; Si IV $\lambda\lambda$1393, 1402, C IV $\lambda\lambda$1548, 1550) interstellar absorption lines across the four LRDs, several of which are clearly seen in Figure 4 and Figure 10.

In Figure 12 we show zoom-ins of the strongest individual low and intermediate ionization absorption lines O I, Si II, Fe II, Al II, Al III and Mg II in each LRD, which we will discuss in more detail below. We also detect low-ionization fine-structure absorption at $> 3\sigma$ in two of our LRDs (Si II* λ1533 in GN-2, and C II* λ1335 in GN-2004), as well as several $2 - 3\sigma$ detections (Si II* λ1265, Si II* λ1817 in GN-2). In star-forming galaxies, fine-structure absorption lines are usually much weaker than resonant absorption lines (e.g., B. L. James et al. 2014; X. Xu et al. 2023b), and at high redshift are most commonly seen in emission (e.g., A. E. Shapley et al. 2003; T. Jones et al. 2012; K. A. Kornei et al. 2013). However, in the LRDs we find the fine-structure absorption lines are comparable in EW to the resonant lines, indicating a high column density in the excited states, which we discuss in detail in Section 4.3.

To quantify the strength and kinematics of the absorption lines, we fit each transition with a Gaussian profile on the continuum-normalized spectrum. For absorption lines below rest-frame 2000 Å, we use a linear continuum fit over the line-free pixels in a window (typically $150 - 200$ Å in the rest-frame) around each transition, masking nearby emission lines during the fit. For absorption lines in the NUV, we adopt the power-law continuum obtained in Section 3.5. To improve the recovery of the velocity profile given the low SNR of some of the absorption profiles, we fit transitions in similar ionization states simultaneously. Thus, in the FUV, we fit each of the LIS (O I, Si II, C II, Al II, Fe II), intermediate-ionization (Al III), and HIS (Si IV, C IV) lines in the FUV with a shared peak velocity offset from systemic and intrinsic line width (which we convolve with the NIRSpec LSF, assuming $R = 1300$, though we note our conclusions are unchanged if we assume the wavelength-dependent resolution), while the depth of each line is fitted independently. In the NUV, covered by G235M, we jointly fit Fe II and Mg II lines in the same way. We derive uncertainties by perturbing the spectrum by the error array and repeating the continuum and line fits 100 times. From these fits we constrain the absorption EW, peak velocity offset, and resolution-deconvolved peak covering fraction (discussed below), which we report in Table 6. For closely separated lines, we report a total

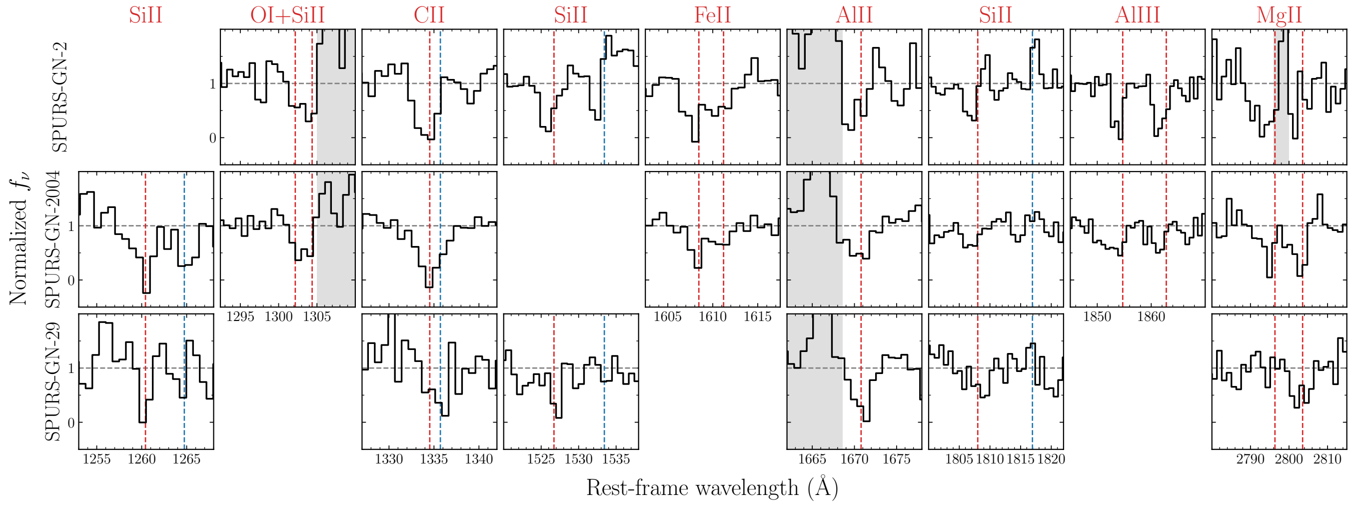

Figure 12. The strongest UV and NUV LIS absorption lines in the three LRDs with the highest continuum SNR. Red dashed lines show the line centers expected from systemic redshifts of detected LIS absorption lines. Blue vertical lines also show the wavelengths for the fine-structure lines.

EW. For non-detections, we report their 3σ EW upper limits obtained from the joint fit.

We first consider the strength of the absorption lines, which provide insights into the covering fraction and column density of gas around the UV emitting regions. In star-forming galaxies at $z \sim 7$, the highest oscillator strength LIS absorption lines measured in stacks, and individual spectra from SPURS, are typically weak (median EW ≈ -1 Å; e.g., K. S. Glazer et al. 2025; C. Keerthi Vasan G. et al. 2026). By contrast, we find the LIS absorption lines in the LRDs all have large EWs, with medians for each LRD ranging from -2.2 Å to -1.2 Å (computed based on measurements for single FUV lines at < 2000 Å only). These values are more typical of, or stronger than, those seen in lower redshift galaxies with weak Lyα emission, where strong LIS absorption lines are thought to indicate a high covering fraction of neutral gas ($z \simeq 1-3$; e.g., A. E. Shapley et al. 2003; C. C. Steidel et al. 2010; T. Jones et al. 2012; A. Saldana-Lopez et al. 2023). In contrast to other galaxies in the SPURS sample and at lower redshift, we also detect strong (< -1 Å) absorption in Si II λ1808 and Fe II λ1611 in three of the LRDs. These transitions have optical depths two orders of magnitude below most other Si II and Fe II transitions detected in our spectra, and are normally extremely weak in galaxies (e.g., T. Jones et al. 2018). The large EW implies very high column densities, which we will discuss below. Moreover it indicates that there is widespread saturation in all of the well-detected LIS absorption lines. We also detect strong Al III $\lambda\lambda$1854, 1862 absorption in the LRDs, most clearly seen in GN-2 and GN-2004 (Al III EW $= -2.2 \pm 0.3$, -2.1 ± 0.5 Å, respectively). These values exceed typical Al III strengths in star-forming galaxies (e.g., T. Jones et al. 2018), implying a high column density of Al in moderately ionized H II gas which we discuss more in Section 4.4. Finally, the HIS absorption lines have comparable EW to the LIS absorption lines (median EW $= -2.0$ Å), and are again at the high end of the range reported in star-forming galaxies at $z \sim 3-5$ (A. E. Shapley et al. 2003; A. J. Pahl et al. 2020).

The velocity peak of the lines provides insights into the bulk kinematics of the absorbing gas. In star-forming galaxies, both LIS and HIS absorption lines typically show comparable blueshifted velocities of ~ -100 to -200 km s^{-1}, indicating multi-phase outflows (e.g., A. E. Shapley et al. 2003; C. C. Steidel et al. 2010; J. Chisholm et al. 2015; X. Xu et al. 2022; G. C. Keerthi Vasan et al. 2023). In the LRDs, we detect blueshifted absorption in the HIS lines (Si IV) of GN-2, GN-2004, and CEERS-7902, peaking at $\Delta v = -231 \pm 32$, -204 ± 37, and -242 ± 92 km s^{-1}, respectively. Notably, the HIS absorption lines in GN-2 and GN-2004 show significantly higher peak velocities than the LIS absorption lines (-153 ± 23 km s^{-1} and -58 ± 30 km s^{-1}). We detect outflows in the LIS lines in GN-2 and CEERS-7902 (-153 ± 23 and -298 ± 74 km s^{-1}, respectively), while strikingly, both GN-2004 and GN-29 show significant LIS absorption close to systemic velocities, with $\Delta v \approx -53 \pm 30$ km s^{-1} and $+39 \pm 21$ km s^{-1} respectively, lower than typically seen in star-forming galaxies at lower redshifts (though three galaxies with similarly low LIS velocities have been reported in a sample from SPURS at $z \sim 5-9$; C. Keerthi Vasan G. et al. 2026). Interestingly, the HIS absorption lines in GN-29 are also consistent with peaking close to systemic velocities ($\Delta v \approx -52 \pm 54$ km s^{-1}), which is not typical for star-forming galaxies at high redshifts. Higher resolution spectroscopy will be required to more precisely determine the velocity profile of the absorbing gas, but these results indicate a diversity of outflow velocities in LRDs, which are not typical for star-forming galaxies.

The physical interpretation of the depth of the absorption lines depends on their optical depth: in optically thick gas this is a sensitive probe of the gas covering fraction, while it traces column density in optically thin gas (e.g., A. E. Shapley et al. 2003; T. A. Jones et al. 2013). We investigate whether the rest-frame UV absorption lines are saturated by comparing the relative EWs of transitions in the same ions (Si II, Si IV, C IV): in optically thin gas, these EWs should scale as $Nf\lambda^2$, where N is the ion column density, f is the oscillator strength, and λ is the rest-frame wavelength. For all four LRDs we find the EW ratios deviate strongly from the optically thin predictions in both the LIS and HIS lines, indicating saturation. Thus we interpret the residual intensity of the absorption lines as primarily tracing the covering fraction rather than column density of the absorbing gas, with the absorption depth providing a lower limit on the column density. Therefore, we also report the peak covering fraction ($C_f \approx 1 - I(v = v_{\rm peak})/I_0$, where I and I_0 are observed intensity and continuum intensity, respectively), corrected for instrumental resolution, in Table 6. In star-forming galaxies, typical LIS absorption line strengths decrease towards higher redshifts (A. J. Pahl et al. 2020; K. S. Glazer et al. 2025; C. Keerthi Vasan G. et al. 2026), which has been interpreted as an evolution towards lower neutral gas covering fraction based on data with moderate spectral resolution ($R \sim 5000$; e.g., T. A. Jones et al. 2013; N. Leethochawalit et al. 2016). To compare the covering fractions in the LRDs, we consider the lines with highest optical depth, which we expect to be strongly saturated, in regions free from emission lines (Si II $\lambda\lambda1260, 1526$, Si IV $\lambda1393$, Al II $\lambda1670$, Al III $\lambda1854$). We find very high covering fractions in both the LIS and HIS lines (median $C_f = 0.7 - 1.0$ for each LRD), implying the vast majority of the UV-emitting regions in these LRDs are surrounded by both low and high ionization gas. These covering fractions are at the high end of the $z \sim 5 - 9$ galaxy sample from SPURS (spanning $C_f \approx 0.2 - 0.9$; C. Keerthi Vasan G. et al. 2026). In particular, GN-2 and GN-29 show covering fractions of the UV continuum consistent with unity.

In summary, the interstellar absorption lines in the LRDs are not typical of star-forming galaxies at similar or lower redshifts. The lines reveal a diversity of kinematics, with two LRDs showing the bulk of low ionization gas at velocities close to systemic. They suggest a high column density and high covering fraction of dense neutral (H I) gas around the UV emitting region, which we quantify more below.

4.2. *Lyα Damping Wings and Column Density*

All four of the LRDs show significant downturns in their UV continuum around the wavelength of Lyα, including absorption troughs and suppression extending to $\gtrsim 1300$ Å in the rest frame. Such turnovers are expected due to Lyα damping wing absorption if neutral hydrogen with very large column densities covers the majority of the UV emitting regions. We note two-photon nebular continuum emission also produces downturns in the UV continuum around 1300 Å (D. Schaerer 2002; A. Raiter et al. 2010; A. J. Cameron et al. 2024). However, comparing the spectra to nebular continuum models we find two-photon continuum produces a more gradual turnover and no absorption trough, inconsistent with the observed spectra. Thus in the following we consider only the impact of the Lyα damping wing.

To estimate the H I column density, we fit the spectral region around Lyα in each source following the approach of C. A. Mason et al. (2026) (see also Z. Chen et al. 2026b; C. Keerthi Vasan G. et al. 2026). We first model the intrinsic continuum as a power law, fit to the observed spectrum over rest-frame $1350 - 1800$ Å, masking both IS absorption and nebular emission lines. We model Lyα attenuation local to the galaxy using a Voigt absorption profile with column density ($18 < \log(N_{\rm HI}/{\rm cm}^{-2}) < 24$) centered at the systemic redshift, assuming a covering fraction of unity, motivated by the large covering fractions inferred from the metal absorption lines, noting that our conclusions are unchanged if we also fit for the H I covering fraction. In GN-29, where we detect Lyα, we additionally model the emergent Lyα emission as a Gaussian, leaving its centroid, width, and EW as free parameters. As the Lyα emission is narrow, it must propagate without significant resonant scattering in the very high column density gas (implying either a patchy/clumpy absorbing medium or that the line is produced in an outer region, e.g., A. Torralba et al. 2026b; M. Tang et al. 2026b); thus we add the emission component on top of the damped Lyα (DLA) and continuum. We then apply the IGM damping wing attenuation (following J. Miralda-Escudé 1998; R. Barkana 2002; A. Mesinger & S. R. Furlanetto 2008), fitting for the distance from the source to the nearest neutral IGM region and assuming the IGM is fully neutral beyond this. We fit the spectra from the beginning of the spectral coverage for each LRD ($\approx 1210 - 1260$ Å) up to 1450 Å in the rest frame, deriving constraints

Table 6. Rest-frame UV interstellar absorption line EWs (Å), velocity offsets (km s^{-1}) and intrinsic covering fraction (C_f) of the four LRDs.

	SPURS-GN-2			SPURS-GN-2004			SPURS-GN-29			CEERS-7902		
Line	EW	Δv	C_f [a]	EW	Δv	C_f [a]	EW	Δv	C_f [a]	EW	Δv	C_f [a]
Si II λ1260	-1.1 ± 0.5	-153 ± 23	0.7 ± 0.3	-1.7 ± 0.4	-58 ± 30	1.0 ± 0.1	-1.2 ± 0.3	$+39 \pm 21$	1.0 ± 0.2	> -1.6	–	–
Si II* λ1265	> -1.5	–	–	-1.6 ± 0.6	-58 ± 30	0.9 ± 0.2	> -1.1	–	–	> -3.3	–	–
O I+Si II $\lambda\lambda$1302, 1304	-1.8 ± 0.4	-153 ± 23	0.7 ± 0.1	-1.7 ± 0.5	-58 ± 30	0.5 ± 0.1	-1.2 ± 0.5	$+39 \pm 21$	0.7 ± 0.2	-3.5 ± 1.4	-298 ± 74	0.8 ± 0.1
C II+C II* $\lambda\lambda$1334, 1335	-2.9 ± 0.6	-153 ± 23	0.9 ± 0.1	-3.2 ± 0.5	-58 ± 30	0.9 ± 0.1	-1.9 ± 0.7	$+39 \pm 21$	0.8 ± 0.2	> -2.2	–	–
Si IV λ1393	-2.3 ± 0.3	-231 ± 32	1.0 ± 0.0	-2.0 ± 0.2	-204 ± 37	0.8 ± 0.1	-1.4 ± 0.4	-52 ± 54	0.9 ± 0.2	-2.2 ± 0.6	-242 ± 92	0.8 ± 0.2
Si IV λ1402	-2.0 ± 0.2	-231 ± 32	0.9 ± 0.1	-1.5 ± 0.3	-204 ± 37	0.6 ± 0.1	-1.5 ± 0.4	-52 ± 54	0.9 ± 0.2	> -2.5	–	–
Si II λ1526	-1.9 ± 0.2	-153 ± 23	1.0 ± 0.1	–[d]	–	–	-1.4 ± 0.2	$+39 \pm 21$	1.0 ± 0.1	-1.9 ± 0.7	-298 ± 74	0.7 ± 0.3
Si II* λ1533	-1.5 ± 0.3	-153 ± 23	0.8 ± 0.2	–[d]	–	–	> -1.0	–	–	> -1.0	–	–
C IV λ1548	–[b]	–	–	–[d]	–	–	> -1.2	–	–	–[b]	–	–
C IV λ1550	–[b]	–	–	–[d]	–	–	> -0.3	–	–	–[b]	–	–
Fe II λ1608	-2.0 ± 0.3	-153 ± 23	1.0 ± 0.1	-1.5 ± 0.3	-58 ± 30	0.7 ± 0.1	-0.8 ± 0.4	$+39 \pm 21$	0.6 ± 0.2	-2.4 ± 0.7	-298 ± 74	0.8 ± 0.3
Fe II λ1611	-1.5 ± 0.3	-153 ± 23	0.7 ± 0.2	-0.9 ± 0.3	-58 ± 30	0.4 ± 0.1	> -1.1	–	–	> -0.7	–	–
Al II λ1670	-2.1 ± 0.3	-153 ± 23	1.0 ± 0.1	-1.7 ± 0.3	-58 ± 30	0.7 ± 0.1	-1.5 ± 0.3	$+39 \pm 21$	1.0 ± 0.0	> -3.2	–	–
Si II λ1808	-1.9 ± 0.4	-153 ± 23	0.8 ± 0.2	-1.0 ± 0.3	-58 ± 30	0.4 ± 0.1	-1.2 ± 0.3	$+39 \pm 21$	0.7 ± 0.2	> -2.5	–	–
Si II* λ1817	> -0.9	–	–	-0.5 ± 0.2[c]	-385 ± 41	1.0 ± 0.0	> -1.0	–	–	-1.7 ± 0.7	-298 ± 74	0.5 ± 0.2
Al III λ1854	-2.2 ± 0.3	-167 ± 22	1.0 ± 0.1	-2.1 ± 0.5	-275 ± 57	0.6 ± 0.1	-1.8 ± 0.7	$+62 \pm 62$	0.8 ± 0.2	-2.1 ± 0.9	-303 ± 59	0.8 ± 0.2
Al III λ1862	-2.2 ± 0.4	-167 ± 22	1.0 ± 0.0	-1.4 ± 0.4	-275 ± 57	0.4 ± 0.1	> -0.7	–	–	-2.6 ± 0.8	-303 ± 59	1.0 ± 0.2
Fe II λ2344	-2.1 ± 0.4	-147 ± 30	1.0 ± 0.0	-2.9 ± 0.5	$+0 \pm 40$	1.0 ± 0.1	-1.6 ± 0.6	$+53 \pm 64$	1.0 ± 0.3	-5.3 ± 1.3	-111 ± 98	0.7 ± 0.2
Fe II λ2383	> -2.5	–	–	-2.1 ± 0.5	$+0 \pm 40$	0.7 ± 0.2	> -1.8	–	–	-4.4 ± 1.6	-111 ± 98	0.6 ± 0.2
Fe II λ2600	-2.3 ± 0.5	-147 ± 30	1.0 ± 0.1	-2.1 ± 0.8	$+0 \pm 40$	0.6 ± 0.2	-1.7 ± 0.7	$+53 \pm 64$	1.0 ± 0.2	-8.0 ± 2.3	-111 ± 98	0.9 ± 0.1
Mg II λ2796	-5.3 ± 1.5	-316 ± 118	1.0 ± 0.1	-2.8 ± 0.6	-138 ± 38	0.8 ± 0.2	> -0.9	–	–	-2.9 ± 0.8	-434 ± 55	1.0 ± 0.1
Mg II λ2803	-4.2 ± 1.4	-316 ± 118	0.8 ± 0.3	-3.4 ± 0.6	-138 ± 38	1.0 ± 0.1	-3.3 ± 1.0	-57 ± 124	0.7 ± 0.2	-2.8 ± 0.8	-434 ± 55	1.0 ± 0.2

NOTE—EW, Δv and C_f are reported for lines detected at $> 2\sigma$; otherwise the 3σ upper limit on the EW is given (negative EW denotes absorption).
a: The covering fractions reported are resolution-deconvolved peak covering fractions.
b: C IV absorption in SPURS-GN-2 and CEERS-7902 is measured separately given its complicated profile.
c: Si II* λ1817 in SPURS-GN-2004 is fitted separately from the other low-ionization lines because an apparent P-Cygni emission component shifts its velocity centre.
d: These lines are not covered, falling in the detector gap.

and uncertainties on the H I column density using the Markov chain Monte Carlo ensemble sampler `emcee` (D. Foreman-Mackey et al. 2013).

Figure 13 shows the best-fit model to the Lyα absorption profile, as well as the intrinsic continuum model, for each LRD. In all cases, we find very large column densities ($N_{\rm HI} \approx 10^{22.0-22.7}$ cm^{-2}) are required to reproduce the observed profiles, dominating over the IGM damping wing. The high column densities in our LRD sample are significantly larger (by $> 10\times$) than what is typically inferred in $z \gtrsim 5$ galaxies from both low-resolution NIRSpec prism spectra and medium-resolution grating spectra (H. Umeda et al. 2026; K. E. Heintz et al. 2025; C. A. Mason et al. 2026; Z. Chen et al. 2026b; C. Keerthi Vasan G. et al. 2026).

These high H I column densities are also consistent with the detections of absorption in low oscillator strength transitions: Si II λ1808 ($f = 0.0022$) in GN-2, GN-2004 and GN-29 and Fe II λ1611 ($f = 0.0014$) in GN-2 and GN-2004. A precise estimate of the column density is challenging given that the Si II and Fe II lines are likely all saturated, and there is uncertainty due to the intrinsic linewidth and dust depletion. However, we can estimate a conservative lower limit on the Si II and Fe II column densities assuming the 1808 Å and 1611 Å transitions are optically thin and no dust depletion of either element. In this case, we estimate $N > 1.13 \times 10^{20}\, W_\lambda / f \lambda^2\, {\rm cm}^{-2}$, resulting in $N_{\rm SiII} > 10^{16}\,{\rm cm}^{-2}$ and $N_{\rm FeII} > 10^{16}\,{\rm cm}^{-2}$ for all LRDs where these lines are detected. Assuming solar abundance ratios and the gas-phase metallicity implied by the emission lines ($Z \approx 0.03 - 0.28 Z_\odot$), this also implies very high HI column densities $N_{\rm HI} > 10^{21.3-22.5}\,{\rm cm}^{-2}$.

4.3. *Fine-structure absorption*

In addition to the ground-state interstellar absorption lines, in GN-2 and GN-2004 we detect absorption lines from several fine-structure states, with comparable strength to the resonant absorption lines. Fine-structure absorption requires a population in an excited level of the ion's ground term, which can only compete against rapid spontaneous decay if the gas is collisionally excited or radiatively pumped by an intense local UV field (J. N. Bahcall & R. A. Wolf 1968; J. X. Prochaska et al. 2006; B. L. James et al. 2014). In star-forming galaxies these transitions are typically weak or seen only in emission, and are thought to trace diffuse ($n_e \sim 10$ cm^{-3}) gas over kiloparsec scales (T. Jones et al. 2012; X. Xu et al. 2023b). Strong fine-structure absorption is however often seen in gamma ray burst (GRB) afterglows, where the levels are thought to be excited by the strong radiation field of the GRB within $\lesssim 100$ pc (J. X. Prochaska

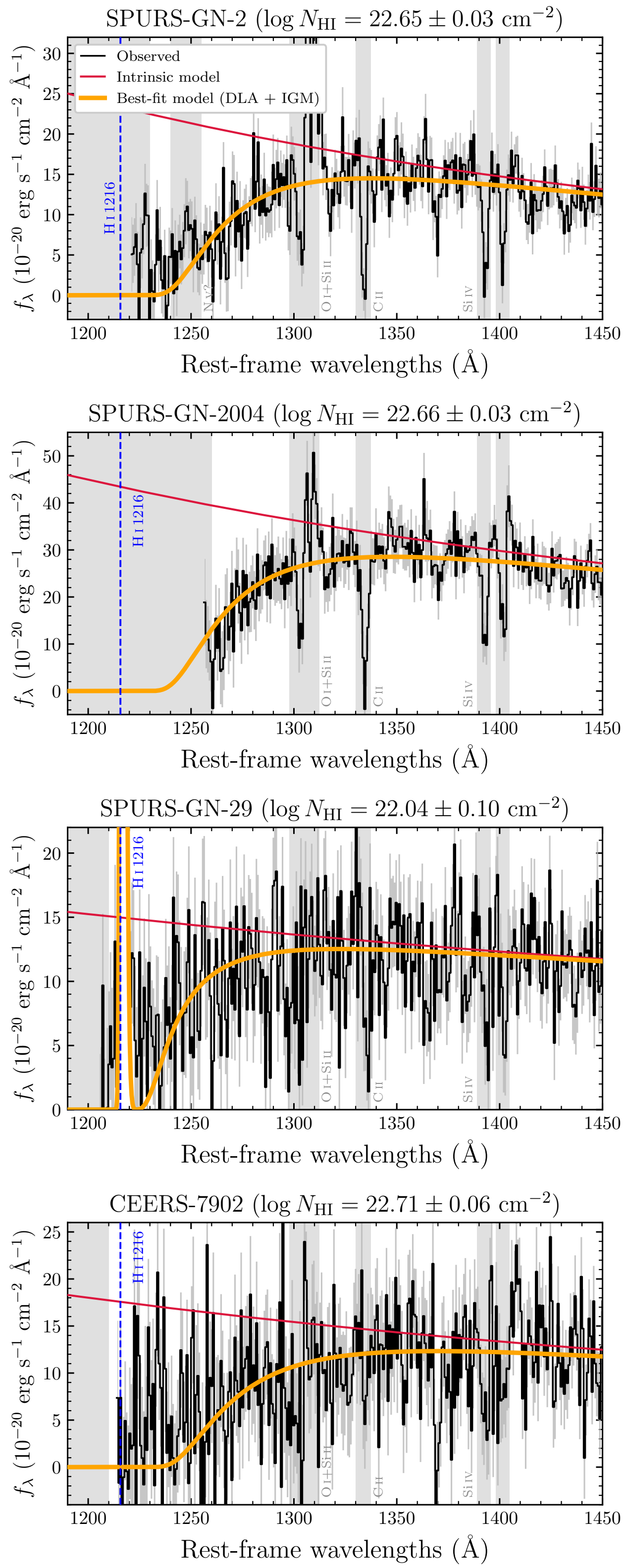

Figure 13. Fit to the Lyα profile. The black line shows the observed spectrum with the error spectrum shown in gray. We show the best-fit absorption line model in orange and the intrinsic power-law continuum model in red. The low-ionization absorption lines are masked in gray and excluded from the fit.

et al. 2006). While some of these lines (Figure 12) also show likely P-Cygni emission components, the detection of strong fine-structure absorption in these LRDs suggests densities and/or radiation fields that are not typical of low redshift star-forming galaxies.

To investigate the conditions that produce these lines, we first estimate the excited-state population fraction implied by these detections. We focus on Si II and Fe II transitions, for which we detect multiple absorption lines, and are sensitive tracers of gas conditions (J. X. Prochaska et al. 2006). As the detected lines in both ground-state and excited state transitions are saturated in our spectra, we consider an order of magnitude approach, leaving more detailed analysis to future work. From the fine-structure EWs, we estimate conservative lower limits on the excited state column densities, assuming the lines are optically thin, using the lowest oscillator strength lines which are robustly detected and free from blending with ground-state lines. The best line for this purpose is Si II $\lambda1817$ ($f = 0.0016$) in GN-2004 (EW $= -0.5 \pm 0.2$ Å), from which we estimate $N_{\rm SiII^*} \gtrsim 1.6 \times 10^{16}$ cm^{-2}. As the ground-state transitions in Si II all appear saturated we estimate the expected ground-state column density assuming the damped Lyα and metal resonant and fine-structure absorption all arise in the same gas. The H I column density from the damping wing fit implies ground-state columns $N_{\rm SiII} \approx 3 \times 10^{17}$ cm^{-2}, assuming $Z = 0.2\,Z_\odot$ and solar abundance ratios. This implies $n_{\rm excited}/n_{\rm ground} \gtrsim 0.04$ for Si II, which is four times higher than the mean Si II* level population inferred in the CLASSY sample at $z \sim 0$ (X. Xu et al. 2023a). We note this is likely to be underestimated given saturation, suggesting potentially significant excitation of the fine-structure states relative to what is seen at low redshifts.

We consider excitation by both radiative pumping and collisional excitation, though a combination of both effects may contribute. To assess radiative pumping, we compute the strength of the local UV radiation field at a distance r from the UV-emitting source: $G = \lambda L_\lambda/(4\pi r^2)$, expressed relative to the mean Galactic interstellar field, G_0 (H. J. Habing 1968), following J. X. Prochaska et al. (2006) and X. Xu et al. (2023b). Based on the excitation calculations of J. X. Prochaska et al. (2006), producing $n_{\rm excited}/n_{\rm ground} > 0.04$ for Si II requires $G_0 > 10^4$. Using the rest-frame UV luminosities of GN-2004, we find this is achieved provided the absorbing gas is within just < 300 pc of the UV-emitting source. Reproducing the same excited fraction through collisional excitation requires $n_e > 30$ cm^{-3}. Assuming $N_{\rm HI} \approx 10^{22.6}$ cm^{-2}, this also implies the gas must be compact ($\lesssim 400$ pc). Thus, both excitation channels imply the absorbing gas must be compact, confined to < 400 pc from the UV-emitting source, to produce the strong fine-structure absorption. Such a compact region is comparable to the unresolved UV continuum ($\lesssim 80$ pc).

4.4. *Aluminum Abundances in LRDs*

Given the nitrogen enhancement in all four LRDs reported above (Section 3.3), we might expect other anomalous abundance signatures associated with enrichment in dense nuclear clusters. In particular, R. Marques-Chaves et al. (2024) suggested aluminum enhancement is a promising additional test (see also J. Chisholm et al. 2026). Aluminum enhancements are expected from the MgAl chain in very hot hydrogen burning, and large aluminum abundance ratios can be a signature of nucleosynthesis under conditions likely only achieved in the most massive stars (VMS or SMS) and in massive AGBs undergoing hot bottom burning (N. Prantzos et al. 2007; N. Bastian & C. Lardo 2018; E. R. Higgins et al. 2023, 2025). Indeed, M. W. Topping et al. (2024) recently reported a tentative Al III $\lambda1854$ emission feature in a N IV]-emitting galaxy at $z = 7.04$, implying $> 30\times$ solar Al-enhancement if confirmed. While we do not detect aluminum emission features in our LRD sample, we do detect markedly strong Al II $\lambda1670$ and Al III $\lambda\lambda1854, 1862$ absorption (Section 4.1), motivating an exploration of potential aluminum enhancement from the absorption lines.

As discussed in Section 4.1, we find all the well-detected absorption lines are affected by saturation, making robust estimates of column densities and abundance patterns very uncertain. We caution that apparent optical depth methods provide lower limits on column density in such cases, and the correction factors can be large (e.g., B. D. Savage & K. R. Sembach 1991; M. Pettini et al. 2002; A. M. Quider et al. 2009). To assess a potential aluminum enhancement in the LRDs, we consider the relative strength of Al II $\lambda1670$ to Si II $\lambda1526$ absorption EW in the LRDs and the rest of the SPURS sample. These specific transitions are chosen to mitigate uncertainties arising from multiple sources. We assess Al/Si rather than Al/Mg because Al II and Si II are both accessible in the high SNR G140M spectra for a large fraction of the SPURS sample, and trace the same odd-even nucleosynthetic signature. The ratio of Al II $\lambda1670$ to Si II $\lambda1526$ is chosen because, for a solar gas-phase abundance pattern, the line strengths are expected to be similar and with low variation. Specifically, EW(Al II $\lambda1670$)/EW(Si II $\lambda1526$) ≈ 1.47 in the optically thin limit, decreasing toward

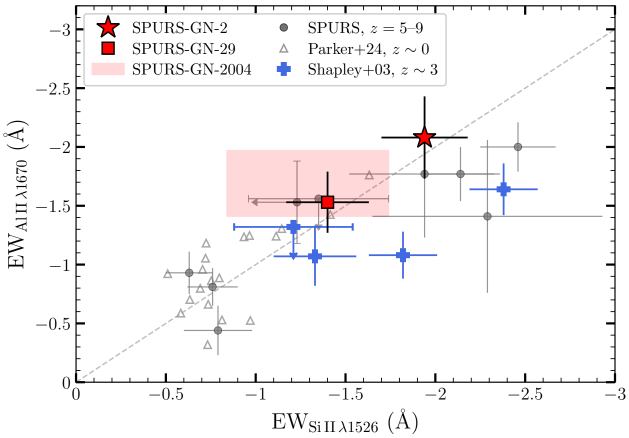

Figure 14. Al II λ1670 absorption line EWs vs. Si II λ1526 absorption line EWs of the three LRDs with absorption line detections (GN-2, GN-2004, GN-29). For GN-2004, which lacks Si II λ1526 coverage, we plot the expected range spanning from the Si II λ1304 EW to the Si II λ1260 EW as a red shaded region. For comparison, we overplot EWs of Lyman break galaxies at $z \sim 3$ (blue crosses; A. E. Shapley et al. 2003), nearby star-forming galaxies from CLASSY (open triangles; K. S. Parker et al. 2024), and SPURS galaxies at $z \simeq 5-9$ (grey circles; Z. Chen et al. 2026b; C. Keerthi Vasan G. et al. 2026).

1.09 as the lines saturate (based on oscillator strengths from D. C. Morton 1991). Dust depletion, which preferentially removes aluminum from the gas phase relative to silicon (e.g., E. B. Jenkins 2009; C. Konstantopoulou et al. 2022), can weaken Al II relative to Si II. On the other hand, an increased ratio of EW(Al II λ1670)/EW(Si II λ1526) may suggest super-solar Al/Si ratio. We also caution that ionization effects can lead to increased EW(Al II λ1670)/EW(Si II λ1526), as the abundance ratio of Al^+/Si^+ can increase by potentially $\gtrsim 0.5$ dex (J. C. Howk & K. R. Sembach 1999; G. Vladilo et al. 2001) in cases where there is significant contribution from ionized gas (i.e., a phase bearing H^+, Al^+, and Si^+). Given the high EW Al III absorption we detect in the SPURS LRDs, the ionization effects may be significant. Thus it is important to consider line saturation, dust depletion, and ionization effects alongside the abundance patterns.

In Figure 14 we plot the Al II λ1670 and Si II λ1526 EW for the LRDs in this paper, along with the rest of the SPURS sample (which will be presented fully in upcoming work). As we lack coverage of Si II λ1526 in GN-2004, we instead use the EW of Si II $\lambda1260, \lambda1304$ as upper and lower limits on the EW respectively (as $\tau_{1302} < \tau_{1526} \ll \tau_{1260}$). We also show measurements from lower redshifts for comparison, from A. E. Shapley et al. (2003) ($z \sim 3$) and CLASSY ($z \sim 0$; K. S. Parker et al. 2024). The SPURS sample generally lies along the one-to-one line, with the LRDs lying towards the upper end of both Al II λ1670 and Si II λ1526 EW, consistent with the high covering fraction and column densities discussed in Section 4. Notably the Al II/Si II EW ratio in the SPURS sample is higher than in the A. E. Shapley et al. (2003) stacks, indicating physical differences in the absorbing gas. The lower Al II/Si II EW ratio < 1 in $z \sim 3$ stacks implies that at least some of the absorption is unsaturated *and* has a sub-solar Al^+/Si^+ abundance in the gas phase. We reiterate that a sub-solar gas-phase Al/Si is consistent with dust depletion effects (or, of course, intrinsically sub-solar Al/Si ratio).

A natural explanation for the higher Al II/Si II EW ratios in the SPURS sample compared to $z \sim 3$ stacks is that lines are fully saturated due to high low-ion column densities (as described in Section 4.1). In general the line ratios suggest that Si II λ1526 is essentially fully saturated, and consequently the ratios shown in Figure 14 imply that Al II λ1670 is likewise saturated. In this case, we cannot robustly recover the Al/Si abundance from this line ratio. We find GN-2004 may be consistent with an offset toward higher Al II λ1670 than the rest of the sample, suggestive of an enhanced Al/Si abundance in this source. However, without a direct measurement of the Si II λ1526 EW, this interpretation remains tentative: a spectrum with coverage of this line will be required to make a more definitive statement.

We now consider the challenges and future prospects for more reliable abundance patterns of Al and other elements based on interstellar absorption in LRDs. First, it is essential to measure unsaturated absorption lines, and to account for hidden saturation effects. Next, dust depletion effects can be assessed by comparing elements of common nucleosynthetic origin with different depletion rates. Alternatively the effects can be mitigated by comparing elements with very low (such as O and S) or similar depletions (such as Si and Mg; e.g., C. Konstantopoulou et al. 2022). Finally, ionization effects can be either modeled based on measurements from multiple ionization states, mitigated by comparing ions with similar ionization corrections, or perhaps most simply by analyzing systems where weak intermediate-ion absorption such as Al III indicates that corrections to the low ion abundances are minimal (e.g., J. C. Howk & K. R. Sembach 1999). Our SPURS sample analysis suggests that precise Al abundances may be difficult to constrain in LRDs due to the large optical depth of Al II λ1670 (and lack of suitable weaker transitions), and potentially significant ionization corrections indicated by the strong Al III absorption. However, lower limits of Al relative to other elements can be obtained if suitably weak lines can be identified. Relatively weak lines may also provide interesting constraints on other chemical abundance patterns once saturation effects are accounted for (e.g., A. M. Quider et al. 2009). We observe potentially not fully saturated absorption from such weak lines as Si II $\lambda1808$ and Fe II $\lambda1611$, which are sensitive to α/Fe ratio for example. Additional low-oscillator strength transitions from species such as S II, Ni II, and Zn II may prove interesting for further analysis.

5. REST-FRAME UV LINE DIAGNOSTICS IN THE BROADER LRD POPULATION

We have investigated the UV spectroscopic properties of a sample of four LRDs. In this section, we place these results in context using spectra from the public archive. In Section 5.1, we quantify how common N IV] and N III] emission is in LRDs, and in Section 5.2 we characterize the range of C III] EWs in LRDs. In both subsections, we compare these measurements to those of star-forming galaxies at the same redshifts, with the goal of establishing whether the narrow-line properties of LRDs are typical of the broader galaxy population.

5.1. *Nitrogen Enhanced Gas in LRDs*

Each of the four LRDs considered in this paper has N IV] or N III] detections that suggest nitrogen-enriched (high N/O or N/C) abundance patterns (Section 3.3). The apparent ubiquity of the UV nitrogen emission in the LRDs is striking compared to the rarity of such detections in the broader galaxy population (e.g., M. W. Topping et al. 2025b). If nitrogen-enhanced abundance patterns are more common in LRDs, it would not only hold clues as to the physics of the narrow-line gas in LRDs, but it would also add to our understanding of the physics that drives the nitrogen enhancements. Of course, with a sample of just four LRDs, definitive conclusions are not possible. In this section, we consider the archive to characterize how commonly N IV] or N III]-emitting LRDs appear in the full LRD population at $z > 4$. We will then compare against similar literature on the incidence of nitrogen emission in the full galaxy population at $z > 4$.

To achieve this goal, we construct a large sample of LRDs at $z > 4$ with publicly available NIRSpec spectra and constrain the strengths of N IV] and N III] emission lines. To maximize the sample size, we take advantage of LRDs with either grating spectra or prism spectra covering the rest-frame UV wavelengths. For LRDs with NIRSpec grating spectra, we identify 20 objects which have been presented in the literature (Y. Harikane et al. 2023; R. Maiolino et al. 2024a; D. D. Kocevski et al. 2025; M. Tang et al. 2025; I. Juodžbalis et al. 2026b; C. Papovich et al. 2026). We also utilize the DIVER (GO 8018, PI: X. Lin) dataset whose G140M spectra are publicly available. The DIVER survey adds 5 LRDs to our database (which will be presented by the DIVER team in S. Cai et al. in prep). Hα emission lines of these 5 LRDs have been characterized with NIRCam grism spectra (J. Matthee et al. 2024; J. Zhang et al. 2026), and we measure rest-frame UV emission lines using the new G140M spectra. The DIVER G140M spectrum in 1 of 5 LRDs has been reported in S. Mascia et al. (2026). We then add 12 LRDs with SPURS grating spectra, including Abell2744-QSO1 (M. Tang et al. 2026b). We report 11 LRDs with new rest-frame UV spectroscopic constraints identified from SPURS and DIVER programs in Table 7. For LRDs with prism spectra, we utilize the sample described in A. de Graaff et al. (2025b). This adds 85 more LRDs at $z > 4$, after cross-matching LRDs with grating observations and removing repeat sources. Overall these yield a sample of 122 LRDs at $z > 4$ with rest-frame UV spectroscopic coverage, including 37 with grating observations and 85 with only prism observations.

The 122 LRDs span a redshift range from $4.05 - 9.29$. We use the NIRSpec spectra of these 122 LRDs reduced in a self-consistent way. For the 110 LRDs that are not in the SPURS sample, we utilize their spectra reduced by the DAWN JWST Archive (DJA; K. E. Heintz et al. 2024; A. de Graaff et al. 2025c) with `msaexp`. We reduce the SPURS spectra of the remaining 12 LRDs with `msaexp` following the same procedures as DJA (see Section 2.2). To derive the absolute UV magnitudes, we also collect the NIRCam photometry of these 122 LRDs from DJA (F. Valentino et al. 2025). The M_{UV} of these 122 LRDs are shown in Figure 15, with a median value of -18.4 and the $16-84$th percentiles of -19.4 to -17.3.

We characterize the N IV] and N III] emission lines in these 122 LRDs by visually inspecting their 2D spectra. Details of the nitrogen emitters are listed in Table 7. We identify 7 LRDs showing N IV] emission with doublet S/N > 5, and an additional LRD with N IV] with S/N $= 3$ (GN-29, see Section 3.3). We detect N III] $\lambda1746 - 1754$ emission with integrated S/N > 5 in 9 LRDs. There are 5 LRDs with spectra that detect both N IV] and N III]. These form a sample of 12 LRDs with detections of either N IV] or N III]. Four of these twelve LRDs are presented in this paper, and the UV nitrogen line detections of another five LRDs have been reported previously in literature (UNCOVER-45924, I. Labbé et al. 2024; CANUCS-LRD-z8.6, R. Tripodi et al. 2025a; T. Morishita et al. 2026; C3PO-45290, C3PO-46403, C. Papovich et al. 2026; GN-16813, S. Mascia et al. 2026). The N IV] or N III] emission lines of the remaining three LRDs are

Table 7. LRDs at $z > 4$ with new rest-frame UV spectroscopic constraints obtained from SPURS and DIVER programs

Program	ID	RA (deg)	Dec (deg)	$z_{\rm spec}$	$M_{\rm UV}$	N IV] EW (Å)	N III] (Å)	C III] EW (Å)
SPURS	A2744-52	3.602778	−30.419355	4.725	−18.1	–	< 3.7	16 ± 1
SPURS	A2744-1069	3.583813	−30.374517	5.145	−19.4	–	2.4 ± 0.6	11 ± 1
SPURS	EGS-39	214.985672	+52.956233	5.200	−19.4	–	< 3.7	18 ± 2
SPURS	EGS-43	215.066442	+52.941884	6.271	−19.6	< 7.9	10 ± 2	< 10
SPURS	EGS-45	214.990972	+52.916527	5.682	−18.7	6.0 ± 1.0	< 4.6	24 ± 3
SPURS	EGS-187	215.020802	+52.917789	6.380	−18.7	< 4.3	< 6.7	< 5.2
SPURS	GN-500	189.094351	+62.198975	4.880	−18.2	–	< 4.5	19 ± 3
DIVER	1008671	189.159025	+62.260221	4.416	−18.6	< 4.2	< 4.4	< 3.0
DIVER	1020621	189.125779	+62.287404	4.681	−18.7	< 23	< 21	< 16
DIVER	1033320	189.159764	+62.295924	4.486	−18.6	< 7.4	< 8.6	< 5.0
DIVER	1034620	189.179302	+62.292533	5.191	−20.2	< 7.6	< 15	< 15

Note—N IV], N III], and C III] EWs are the integrated EWs of N IV] doublet, N III] quintuplet, and C III] doublet, respectively. For non-detections, 5σ upper limits of EWs are provided. For the 4 LRDs in DIVER observations (S. Cai et al. in prep), Hα emission lines have been characterized with grism spectra (J. Matthee et al. 2024; J. Zhang et al. 2026), and here we list the rest-frame UV emission lines measured from the new G140M spectra.

newly-identified from SPURS program (SPURS-A2744-1069, SPURS-EGS-43, SPURS-EGS-45; Table 7), and we show their N IV] or N III] spectra in Figure D.3 in appendix. We will present the new N IV] and N III] detections in more detail in a future paper. The N IV] or N III] EWs of these 12 LRDs are measured following the same methodology described in Section 2.2.

The vast majority (110) of the LRDs do not show N IV] and N III] detections in their NIRSpec spectra. However, given the widely varying continuum strengths and sensitivity limits among different programs, the EW limits of non-detections span a wide range. For LRDs with grating spectra, we estimate the flux limits of each component of N IV] doublet and N III] quintuplet by integrating the error spectrum over two resolution elements (600 km s^{-1} for $R \simeq 1000$; 222 km s^{-1} for $R \simeq 2700$) in quadrature. For LRDs with low-resolution ($R \sim 100$) prism spectrum only, we estimate the total flux limit of N IV] and N III] by integrating the error spectrum over two resolution elements (6000 km s^{-1}) in quadrature as it is impossible to resolve the individual components. We measure the underlying continuum from the spectrum and compute the EW limit. For the N IV] doublets of these 110 LRDs, we derive $16 - 50 - 84$th percentiles of 5σ limiting EWs of 9 Å, 48 Å, and 115 Å, respectively. The $16 - 50 - 84$th percentiles of 5σ limiting N III] EWs are 13, 71, and 173 Å. This demonstrates that many of the LRDs do not have deep enough spectra to place a useful limit on the N IV] or N III] EW.

To put robust constraints on the fraction of LRDs presenting UV nitrogen emission lines, we focus on the subset with 5σ EW limit reaching 5 Å for the N IV] doublet or the N III] quintuplet. This yields a sample of 18 LRDs out of the total 122. These 18 LRDs are brighter in the UV continuum than the full LRD population, with $16 - 50 - 84$th percentiles of $M_{\rm UV}$ of −20.4, −19.4, −18.2, respectively. The 18 LRDs include all the 12 objects with N IV] or N III] detections described above. Ten of these twelve LRDs present N IV] or N III] emission with EWs > 5 Å. This results in a fraction of 56^{+14}_{-14}% LRDs presenting relatively strong N IV] or N III] emission lines. This suggests that UV nitrogen emission which links to nitrogen enhanced gas is likely very common among the LRD population.

We compare the incidence of UV nitrogen emission in LRDs against that of the full galaxy population at $z > 4$. Recent studies have reported that the N IV] and N III] emission lines are generally weak in a large population of star-forming galaxies. Y. Isobe et al. (2025) have created a composite prism spectrum of 665 non-AGN galaxies at $z = 4 - 7$ and did not detect N IV] or N III] emission lines. R. Singh Rai & G. Roberts-Borsani (2026) have stacked grating spectra of 135 galaxies at $z = 6 - 10$, revealing very weak average N IV] (EW = 1.1 Å) and N III] emission (EW = 0.4 Å). Strong UV nitrogen emission is also rare among the galaxy population. Using a sample of 747 galaxies at $z > 4$ constructed from publicly available NIRSpec observations, M. W. Topping et al. (2025b) have shown that only 7% of galaxies with suffi-

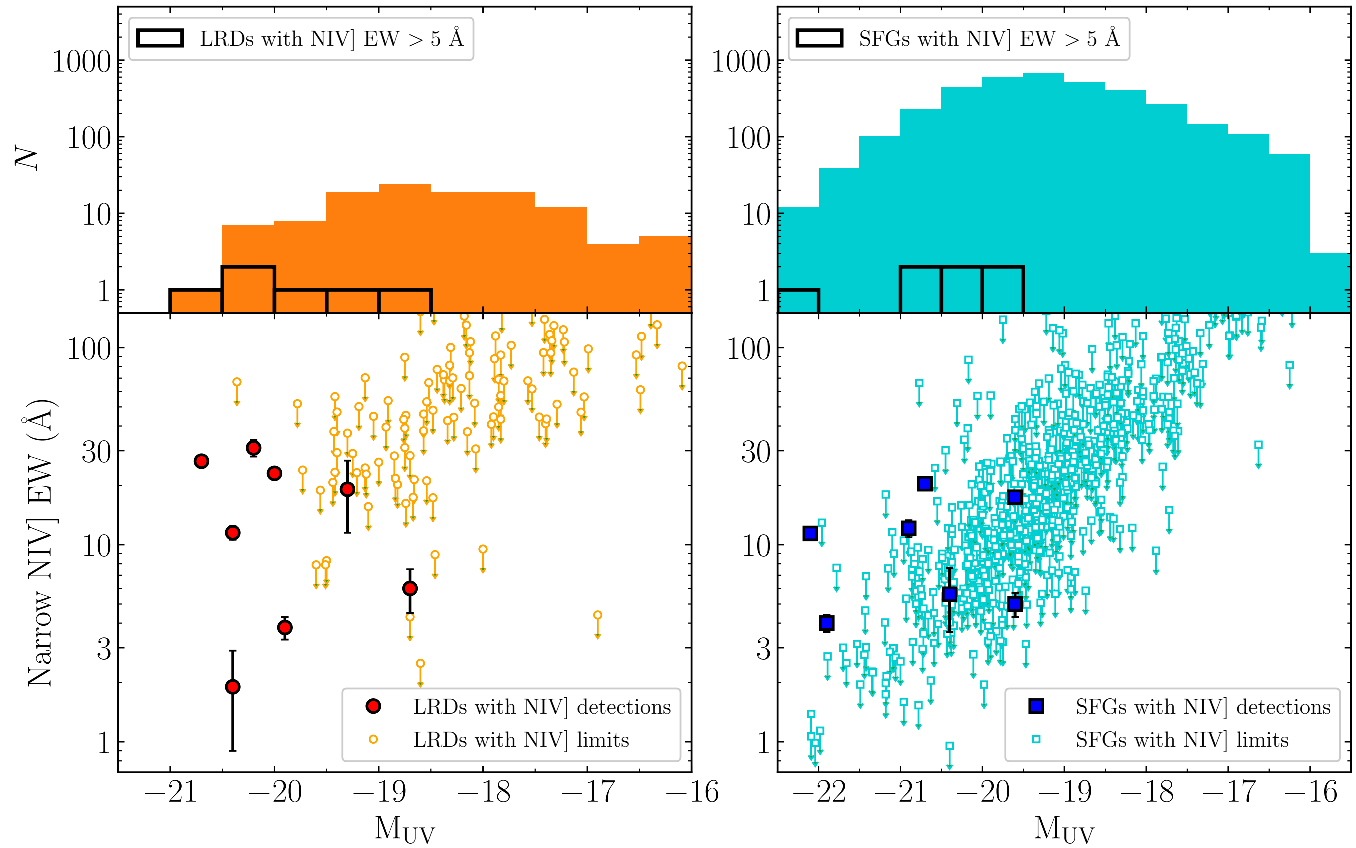

Figure 15. N IV] EW versus M_{UV} of LRDs (left panel) and full galaxy population (right panel) at $z > 4$. LRDs with N IV] detections are shown as red circles, and star-forming galaxies (SFGs) are shown as blue squares (M. Castellano et al. 2024; R. Maiolino et al. 2024b; D. Schaerer et al. 2024; M. W. Topping et al. 2024, 2025b; Z. Chen et al. 2026a). The 5σ upper limits of non-detections are shown as orange open circles for LRDs (cyan open squares for galaxies). On the top of each panel, we provide the M_{UV} distributions, highlighting those with N IV] EW > 5 Å with black colors.

ciently deep spectra exhibit N IV] with EW > 5 Å. We compare the N IV] emitter fraction in LRDs with that in M. W. Topping et al. (2025b). To make a fair comparison, we select LRDs following the same criteria in M. W. Topping et al. (2025b): identifying objects with deep enough spectra with 5σ limiting N IV] EW reaching 5 Å. This leaves 11 LRDs from our sample of 122 LRDs. We find 6 of these 11 LRDs presenting N IV] emission with EW > 5 Å, indicating a N IV] emitter fraction of 55^{+18}_{-19}%. Though the sample size is small, the N IV] emitter fraction of LRDs is 8 times that of the galaxy population (7%; Figure 15).

Overall, the analysis of the full archive suggests that N IV] and N III] are fairly common in LRDs. We find that 12 of 18 LRDs with deep spectra show either N IV] and N III], including 10 with EW > 10 Å, implying a nitrogen emitter fraction of 56^{+14}_{-14}%. Considering just the subset with deep N IV] constraints, this fraction is similar (55^{+18}_{-19}%). While larger grating datasets will be required to reduce the statistical uncertainties, the current samples already suggest that LRDs are more likely to have nitrogen line detections than the full galaxy population. While the physics responsible for nitrogen enhancements has been discussed extensively in the literature (e.g., C. Charbonnel et al. 2023; C. Kobayashi & A. Ferrara 2024; D. Schaerer et al. 2024; P. Senchyna et al. 2024; M. W. Topping et al. 2025b; W. McClymont et al. 2026), there has not been as much focus on why LRDs also show similar abundance patterns. We will return to the topic of nitrogen in LRDs in Section 6.

5.2. *C III] EW Distribution in LRDs*

The C III] EW provides a diagnostic of the physical conditions of the narrow-line gas. We have shown that the four LRDs presented in this paper have very large narrow C III] EWs, ranging from 18 Å to 26 Å (Section 3.2). We have reported that these values are well above what is seen in typical star-forming galaxies at similar redshifts (e.g., G. Roberts-Borsani et al. 2024; R. Singh Rai & G. Roberts-Borsani 2026; M. Tang et al. 2026a). If such large C III] EWs are the norm in LRDs, it would hold important clues as to the nature of the

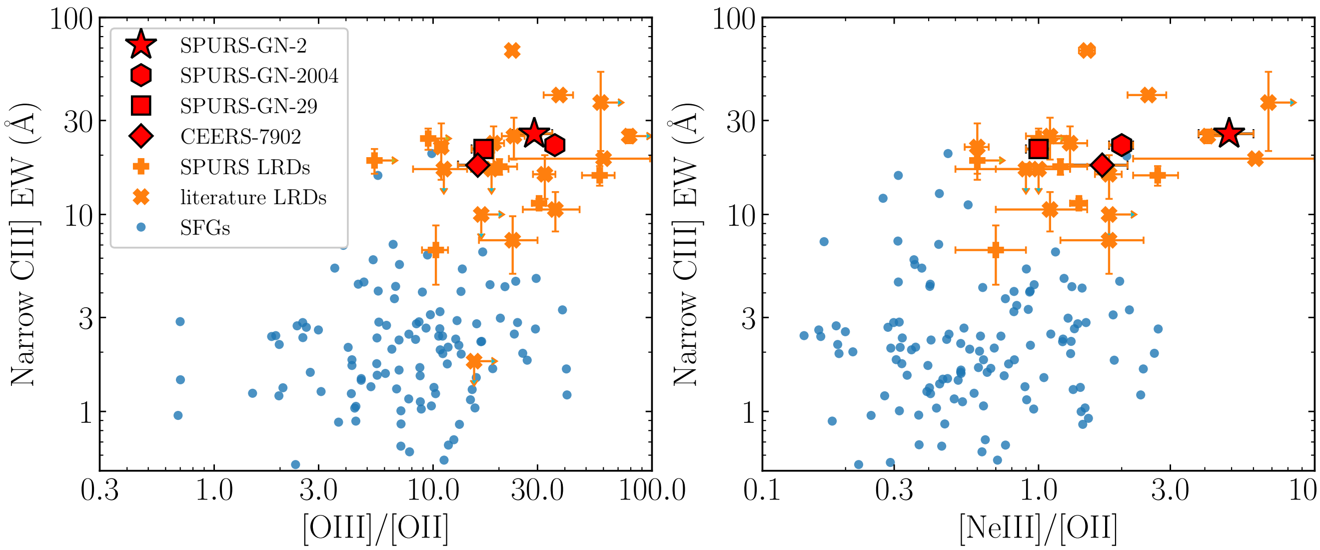

Figure 16. C III] EW versus O32 (left) and C III] EW versus Ne3O2 (right) of LRDs. We plot GN-2, GN-2004, GN-29, and CEERS-7902 as red star, red hexagon, red square, and red diamond, respectively. We also show other LRDs with SPURS spectra (orange plus symbols) or in literature (orange cross symbols; Y. Harikane et al. 2023; R. Maiolino et al. 2024a; A. de Graaff et al. 2025b; D. D. Kocevski et al. 2025; M. Tang et al. 2025; I. Juodžbalis et al. 2026b; S. Mascia et al. 2026; T. Morishita et al. 2026; C. Papovich et al. 2026). For comparison, we overplot star-forming galaxies (E. Curtis-Lake et al. 2026; J. Scholtz et al. 2026b; M. Tang et al. 2026a) as blue circles.

ionizing sources powering the narrow-line gas. Using the NIRSpec archive, we characterize the range of C III] EWs seen in LRDs.

We again utilize the sample of 122 LRDs at $z > 4$ constructed in Section 5.1, searching for C III] emission lines. We identify 20 LRDs with C III] line detections. We detect C III] emission from the archival spectra of 7 LRDs (I. Labbé et al. 2024; R. Maiolino et al. 2024a; A. de Graaff et al. 2025b), and we also recover the C III] detections of the 4 LRDs reported in S. Mascia et al. (2026); T. Morishita et al. (2026); C. Papovich et al. (2026). The remaining 9 LRDs with C III] are from the SPURS program (Table 7), including the 4 presented in this paper. The new C III] detections of the other SPURS LRDs are shown in Figure D.3 in the appendix. We measure the C III] EWs following the same method described in Section 2.2. The C III EWs of these 20 LRDs are generally large, with $16-50-84$ percentiles of 16 Å, 22 Å, and 26 Å (Figure 16). These are above the average C III EWs of star forming galaxies, as measured from composite spectra at similar redshifts ($6-8$ Å; G. Roberts-Borsani et al. 2024; R. Singh Rai & G. Roberts-Borsani 2026; M. Tang et al. 2026a). We do not find C III] emission in the remaining 102 LRDs. The $16-50-84$ percentiles of 5σ limiting C III] EWs of these 102 LRDs are 25 Å, 55 Å, and 112 Å.

We plot the C III] EWs of LRDs as a function of the O32 and Ne3O2 ratios in Figure 16, and we overlay the distribution of galaxies at similar redshifts. It is clear that LRDs lie in a distinct region of the diagram relative to star forming galaxies, with both larger C III] EW and larger O32 and Ne3O2. The O32 and Ne3O2 ratios are sensitive to both ionization parameter and electron density. As we will show below, the offset between LRDs and galaxies can be explained by a combination of effects, with larger ionization parameters, larger electron densities, younger stellar population ages, or additional ionizing sources present in the LRDs.

We now quantify the C III] EW distribution of the LRDs. Here we consider sources with C III] EW > 20 Å. Such strong C III] is thought to trace extremely young stellar populations (< 10 Myr assuming constant star formation history; e.g., A. E. Jaskot & S. Ravindranath 2016; R. Mainali et al. 2020; M. Tang et al. 2021) or AGN activity (K. Nakajima et al. 2018). Among the 122 LRDs, 31 have deep spectra with 5σ limiting C III] EWs reaching 20 Å. We identify 10 LRDs with C III] detections with EWs > 20 Å. This results in a strong C III] fraction of $32^{+11}_{-9}\%$ for LRDs. We compare this fraction against that of the full galaxy population at similar redshift. In M. Tang et al. (2026a), we have assembled a sample of 401 galaxies at $6 < z < 9$ from the archival NIRSpec observations, and we found that $11^{+3}_{-3}\%$ of the galaxies show C III] with EWs > 20 Å. Based on this comparison, it appears that strong C III] emission is roughly three times more common in LRDs than in the full galaxy population at $z \simeq 7$ (Figure 16).

To understand what the strong C III] emission may be revealing about LRDs, we first utilize the BEAGLE tool (J. Chevallard & S. Charlot 2016) to explore the stellar populations required to reproduce C III] with EW > 20 Å. Assuming a constant star formation history, it requires young stellar populations with < 10 Myr with moderate metallicities ($\simeq 0.1\ Z_\odot$) to produce C III] EW > 20 Å. The two largest C III] EWs seen in LRDs are 68 Å (UNCOVER-45924; I. Labbé et al. 2024) and 40 Å (C3PO-46403; C. Papovich et al. 2026). It requires extremely young ($\simeq 2$ Myr) stellar populations to power C III] emission with such large EWs. The UV line diagnostic ratios are consistent with a stellar origin of the strong C III] emission in LRDs. The large O III]/He II ($1.2 - 5.0$) and C III]/He II ($4.3 - 11$) flux ratios seen in the four LRDs are consistent with photoionization models driven by star formation (e.g., A. Feltre et al. 2016; J. Gutkin et al. 2016; M. Mignoli et al. 2019).

Alternatively, it is possible that the strong C III] EWs of LRDs may reflect an additional ionizing source, perhaps associated with a central AGN. It has been shown that very large C III] EWs are often associated with AGN activity at lower redshifts (K. Nakajima et al. 2018). While LRDs are likely mostly enshrouded in dense gas, it is possible that the covering fraction is not uniform, allowing some ionizing radiation to escape to the narrow line region (M. Tang et al. 2026b). Indeed some theoretical models for LRDs suggest that they may have polar cavities where ionizing radiation may be able to escape to the narrow line region (P. Madau & R. Maiolino 2026). While the line ratios are consistent with stellar photoionization, it is possible that the ionizing spectrum associated with LRDs may be softer than most AGNs at lower redshifts.

In summary, we find that the C III] EWs of LRDs are not typical of the galaxy population. They may imply that the host galaxies of LRDs are in the midst of extremely strong bursts of star formation. Among the galaxy population, such bursts are commonly associated with large ionization parameters and high ionized gas densities, both of which would explain the elevated O32 and Ne3O2 ratios we observe in the LRDs. In this picture, the host galaxies of LRDs would preferentially trace the highest specific-star-formation-rate subset of the galaxy population. However, we cannot rule out the possibility that the strong narrow lines instead reflect a significant ionizing contribution from AGN activity. In the following section, we explore whether the SPURS observations reveal massive star signatures that can help distinguish between these two scenarios.

6. DISCUSSION

The deep rest-frame UV spectra of these UV-bright LRDs provide our first opportunity to understand the nature and origin of the UV emission from LRDs, both on scales close to the central engine and within the interstellar medium. In this section we discuss the implications of our discovery of broad C IV emission and dense narrow-line gas for the LRD inner structure (Section 6.1), the implications of the interstellar absorption for the nature of the UV continuum (Section 6.2) and constraints on stellar populations (Section 6.3) in the LRDs. Finally we discuss the origins of nitrogen enhancement in the LRDs and their potential links to the broader population of nitrogen-emitting galaxies (Section 6.4).

6.1. *Broad C IV and Ultra Dense Narrow-Line Gas*

The elevated C III] EWs we measure (Section 5.2) can be explained by either a very young stellar population, or a significant ionizing contribution from the central engine. Distinguishing between these requires evidence that UV continuum photons from the disk or broad-line region reach the narrow-line-emitting gas. Such leakage is a prediction of the orientation-based model of P. Madau & R. Maiolino (2026), in which the gas which makes up the broad-line region occupies an equatorially-concentrated solid angle. This geometry is found in simulations of super-Eddington accretion flows, which indicate that an evacuated, low-density polar structure should be common (e.g., Y.-F. Jiang et al. 2014, 2019; A. Sądowski & R. Narayan 2016; L. Zhang et al. 2025). In this picture, the polar angles will see less of the extremely dense gas clouds, so a substantial fraction of the UV and ionizing continuum should reach the narrow line region. Porosity in the dense gas coverage may also transmit UV radiation beyond the broad-line region (e.g., X. Ji et al. 2026b; V. Sok et al. 2026; M. Tang et al. 2026b). Such covering fraction effects have been argued to explain a subset of narrow high ionization lines (e.g., C. Papovich et al. 2026).

The broad permitted UV lines offer a test of such leakage, provided the chosen transition is both readily produced by the central engine and minimally attenuated by the surrounding gas on its way out. Bound-free absorption from the $n = 2$ level of hydrogen, the process responsible for the Balmer break, extends to all wavelengths shortward of the Balmer limit (3646 Å), but its cross section falls steeply, roughly as ν^{-3}, for photons of increasingly higher energy. Mg II $\lambda2796$ sits close enough to this threshold that it remains strongly attenuated. C IV $\lambda1548$, at nearly twice the threshold photon energy, will face less attenuation. While He II $\lambda1640$ is also far from the Balmer limit, it is very sensitive to the ionizing spectrum, so absence of He II is therefore ambiguous between absorption and an intrinsically soft ionizing spectrum. Among the available transitions, C IV is therefore best suited to this test.

We have shown in this paper that a subset of LRDs have broad C IV emission. GN-2, the bluest source in our sample, shows the strongest broad C IV emission. CEERS-7902, the reddest of the three with C IV coverage, shows broad C IV suppressed by roughly an order of magnitude relative to GN-2. GN-29 is nearly as red as CEERS-7902. It is a weaker C IV emitter overall, with its narrow component fainter than the narrow components of GN-2 and CEERS-7902. Its non-detection of a broad component is therefore inconclusive. Scaling its narrow C IV flux by the broad-to-narrow ratio in GN2 predicts an expected broad flux below our detection limit. Finally the fourth LRD presented in this paper, GN-2004, does not have spectral coverage of the C IV profile.

The presence of broad C IV emission indicates that far-UV radiation from the broad-line region or cocoon escapes the surrounding dense gas in a subset of LRDs. If ionizing radiation also reaches the narrow-line emitting gas, it would imply non-stellar contributions to the narrow emission lines in LRDs. This may help explain some of the extreme narrow line properties seen in LRDs, including the very large C III] EWs we introduced in Section 5.2. We note that (similarly) broad He II remains undetected even in GN-2 and CEERS-7902, where broad C IV demonstrably escapes. We have argued that this favors an intrinsically soft ionizing spectrum, as has been argued previously (e.g., E. Lambrides et al. 2026; B. Wang et al. 2026) and not obscuration as the explanation for the absence of broad He II.

GN-2 is the clearest example of broad C IV transmission in our sample. This LRD has the bluest optical and UV colors, and it is the only source with no detected Balmer line absorption. Its Balmer emission lines have among the largest narrow-to-broad ratios in our sample. Its narrow UV lines imply electron densities of $\gtrsim 1.0 \times 10^6$ cm^{-3} from C III] and $\gtrsim 2.5 \times 10^6$ cm^{-3} from N IV] (Section 3.2 and 3.3), roughly two orders of magnitude above the densities ($\sim 1 \times 10^4$ cm^{-3}) typical of the galaxy population at similar redshift (M. W. Topping et al. 2025b; R. Singh Rai & G. Roberts-Borsani 2026; H. Umeda et al. 2026). These properties can be explained within an orientation-based picture. If our sightline to GN-2 intersects a low-density polar funnel, the blue optical and UV colors may be partially related to leaking continuum emission from the central engine. It is possible that this less obscured sightline allows a deeper view into the AGN, revealing narrow-line gas that is photoionized along the cavity walls. This may boost the narrow-line luminosity and allow visibility of extremely dense material that would not be viewed along more obscured sightlines. Super-Eddington accretion is also predicted to drive fast outflows along the polar direction (e.g., Y.-F. Jiang et al. 2014, 2019; A. Sądowski & R. Narayan 2016; L. Zhang et al. 2025), meaning we should expect to see the fastest outflow signatures in the bluest LRDs. This may be consistent with the broad He II P-Cygni profiles we detect in GN-2 and GN-2004 (Section 3.6), and the broad emission components in N IV], N III], and C III] in GN-2 (Section 3.3).

We emphasize that the optical color of GN-2 classifies it as an LRD, but it is close to the boundary of the little blue dots. In the orientation framework of P. Madau & R. Maiolino (2026), the little blue dots are predicted to be viewed close to pole-on (see below for an alternative interpretation from A. Sneppen et al. 2026b). In the context of P. Madau & R. Maiolino (2026), this suggests GN-2 may represent an intermediate viewing angle, more polar than the other three LRDs in our sample, but not the fully pole-on view associated with little blue dots. In contrast, the redder colors of GN-29 and CEERS-7902 may reflect a more edge-on viewing angle, resulting in more obscuration of the broad C IV photons. Larger spectroscopic samples are required to establish correlations beyond the simple trends we can see with our small SPURS database.

The strength of the broad C IV of GN-2 also can be explained within the electron-scattering cocoon picture. It has the weakest Balmer break and the narrowest broad Hα width. In the context of the column-density sequence linking little blue dots to LRDs (A. Sneppen et al. 2026b), these suggest GN-2 has a lower column density than the other LRDs in the sample. We note, this could also be explained by orientation effects in these models if the column density is reduced along polar sightlines (S. Mascia et al. 2026). This reduced column density (and the associated reduction in $n = 2$ bound-free absorption) may explain its transmitted broad C IV. If the dense neutral gas surrounding the cocoon is clumpy or porous, or has a reduced covering fraction, the transmission of broad C IV may be further boosted.

As C IV is a resonant emission line, it can be a sensitive tracer of ionized gas density and kinematics. Future detailed simulations incorporating C IV radiative transfer into LRD models should prove promising for providing new constraints on the gas close to the central engine. As discussed above, we emphasize that GN-2 is at the boundary of the LRD and little blue dot populations. Even in the context of the dense gas cocoon, this is potentially a regime where there is still significant transmission of UV light from the central nucleus, either in terms of nebular continuum or hot blackbody emission from the disk. We will discuss this possibility in more detail in the next subsection.

6.2. *Deeply Embedded UV Emission in SPURS LRDs*

The origin of the UV emission has been one of the central challenges in understanding LRDs. The dense neutral gas invoked to explain their optical properties should strongly suppress the UV continuum (e.g., A. de Graaff et al. 2025c; H. Liu et al. 2025; A. Sneppen et al. 2026b). The majority of the UV continuum is generally attributed to the host galaxy, though emission from the central source may contribute (e.g., A. de Graaff et al. 2025b; P. Rinaldi et al. 2025; A. P. Cloonan et al. 2026; K. Inayoshi et al. 2026; W. Q. Sun et al. 2026; J. Zhang et al. 2026).

The SPURS spectra open a new window into LRDs' UV continua: revealing a plethora of absorption and fluorescent emission features with no analog in typical star-forming galaxies. Interpreting these features requires first establishing where in the four LRDs this UV continuum originates. NIRCam imaging has shown LRDs are often more extended and clumpy in the UV than the optical (e.g., P. Rinaldi et al. 2025; A. P. Cloonan et al. 2026; J. Zhang et al. 2026), motivating the picture that their UV emission is dominated by the host galaxy. However, LRDs with compact UV emission make up the majority of the spectroscopically-confirmed population: M. Ando et al. (2026) find that the UV sizes in the spectroscopic LRD sample of A. de Graaff et al. (2025b) are significantly smaller than those of star-forming galaxies at fixed UV magnitude and redshift, with many unresolved. Recent prism integral field unit (IFU) spectroscopy of several LRDs has also shown the dominant UV emission component to be spatially compact, and coincident with the optical emission (Y. Ishikawa et al. 2026). The four SPURS LRDs belong to this UV-compact population. Our PSF decomposition demonstrates the majority of their UV emission arises from an unresolved region co-spatial with the optical emission (Section 2.4). Thus, SPURS spectroscopy of these four LRDs probes the UV continuum emerging from or extremely close to the optical-emitting region.

The SPURS spectra reveal the majority of the UV continuum in these LRDs is heavily enshrouded in gas. The detections of strong Lyα damping wings, saturated resonant absorption lines, high EW low oscillator-strength transitions and strong fine-structure absorption lines all indicate a large covering fraction of neutral gas with an extremely high column density ($N_{\rm HI} > 10^{22}$ cm^{-2}) surrounding the UV continuum in all four LRDs (Section 4). We also detect multiple Lyα- and Lyβ-pumped fluorescent emission lines and a forest of narrow Fe II emission lines in the NUV (Section 3.5) that imply comparable neutral gas columns, and that the UV continuum and Lyman series emitting regions must be close to the absorbing gas. These features are essentially negligible in star-forming galaxies at lower and similar redshifts to the LRDs (A. E. Shapley et al. 2003; T. A. Jones et al. 2013; M. Nakane & M. Ouchi 2026; C. Keerthi Vasan G. et al. 2026), and imply significantly higher column density gas conditions than we would expect if typical star-forming regions dominate the UV emission. Together, these results indicate the UV continuum in the SPURS LRDs is deeply embedded behind a very high column density of gas.

The extreme column densities and strong NUV Fe II forest we detect also offer a potential explanation for the rarity of broad Lyα emission across the LRD population. Broad Lyα has, to-date, only been detected in two LRDs (T. Morishita et al. 2026; M. Tang et al. 2026b; X. Ji et al. 2026b; S. Geris et al. 2026; Y. Kageura et al. 2026), including Abell2744-QSO1, the lowest-metallicity LRD identified so far (M. Tang et al. 2026b; X. Ji et al. 2026b), despite being expected to be produced along with the broad Balmer emission. Because a large number of Fe II transitions fall within $\lesssim 1000$ km s^{-1} of the Lyα resonant wavelength (S. Johansson & C. Jordan 1984; T. A. A. Sigut & A. K. Pradhan 2003), a large Fe II column density will provide significant opacity to broad Lyα photons emerging from the central source. This is consistent with the strong Fe II λ2508 emission we detect in GN-2, GN-2004, and CEERS-7902, which requires Lyα photons at > 600 km s^{-1} to reach the Fe II gas to pump this transition. Of these, only CEERS-7902 has coverage of Lyα, and we do not detect emission. This implies broad Lyα does reach the Fe II gas, but negligible flux can escape. Conversely, Abell2744-QSO1, which does show broad Lyα (M. Tang et al. 2026b; X. Ji et al. 2026b) has a very low metallicity (R. Maiolino et al. 2025) and no clear Fe II forest, suggesting a lower Fe II column density. Future spectroscopy of the lowest-metallicity LRDs with weak Fe II emission may reveal more broad Lyα detections.

Given these results, a key question is what powers the UV continuum. One possibility is that the UV continuum originates from the central engine of the LRD, either from the accretion disk itself or nebular emission produced by the dense gas invoked to explain the Balmer break. As the high H I column densities required to produce a Balmer break ($N_{\rm HI} > 10^{23}$ cm^{-2}) would produce a stronger damped Lyα wing than we infer, this implies the UV continuum would need to escape the region where the Balmer break forms along sightlines with lower column densities, as has been proposed in some LRD models (P. Madau & R. Maiolino 2026; S. Mascia et al. 2026). As discussed above, this emission could escape along low-density polar sightlines, or through a porous or clumpy gas envelope.

A second possibility is that the UV continuum comes from young massive stars embedded within an extended gas envelope around the central engine, exterior to the region where the Balmer break forms (see also, e.g., M. Ando et al. 2026; K. Inayoshi et al. 2026). To test whether the neutral gas column densities we infer are consistent with this geometry, we adopt the fiducial dense gas cocoon model of A. Sneppen et al. (2026b). While the ionized cocoon in that model is compact (< 0.05 pc), A. Sneppen et al. (2026b) note it would be depleted rapidly by accretion and outflows, requiring a larger neutral gas reservoir to sustain the LRD. Thus we extend the outer radius to 100 pc, sufficient for a gas depletion timescale > 10 Myr assuming a radiative efficiency $\eta \sim 0.1$. In this configuration, stars within $\lesssim 8$ pc of the nucleus would sit behind a neutral gas column of $N_{\rm HI} \gtrsim 10^{22.6}$ cm^{-2}, comparable to the columns we infer from the Lyα damping wings and absorption lines. This is a conservative estimate: the fiducial model's core column density is extremely high ($N_H \approx 10^{26}\,{\rm cm}^{-2}$), so a lower core density would require stars even closer to the nucleus to reach the same column.

Thus, massive stars embedded deep within a dense gas envelope surrounding the optical emitting region remain a plausible origin for the UV continuum. Indeed, gravitational instabilities in dense gas disks have been proposed to trigger star formation, with the resulting stars and clusters able to migrate inward via disk interactions to build up nuclear star clusters (L. Mayer et al. 2025; K. Inayoshi et al. 2026). If these stars dominate the UV continuum, we may expect to detect their wind and photospheric signatures, which we discuss in more detail below.

Together, these results show that the UV continuum in these LRDs emerges from a compact region deeply embedded in dense gas, possibly probing stars within $\simeq 8$ pc of the central engine. This may indicate that these LRD hosts are in the process of building-up of nuclear star clusters. Since stellar densities are likely to be very high, we may expect dynamical interactions to shape the resulting stellar populations: runaway collisions could build up very massive stars (e.g., S. F. Portegies Zwart & S. L. W. McMillan 2002; M. S. Fujii et al. 2024; A. Rantala et al. 2025), close binary interactions could eject nitrogen-rich material via mass transfer or mergers (P. Senchyna et al. 2024), and tidal disruption of stars by a growing central black hole could expose nitrogen-rich core material as debris (e.g., A. J. Cameron et al. 2023). Whether these results are representative of the LRD population will ultimately require larger samples with deep rest-frame UV spectroscopy.

6.3. *Characterizing Massive Star Features in LRDs*

We have shown in Section 3 that the four LRDs all host highly nitrogen-enhanced ionized gas and high-EW UV emission lines, all of which have now also been observed in a small number of compact, low metallicity galaxies at $z > 6$ (e.g. A. J. Bunker et al. 2023; A. J. Cameron et al. 2023; R. Marques-Chaves et al. 2024; D. Schaerer et al. 2024; P. Senchyna et al. 2024; M. W. Topping et al. 2024). Recently ultra-deep moderate resolution UV spectroscopy has been obtained through SPURS for a subset of the nitrogen emitters. The spectra reveal strong stellar-wind P-Cygni profiles in C IV and N V and broad He II emission, that can be explained via the presence of a population of VMSs ($M_\star \gtrsim 100\,M_\odot$; Z. Chen et al. 2026a; R. Marques-Chaves et al. 2026). It is possible that the winds of VMS drive out the CNO-processed, nitrogen-rich material exposed at their surfaces into the ISM (e.g., J. S. Vink 2023; Y. Shi et al. 2026). The deep spectra have also revealed a broad (FWHM $= 1078 - 1670$ km s^{-1}) component to N IV] λ1486, likely tracing dense WN-like winds or luminous blue variable (LBV)-like outbursts from a population of very massive stars, though an AGN-driven wind cannot be excluded (Z. Chen et al. 2026a; M. Nakane & M. Ouchi 2026). In either scenario, this broad component may trace the gas delivering the nitrogen enrichment. If the nitrogen enrichment follows similar channels in LRDs, we may expect to see similar wind features in SPURS observations presented in this paper.

We briefly summarize potential stellar features in the four SPURS LRDs. As discussed in Section 3.6, we detect a broad He II emission in GN-29, with an EW of 4.1 ± 1.2 Å. The He II profile can be well described with a single Gaussian with a significantly larger (by a factor of 3) FWHM (929 ± 211 km s^{-1}) compared to narrow forbidden lines, yet narrower than the broad Balmer lines. This feature may be most likely explained through optically thick winds of the most massive O stars near the Eddington limit or from WR stars (D. Schaerer 1996; P. A. Crowther 2007; J. Brinchmann et al. 2008; P. Senchyna et al. 2021). The EW of the broad He II emission we measure is slightly larger than what is measured in GN-z11 (Z. Chen et al. 2026a; M. Nakane & M. Ouchi

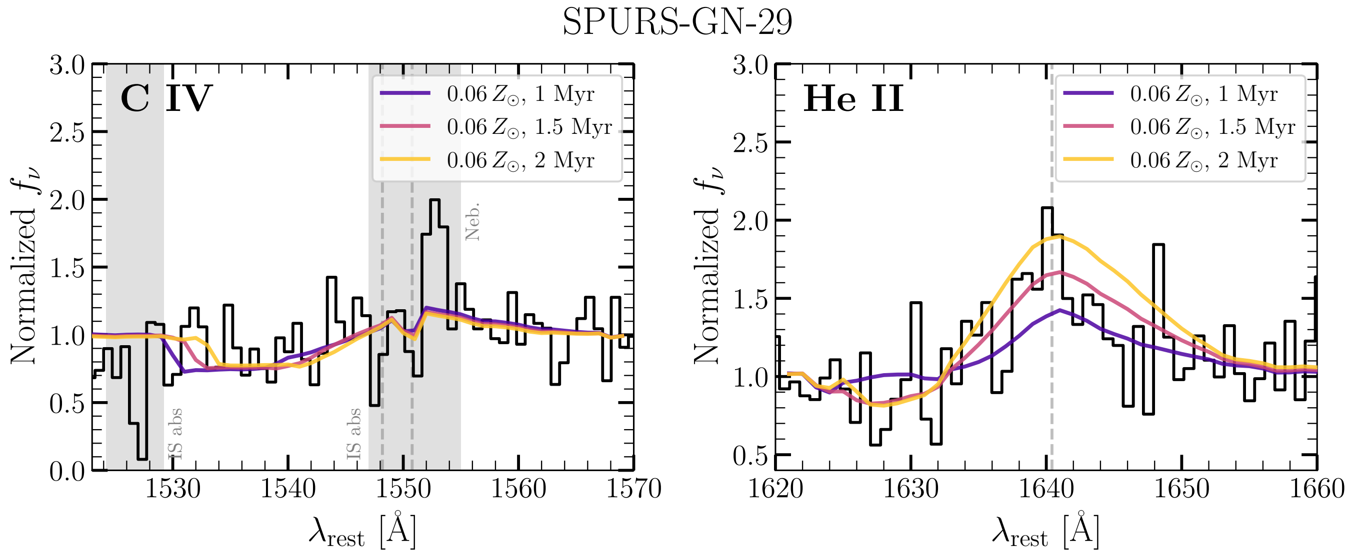

Figure 17. Stellar wind features in GN-29: the observed C IV profile (left) and the detected broad He II $\lambda1640$ emission (right). We compare the continuum-normalized spectrum (black) to predicted stellar wind profiles from the F. Martins et al. (2025) SSP models including VMSs, computed at the low metallicity expected for this source ($Z_\star = 0.06\,Z_\odot$). Colored lines show models in which the optically thick wind mass-loss rate is not scaled down with $Z_\star$ but is instead fixed to the LMC value. Both the strong broad He II emission and the weak C IV P-Cygni absorption can be well reproduced by these VMS models at young SSP ages ($1-2$ Myr), despite this low metallicity, provided that the wind mass loss is enhanced. Grey bands mask the interstellar Si II $\lambda1526$ and C IV absorption and the narrow nebular C IV emission.

2026) while also comparable to other $z > 6$ galaxies suggested to host VMSs (D. Yang et al. 2026). As shown in Figure 11, the He II emission in both GN-2 and GN-2004 shows a likely P-Cygni profile, with broad blueshifted absorption extending to $\approx$ 2900 and 2200 km s^{-1} respectively. These broad He II absorption profiles may probe fast AGN-driven winds or VMS populations (e.g., F. Martins et al. 2025). A broad He II with EW = 4.0 Å is not ruled out in CEERS-7902, where the value is calculated as 3σ upper limit assuming the same FWHM as measured in GN-29. If a recently formed massive star population is present, we also expect to see a strong N V P-Cygni profile, which is covered by the SPURS observations in three of the four LRDs. However, as we have shown in Section 4.2, the spectra near the N V resonance are strongly attenuated by the neutral H I at extremely large column densities ($N_{\rm HI} \approx 10^{22.0-22.7}$ cm^{-2}), leaving an effective transmission of only $0.01-0.04$ at 1239 Å and washing out their P-Cygni features. We also look for a C IV P-Cygni profile, but both GN-2 and CEERS-7902 show strong absorption on top of broad C IV emission, making it challenging to separate the stellar wind component, while the C IV in GN-2004 falls into the detector gap. However, a weak C IV P-Cygni feature is seen in GN-29, allowing us to characterize the stellar population using both C IV and He II wind lines, which we focus on below.

To determine whether the features may be consistent with an origin in massive stars, we compare the observed stellar wind profile in GN-29 with stellar population synthesis models including very massive stars up to 300 $M_\odot$. We consider the models presented in F. Martins et al. (2025), which include two variants that differ in their mass-loss prescriptions of optically thick winds ($\dot{M}_{\rm thick}$), one in which the VMS mass-loss rate is calibrated on the LMC (following G. Gräfener 2021) and is consequently near-independent of metallicity, and one in which this rate decreases at a lower metallicity. We consider models at a stellar metallicity that is informed by the gas-phase oxygen abundance, $12 + \log({\rm O/H}) = 8.13 \pm 0.10$ ($0.28\,Z_\odot$), derived in Section 2.3. As the stellar metallicity is set by iron production dominated by Type Ia supernovae that is delayed relative to oxygen (dominated by Type II supernovae), we expect high-redshift galaxies to be α/Fe-enhanced. To approximate this effect, we consider models at $Z_\star = 0.06\,Z_\odot$, consistent with the factor of five ratio found between gas-phase and stellar metallicities found among $z \simeq 2-3$ galaxies (e.g. C. C. Steidel et al. 2016; R. L. Sanders et al. 2020; M. W. Topping et al. 2020; J. N. Runco et al. 2021) and expected from theoretical limit for Type II supernova yields ($\simeq 0.2\,({\rm O/Fe})_\odot$; K. Nomoto et al. 2006). We also consider models at higher metallicities where these winds are easier to launch, but we consider them unlikely for this source.

As shown in the right panel of Figure 17, the F. Martins et al. (2025) models at $0.06\,Z_\odot$ with $\dot{M}_{\rm thick}$ fixed to LMC metallicity reproduce the observed profile at ages of $1-1.5$ Myr, predicting equivalent widths of 4.1 and 7.0 Å that bracket the observed 4.1 ± 1.2 Å. We note that the models with $\dot{M}_{\rm thick}$ decreasing as a function of metallicity produce at most 1.9 Å of He II emission over the $1-2$ Myr ages at which VMS dominate, and no more than 3.7 Å even at an implausibly high $0.2\,Z_\odot$, suggesting that enhanced mass-loss rates in the VMS are required to match the observed profile. As the C IV P-Cygni absorption is known to trace metallicity for integrated light clusters at fixed other properties, we expect it to weaken as metallicity decreases (e.g. S. A. Rix et al. 2004; C. Leitherer et al. 2010, 2011; A. Vidal-García et al. 2017; J. Chisholm et al. 2019). As expected, at the low metallicity relevant for GN-29, the same models also produce a weak C IV P-Cygni profile (EW $= -1.9$ to -2.1 Å at $1-1.5$ Myr), in agreement with our data (-1.5 ± 0.6 Å).

We also consider other possibilities that may explain the broad He II without requiring very strong stellar winds, but find them to be unlikely. Given the much smaller (by 3×) FWHM of He II in GN-29 compared to the Balmer lines, they are unlikely to share the same kinematics or originate from the BLR (e.g. J. Clavel et al. 1991). In addition, in classical type I AGN, broad He II is accompanied by broad C IV emission line of comparable or greater strength (D. E. Vanden Berk et al. 2001; R. C. Telfer et al. 2002), whereas the C IV emission of GN-29 is narrow (FWHM $= 318 \pm 70$ km s^{-1}). The electron scattering that has been proposed for the broad Balmer lines of LRDs (V. Rusakov et al. 2026; A. Sneppen et al. 2026b) may also produce a broad He II line. However, since the Thomson cross-section is independent of wavelength, its width should also be roughly comparable to those of the Balmer lines, making it unlikely to explain the very different widths we measure for these lines. Winds from an AGN disk may also produce a broad or P-Cygni He II. For the broad-absorption-line and accretion-disk winds that dominate the quasar population, broad He II is generally found with much larger FWHM ($5000-20\,000$ km s^{-1}; e.g., R. J. Weymann et al. 1991; N. Murray et al. 1995; R. R. Gibson et al. 2009). We cannot rule out the case that the outflows associated with the LRDs may be considerably slower, and indeed in the case of GN-2 and GN-2004 we have suggested that the He II P-Cygni profiles may probe AGN-driven winds seen through the polar axis.

We also search for other features that might trace the outflows suggested by the He II profiles. In addition to the broad N IV] discussed further below, we detect broad C III] in GN-2, which can also be powered in WR atmospheres (e.g. D. J. Hillier 1989; W.-R. Hamann et al. 1992; A. Niedzielski & K. Rochowicz 1994). We search for other lines which typically accompany these features; and find that the data for both GN-2 and GN-2004 is potentially consistent with blueshifted absorption in O V λ1371 and emission in C III λ2297, both permitted transitions with a significantly elevated lower level (the direct analogues of N IV λ1719 for these ions) which are common in hot stellar atmospheres and rare to entirely absent in other environments. Indeed, O V λ1371 in particular is rare enough in lower-mass stars but strong enough at high temperatures to be employed as a tracer of VMS and hot WR populations in integrated light spectra, emerging in many young clusters including R136 (e.g. A. Wofford et al. 2014; L. J. Smith et al. 2016; P. A. Crowther et al. 2016; F. Martins et al. 2023). If confirmed, this O V absorption (see Figure 18) would suggest that a large fraction of the UV continuum is likely stellar in origin (or otherwise cloaked in exceptionally hot and dense gas). We emphasize that these features and their associations are tentative at the current SNR and will require dedicated modeling; but this suggests that deeper spectroscopy, which could more clearly constrain these fainter features, might shed significant light on the origin of these other broad UV lines.

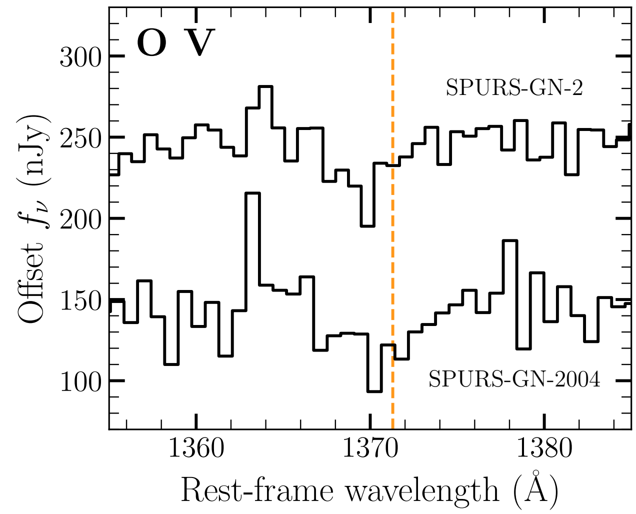

Figure 18. Zoom-in on the O V λ1371 region in the observed spectra of GN-2 (top) and GN-2004 (bottom). Both sources show a broad absorption feature spanning ≈ 1367–1372 Å, consistent with being from stellar winds of VMS or hot WR populations.

To summarize, we detect wind signatures in the SPURS LRD spectra that may indicate the presence of VMSs. In the case of GN-29, we have demonstrated that population synthesis models with VMS are able to

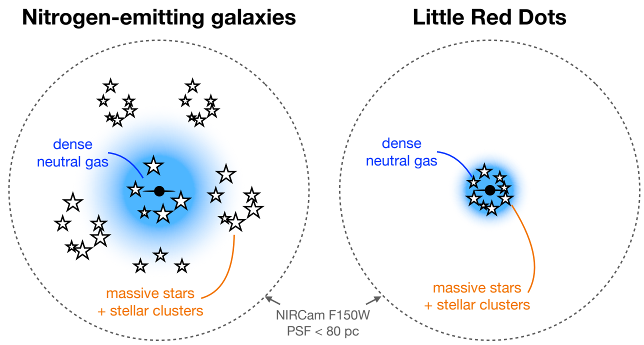

Figure 19. Schematic illustrating similarities and differences between LRDs and nitrogen emitting galaxies and the sub-PSF dense stellar systems they potentially trace.

reproduce the observed strong, broad He II and weak C IV. In GN-2 and GN-2004, the He II profiles appear P-Cygni in shape, with very fast winds ($\gtrsim 2200\,\mathrm{km\,s^{-1}}$). Whether these trace winds are powered by massive stars or an AGN is not clear, but in either case the winds may be important for delivering the nitrogen-enhanced abundance pattern to the ISM, as suggested in Z. Chen et al. (2026a). We consider the prevalence of nitrogen emission in the LRDs in the next subsection.

6.4. *Nitrogen Emission in LRDs*

We have shown that all four LRDs in our paper host highly nitrogen-enhanced gas (Section 3.3). Our archival analysis demonstrates this is not unique to our small sample: nitrogen emission appears roughly 8× more common among LRDs than in the broader galaxy population at these redshifts (Section 5.1). The origin of nitrogen enhancement in early galaxies has been debated in the literature (e.g., A. J. Cameron et al. 2023; C. Charbonnel et al. 2023; C. Kobayashi & A. Ferrara 2024; P. Senchyna et al. 2024; W. McClymont et al. 2026), and its prevalence in LRDs may offer new clues to the physical conditions that produce it.

JWST has now obtained spectra for over a thousand galaxies at $z > 6$ (e.g., K. E. Heintz et al. 2025; F. Valentino et al. 2025), spanning a wide diversity of ISM conditions and stellar populations. Yet within this range, LRDs and nitrogen-emitting galaxies[13] do not appear to be broadly distributed; instead, their properties overlap, occupying only a small region of the parameter space populated by the full sample (see Figure 19 for a schematic). One of the hallmarks of both populations is extremely compact UV emission ($\lesssim 80$ pc), suggesting a very dense complex of star clusters (e.g., S. Tacchella et al. 2023; M. W. Topping et al. 2024). In addition, both show high ionized gas densities (Section 3.3, M. W. Topping et al. 2024, 2025b; R. Maiolino et al. 2024b; Z. Chen et al. 2026a; C. Papovich et al. 2026), fluorescent O I* emission, requiring dense neutral gas close to the ionizing sources (S. Choe et al. 2025; R. Tripodi et al. 2025b; Z. Chen et al. 2026a; V. Kokorev et al. 2026), and in some cases, potential signatures of very massive stars (see Section 6.3; Z. Chen et al. 2026a).

These similarities point to a common origin of nitrogen enhancement within high density environments. In the LRDs studied in this paper, the gas columns we infer are consistent with a UV-emitting source confined to within as little as ~ 8 pc of the central engine, pointing to an environment where nuclear clusters are being assembled. Dynamical interactions are likely to be common in dense star clusters on such small scales, with runaway stellar collisions potentially building-up populations of VMS (e.g., A. Rantala et al. 2024, 2026). It is even plausible that supermassive stars (SMS; $M_\star > 10^3\,M_\odot$) might be effectively formed in these dense metal poor conditions (S. Chon & K. Omukai 2025; M. Gieles et al. 2025). There are many papers emphasizing why such high density environments may spark the nitrogen enhancement. The winds of VMS or SMS populations can efficiently transport CNO-processed, nitrogen-rich material into the surrounding gas, offering a natural explanation for the elevated N/O and N/C ratios seen in both LRDs and nitrogen emitters (e.g., C. Charbonnel et al. 2023; J. S. Vink 2023; D. Nandal et al. 2025; Y. Shi et al. 2026). Close binary interactions among massive stars in these same dense environments can eject comparably nitrogen-rich material through non-conservative mass transfer or stellar mergers (P. Senchyna et al. 2024).

These same dense nuclear environments also raise the possibility that the central black hole itself contributes directly to the nitrogen budget, through tidal disruption events (TDEs). In sufficiently dense clusters, close stellar encounters can readily scatter stars onto orbits that bring them within the tidal disruption radius of the central black hole. Since intermediate- and high-mass stars carry substantial CNO-processed material in their cores, the resulting debris can be strongly nitrogen-enhanced, offering an additional enrichment channel (A. J. Cameron et al. 2023; B. Mockler et al. 2024; K. Watanabe et al. 2026). The high frequency of nitrogen enhancement among LRDs suggests this possibility deserves serious consideration. Whether the nitrogen-emitting galaxies also harbor supermassive black holes in their nuclei remains debated (e.g., R. L. Larson et al. 2023; R. Maiolino et al. 2024b). Deep observations

[13] We will refer to N IV] and N III] emitters that are not LRDs as nitrogen-emitting galaxies.

from SPURS have revealed broad N IV] emission lines in nitrogen-emitting galaxies (Z. Chen et al. 2026a; M. Nakane & M. Ouchi 2026), suggesting the presence of dense, nitrogen-rich outflows. This has been interpreted as evidence for WN-like winds or LBV-like outbursts, though an AGN-driven wind cannot be ruled out. In the latter case, rather than producing the nitrogen-rich material directly, the AGN outflow may instead be driving out a pre-existing reservoir of TDE or dense cluster debris, polluting the surrounding interstellar medium with nitrogen-rich material. The presence of broad N IV] in GN-2 (Section 3.3) suggests such winds may be present in a subset of LRDs as well.

Despite their similarities, the nitrogen-emitting galaxies' spectra also differ from LRDs in several ways. They do not show the prominent red optical colors of LRDs, and their spectra exhibit neither Balmer breaks nor Balmer line absorption. While samples remain small, deep UV spectra from SPURS have revealed another key difference: low-ionization interstellar absorption lines are much weaker in nitrogen-emitting galaxies than in LRDs, implying a lower covering fraction of neutral gas and a UV continuum that is less deeply embedded than in LRDs. It may be that these two populations represent a continuum along the density sequence of high-redshift galaxies, with LRDs corresponding to the most concentrated and densest systems. The nitrogen-emitting galaxies may share a similar, albeit slightly less dense, nuclear structure to LRDs ($\lesssim$ 10 pc scales). But while the UV light of LRDs we present in this paper may be very highly concentrated (resulting in the strong absorption lines)[14], the UV output of the nitrogen-emitting galaxies is instead dominated by surrounding young star clusters ($\lesssim$ 100 pc scales) that are not deeply embedded within neutral gas[15]. This framework was recently proposed by Z. Chen et al. (2026a) to simultaneously explain the presence of broad Lyα and fluorescent emission lines alongside weak low-ionization absorption lines in the nitrogen-emitting galaxy GN-z11. This picture remains speculative owing to the small samples with deep spectroscopy. Larger spectroscopic databases are required to test whether the LRDs and nitrogen-emitting galaxies studied to-date are representative.

[14] We note that LRDs are often surrounded by blue clumps, but these are often found on larger physical scales ($>$ 100 pc) than we are discussing here (J. F. W. Baggen et al. 2026; F. Pacucci & C. M. Urry 2026).

[15] It is worth emphasizing that the young star clusters that are proposed to surround the nucleus in this picture remain unresolved at NIRCam resolution.

7. SUMMARY

We present ultra-deep (29 hours) JWST/NIRSpec G140M (rest-frame UV) spectroscopy of four UV-bright ($M_{UV} < -20$) LRDs in the GOODS-N and EGS fields at $z \simeq 7$: GN-2, GN-2004, GN-29, and CEERS-7902. The data were obtained as part of the SPURS Cycle 4 Large Program. These observations provide the deepest rest-frame UV view of LRDs yet obtained at medium resolution ($R \simeq 1000$) and provide new insights into the origin of LRD's UV emission and the conditions responsible for extreme nitrogen enhancements in the early universe. The ultra-deep spectra reveal the first detections of broad high ionization UV emission lines in LRDs and provide the first view of the gas surrounding the UV continuum-emitting sources in LRDs. We summarize the key results below.

1. With the SPURS spectra, we characterize the rest-frame UV to optical spectroscopic properties of the four LRDs. These systems span wide ranges of continuum slopes among the LRD population. GN-2 and GN-2004 are blue from rest-frame FUV ($\beta_{\rm FUV} = -2.39$ to -1.95) to optical ($\beta_{\rm opt} = 0.06 - 0.09$), while GN-29 and CEERS-7902 are redder ($\beta_{\rm FUV} = -1.41$ to -0.76, $\beta_{\rm opt} = 0.40 - 0.48$). The Balmer lines show both narrow and broad emission, with larger narrow-to-broad Hα flux ratios in GN-2 and GN-2004 than GN-29 and CEERS-7902. These may reflect different relative contributions of host galaxy or AGN versus dense gas cocoon emission among the four LRDs. We find large ionization-sensitive line ratios (O32 $= 16 - 36$, Ne3O2 $= 1.0 - 4.9$) in all four LRDs, likely indicating both large ionization parameters and high electron densities in the narrow-line emitting gas.

2. The ultra-deep spectra reveal the first detections of broad high ionization lines in the UV. We detect a strong broad (FWHM = 2830 km s^{-1}) C IV emission line in the G140M spectrum of GN-2 and a weaker broad C IV in CEERS-7902. The broad C IV to Hβ flux ratios of both LRDs are well below those of typical type I AGN, consistent with previous results suggesting LRDs have soft ionizing spectra. We also detect many other narrow UV emission lines (N IV], He II, O III], Si III], C III]) in the four LRDs. We detect nitrogen emission lines in all four LRDs, which indicate nitrogen-enhanced abundance patterns with super-solar N/O and N/C ratios. In GN-2 we detect broad emission components in N IV] (similar to that detected in GN-z11; Z. Chen et al. 2026a), N III], and C III], indicating fast moving ionized gas. Using the density-sensitive N IV], Si III], and C III] doublet ratios, we derive large electron densities for the four LRDs, well above that of typical galaxies at $z \simeq 7$. In particular, GN-2 has an extremely high electron den-

sity ($\gtrsim 10^6$ cm^{-3}) that is two orders of magnitude above the typical $z \simeq 7$ value.

3. The continuum spectra of all four LRDs show strong downturns near the Lyα wavelength, extending to $\gtrsim$ 1300 Å in the rest frame, and extremely strong absorption lines, including detections of usually weak fine-structure absorption. Reproducing these downturns requires exceptionally large H I column densities ($N_{\rm HI} \approx 10^{22.0-22.7}$ cm^{-2}). The low-ionization absorption lines are strong and saturated, with EWs (median ranging -2.2 Å to -1.2 Å in each source) well above those measured in star-forming galaxies at comparable redshifts, and implying near-unity covering fractions ($C_f = 0.7 - 1.0$). Together, these results indicate the UV-emitting regions are deeply embedded in neutral gas that covers nearly the entire source. We detect strong Al II λ1670 and Al III $\lambda\lambda$1854, 1862 absorption, motivating investigation of aluminum abundances that potentially offer a signpost of supermassive and very massive star enrichment, but find that line saturation and ionization effects prohibit conclusive results.

4. Consistent with the picture from the absorption lines, we detect a suite of low-ionization fluorescent emission lines, indicating pumping by the UV continuum and Lyman series photons in dense neutral gas. Fluorescent O I* λ1306 in GN-2 and GN-2004 requires Lyβ pumping in dense H I gas close to the ionizing sources, while the rare semi-forbidden O I] λ1641 line detected in GN-2 implies extreme column densities $N_{\rm HI} > 10^{22.5}$ cm^{-2}. The NUV spectra of all four LRDs also show a forest of strong, narrow, permitted Fe II emission, with the total NUV Fe II EWs ranging from 72 to 356 Å. (integrated over $2200 - 3090$ Å). Three LRDs show extremely strong narrow Fe II λ2508 emission (EW $= 6 - 10$ Å, deconvolved FWHM $\lesssim$ 464 km s^{-1}), requiring pumping by broad Lyα in a dense, iron-rich region. We suggest this region may regulate the visibility of broad Lyα from the central engine in the LRD population.

5. We explore the incidence of N IV], N III] emission and strong C III] emission in a sample of 122 $z > 4$ LRDs with NIRSpec rest-frame UV spectroscopy. Strong C III] (EW $>$ 20 Å) in LRDs is about three times more common than in the galaxy population. This suggests that the host galaxies of LRDs are more likely to be in the midst of intense bursts of star formation or with a significant ionizing contribution from an AGN. We find that 56^{+14}_{-14}% of $z > 4$ LRDs present N IV] or N III] detections with EW $>$ 5 Å. This fraction is $\sim 8\times$ larger than that of the full galaxy population (M. W. Topping et al. 2025b).

6. We investigate the dense gas properties that can explain the strong broad C IV emission in GN-2. GN-2 has one of the bluest UV and optical colors among LRDs, no clear Balmer line absorption, and signatures of extremely dense and fast-moving ionized gas. The presence of broad C IV requires FUV radiation from the central engine to escape through the surrounding dense gas, suggesting GN-2 is viewed along a less obscured sightline than other LRDs in our sample. This could be explained by orientation-based models, in which sightlines closer to the polar direction intercept a smaller column of broad-line-region clouds and may be more aligned with ionized outflows from the accretion disk. Alternatively, in the dense gas cocoon picture, GN-2 may have a lower covering fraction or column density of dense neutral gas surrounding its nucleus than the rest of our sample.

7. The absorption lines and Lyα damping wing demonstrate the UV continuum in these four LRDs is deeply embedded in neutral gas. In our sample we find the UV continuum emerges from a compact, unresolved ($<$ 80 pc) region co-spatial with the optical emission. The UV continuum could be consistent with escaping emission from the central engine along low column density sightlines, or young massive stars embedded within an extended dense gas envelope surrounding the central engine. If massive stars produce the UV emission, we find they would need to be confined to within just $\lesssim$ 8 pc of the nucleus to be consistent with the column densities inferred from the UV absorption features, implying extremely concentrated stellar systems.

8. The spectra reveal He II wind signatures in three LRDs that may indicate the presence of very massive stars (VMS), but can also be consistent with AGN-driven winds. In either case, we argue these winds could deliver the nitrogen-enhanced material into the ISM. In GN-29, we detect a strong, broad He II emission line (EW $= 4.1 \pm 1.2$ Å, FWHM $= 929 \pm 211$ km s^{-1}) together with weak C IV P-Cygni absorption, which are well reproduced by stellar population synthesis models including VMS. In GN-2 and GN-2004, the He II profiles instead show blueshifted P-Cygni absorption, indicating fast winds out to $\gtrsim$ 2200 km s^{-1} that could be driven either by massive stars or by an AGN.

9. Among the broader population of $z > 4$ galaxies observed with JWST, LRDs and nitrogen-emitting galaxies stand out as a small, tightly overlapping subset, sharing nitrogen-enhanced abundance patterns, elevated narrow-line electron densities, and compact UV emission not seen in typical star-forming systems at these redshifts. We argue that this points to a common origin in dense nuclear environments, where massive stars are concentrated in compact clusters surrounded by extremely dense gas, and where dynamical interactions,

including runaway stellar collisions, binary mass transfer, and tidal disruption of stars by the central black hole, can efficiently enrich the surrounding gas with nitrogen. Despite these similarities, nitrogen-emitting galaxies show markedly weaker low-ionization absorption than LRDs, implying a lower covering fraction of neutral gas and a less deeply embedded UV continuum. We propose that LRDs and nitrogen emitters may represent a sequence in gas column density around a similar underlying nuclear structure, with LRDs at the densest, most deeply embedded extreme.

ACKNOWLEDGMENTS

The authors thank Liang Dai, Yuzo Ishikawa, and Harley Katz for helpful conversations, Stéphane Charlot and Jacopo Chevallard for providing access to the `BEAGLE` tool, and Fabrice Martins for sharing their population synthesis models. MT is supported by the National Natural Science Foundation of China (grant No. 12673014). DPS acknowledges support by the National Science Foundation under Grant No. AST-2109066. CAM acknowledges support by the European Union ERC grant RISES (101163035), Carlsberg Foundation (CF22-1322), and VILLUM FONDEN (37459). ZC acknowledges support by VILLUM FONDEN under grant 37459. SSG and VG acknowledge support by the Carlsberg Foundation (CF22-1322). LW acknowledges support from the Gavin Boyle Fellowship at the Kavli Institute for Cosmology, Cambridge and from the Kavli Foundation. KVGC is supported by NASA through the STScI grants JWST-GO-03777, JWST-GO-04265, and JWST-GO-05974. The Cosmic Dawn Center (DAWN) is funded by the Danish National Research Foundation under grant DNRF140.

This work is based in part on observations made with the NASA/ESA/CSA JWST. The data were obtained from the Mikulski Archive for Space Telescopes at the Space Telescope Science Institute, which is operated by the Association of Universities for Research in Astronomy, Inc., under NASA contract NAS 5-03127 for JWST. These observations that form the basis of this work are associated with program GO 9214 (SPURS). The authors thank the program coordinator, Christian Soto, and NIRSpec reviewer, Diane Karakla. This work also uses observations associated with the following publicly available programs: GTO 1180, 1181, GTO 1210, GTO 1286, GTO 1287, and GO 3215 (JADES, doi:10.17909/8tdj-8n28), ERS 1345 and DDT 2750 (CEERS, doi:10.17909/z7p0-8481), GO 2561 (UNCOVER), GO 4233 (RUBIES), GO 6368 (CAPERS), and GO 8018 (DIVER). The authors acknowledge the above teams led by Daniel Eisenstein & Nora Lüetzgendorf, K. Isaak, Steven L. Finkelstein, Pablo Arrabal Haro, Ivo Labbé & Rachel Bezanson, Anna de Graaff & Gabriel Brammer, Mark Dickinson, and Xiaojing Lin for developing their observing programs. Some of the data products presented herein were retrieved from the Dawn JWST Archive (DJA). DJA is an initiative of the Cosmic Dawn Center (DAWN), which is funded by the Danish National Research Foundation under grant DNRF140. The Tycho supercomputer hosted at the SCIENCE HPC center at the University of Copenhagen was used for supporting this work.

Facilities: JWST(NIRSpec)

Software: `msaexp` (G. Brammer 2023), `emcee` (D. Foreman-Mackey et al. 2013), `pysersic` (I. Pasha & T. B. Miller 2023), `fantasy` (D. Ilić et al. 2023), `NumPy` (C. R. Harris et al. 2020), `SciPy` (P. Virtanen et al. 2020), `Astropy` (Astropy Collaboration et al. 2013, 2018, 2022), `Matplotlib` (J. D. Hunter 2007), `BEAGLE` (J. Chevallard & S. Charlot 2016).

APPENDIX

A. BIC ANALYSIS OF EMISSION LINE FITTING

The N IV], N III], C III], He II, and [O III] emission lines of the four LRDs present complex profiles with multiple components. To interpret each of these lines, we fit the line profile with different models. We evaluate the goodness of fit of each model using the Bayesian Information Criterion (BIC; G. Schwarz 1978; A. R. Liddle 2007). The BIC of each model fit is defined as: BIC $\equiv -2\ln\mathcal{L} + k\ln N$, where $\mathcal{L}$ is the maximum likelihood achievable by the model, k is the number of parameters of the model, and N is the number of data points used in the fit. When comparing two models, we take ΔBIC > 10 as very strong evidence that the model with the lower BIC provides a better fit to the data than the other. The best-fit results are presented in Table 3 (for N IV], N III], C III], He II emission lines) and Table D.2 (for [O III] lines).

We first fit the C III] profile of GN-2 with two narrow Gaussians, fixing the two centroids to the rest-frame wavelengths of [C III] λ1907, C III] λ1909. We allow the peak fluxes of the two Gaussians and the line width to vary as free parameters, but require the two line widths to be the same. Here we mask out the region with Fe III λ1914. We find excess emission on both blue and red sides of the C III] profile, likely suggesting the presence of a broad C III] component. With this model, we derive a large reduced chi-square value ($\chi^2_\nu = 2.7$) and a large BIC value (135). We then simultaneously fit the C III] of GN-2 with two narrow Gaussians and two broad Gaussians. Again we fix the centroids of the two broad Gaussians to the rest-frame wavelengths of the doublet. The fitting results are presented in Section 3.2. This model well reproduces the C III] profile of GN-2 (Figure 7) with broad C III] with FWHM of 2271 ± 371 km s^{-1}. We find much lower χ^2_ν (1.3) and also lower BIC (83). The difference between BIC values of the two fits (ΔBIC = 52) indicates that the model with a broad component provides a much better fit to the C III] profile.

We also fit the C III] profiles of GN-2004, GN-29, and CEERS-7902 with the two models described above: two narrow Gaussians only and a combination of two narrow and two broad Gaussians. For each of these three LRDs, we perform the BIC test for C III]. We do not find a significant difference between fitting C III] with both models (ΔBIC ≤ 1). When fitting C III] with two narrow and two broad Gaussians, the inferred broad C III] components have S/N below 3. These indicate that we do not detect clear broad C III] in these three LRDs (Figure 7).

The SPURS spectrum of GN-2 reveals the detection of a broad N IV] component. Motivated by this, we simultaneously fit the N IV] profile of GN-2 with two narrow Gaussians and two broad Gaussians, with centroids fixed to the rest-frame wavelengths of [N IV] λ1483, N IV] λ1486. We present the fitting results in Section 3.3. This model well reproduce the N IV] profile (Figure 7), with a χ^2_ν of 1.1 and a BIC of 66. The best-fit broad N IV] component has a FWHM of 1514 ± 137 km s^{-1}. We also examine whether the N IV] of GN-2 can be fitted by two narrow Gaussians only. With this fit, we derive considerably larger χ^2_ν (4.1) and BIC (159). The difference in BIC (ΔBIC = 60) suggests that the model including a broad component is strongly preferred.

GN-29 and CEERS-7902 also show N IV] detections. We fit each of the N IV] profiles with models with and without a broad component. We then perform the BIC test for these fits. For both CEERS-7902 and GN-29, we do not find a significant difference between fitting N IV] with the two models (ΔBIC ≤ 1). The broad components inferred from the model with broad Gaussians also have S/N below 3. These results demonstrate that there is no clear broad component underlying the N IV] of these two LRDs (Figure 7).

We model the individual components of the N III] $\lambda 1746 - 1754$ quintuplets of GN-2 and GN-2004, which show high S/N ($= 17 - 27$) N III] detections. We first fit the N III] profile of GN-2 with five narrow Gaussian functions following the methodology described in R. Maiolino et al. (2024b) and Z. Chen et al. (2026a). The centroids of the five narrow Gaussians are fixed to the rest-frame wavelengths of individual quintuplet lines. We also require the line widths of the five components to be the same, and fix the following flux ratios according to the theoretical values: $f_{\mathrm{NIII]}\lambda1746}/f_{\mathrm{NIII]}\lambda1752} = 0.14$, $f_{\mathrm{NIII]}\lambda1748}/f_{\mathrm{NIII]}\lambda1754} = 0.95$. With this model, we derive a large χ^2_ν value (3.6) and a large BIC (151). We find excess emission in the blue side of the N III] profile, likely suggesting the presence of a broad N III] component. We then model the N III] profile of GN-2 with five narrow Gaussians and a broad Gaussian, allowing the centroid, peak flux, and line width of the broad component to vary freely. The fitting results are presented in Section 3.3. By adding the broad component (FWHM $= 1797 \pm 219$ km s^{-1}), we find a significantly lower χ^2_ν (1.6) and lower BIC (81). The difference in BIC (ΔBIC = 70) indicates that the model with broad component indeed fits the N III] profile of GN-2 better (Figure 7). We perform the same fits to the N III] emission of GN-2004. Again, we find that the model including a broad component is strongly preferred to reproduce the N III] profile of GN-2004 with a much lower BIC (27) than the model with five narrow components only. For GN-29 and CEERS-7902, we do not resolve the N III] quintuplet lines owing to the relatively low S/N ($= 4 - 6$).

The He II λ1640 emission line is coupled with nearby O I] λ1641 emission. To resolve both lines for the four LRDs, we fit each He II profile with two Gaussians. We fix the two centroids to the rest-frame wavelengths of He II λ1640 and O I] λ1641, respectively. We allow the two peak fluxes and the line width of He II to vary as free parameters, while we fix the line width of O I] to be the same as O III] λ1666. This model well reproduces the He II profile of GN-2 ($\chi^2_\nu = 1.2$, BIC = 21), and we identify the O I] λ1641 emission with S/N = 3 (Section 3.5). We also fit the He II of GN-2 with a single Gaussian with centroid fixed at the rest-frame wavelength of He II λ1640. With this model, we find excess emission on the red side of the line profile with a large χ^2_ν (2.2) and a large BIC (35). The difference in BIC (ΔBIC = 14) indicates that the model including both He II and O I] is significantly preferred over the model with He II only. For GN-2004, GN-29, and CEERS-7902, we do not find O I] (S/N < 1.5) when modeling the line profile with two Gaussians. We then fit their He II profiles with single Gaussians. With this model, we find no difference compared to fitting with two Gaussians (ΔBIC $= 0 - 2$), suggesting that there is no clear O I] λ1641 detection in these three LRDs (Figure 11).

Finally, we test whether the [O III] λ4959, λ5007 emission lines of the four LRDs present broad components, as have been revealed in a few LRDs in the literature (e.g., I. Juodžbalis et al. 2024). For each LRD, we consider two models: one fitting [O III] λ4959, λ5007 with two narrow Gaussians only, and one with two narrow and two broad Gaussians. We mask out the region including Hβ when performing the fits. For two narrow Gaussian model, we fix the centroids to the rest-frame wavelengths of [O III]. We allow the peak flux and line width of [O III] λ5007 to vary as free parameters, fix the flux of [O III] λ4959 according to the theoretical line ratio ($f_{[\mathrm{OIII}]\lambda4959} : f_{[\mathrm{OIII}]\lambda5007} = 1 : 2.98$), and require the line width of λ4959 to be the same as λ5007. With this model, we find excess emission in both blue and red sides of [O III] profiles of each LRD, potentially indicating the presence of broad components. We then simultaneously fit the [O III] doublet of each LRD with two narrow and two broad Gaussian functions, setting the parameters of broad Gaussians in the same way as narrow Gaussians described above. This model can well reproduce the [O III] doublet profiles of all the four LRDs ($\chi^2_\nu = 1.2 - 1.5$), revealing the presence of broad [O III] components (FWHM $= 1130 - 1627$ km s^{-1}). The fitting results are presented in Section 2.3. Comparing to models including narrow Gaussians only, the differences in BIC (ΔBIC $= 39 - 621$) strongly prefer models with broad components (Figure D.2).

B. Hα EMISSION LINE FITTING

The Hα emission lines of the four LRDs show both narrow and broad components, and we also find Hα absorption features in three LRDs (GN-2004, GN-29, CEERS-7902). In order to interpret the Hα complex, we fit each Hα line with multiple different models. Following the framework presented in Appendix A, we assess the goodness of fit using the Bayesian Information Criterion and reduced chi-square values.

We first assume the Doppler velocity broadening of Hα, and consider whether the line profile can be fitted by a combination of a narrow (FWHM $\lesssim 500$ km s^{-1}) and a broad (FWHM $\gtrsim 1000$ km s^{-1}) Gaussian. When an absorption feature is present, we fit the absorption line with an additional Gaussian. We allow the centroid, peak flux, and line width of each Gaussian to vary as free parameters. We additionally fit the [N II] $\lambda\lambda$6548, 6584 emission lines with two Gaussians, fixing the centroids to the rest-frame wavelengths of [N II] and fixing the λ6548 : λ6584 flux ratio to the theoretical value (3.05). We do not find significant [N II] emission (S/N < 3) in any of the four LRDs, and the results do not change with and without fitting [N II]. Therefore, we only consider fitting Hα for the four LRDs. With this model, we find excess flux in both blue and red wings of the Hα profiles of all four LRDs. The χ^2_ν values are large ($2.2 - 5.7$), indicating that the Hα profiles cannot be well reproduced with a single broad and a narrow emission.

Recent studies have found that the broad Hα emission of LRDs can be better fitted by double-Gaussian profiles when S/N is high enough (e.g., F. D'Eugenio et al. 2025, 2026). Motivated by this, we simultaneously fit each Hα line with a narrow and two broad Gaussian functions. Again, for the three LRDs presenting absorption features, we include another Gaussian. The fitting results are described in Section 2.3, and we show the best-fit models in Figure B.1. The model can well reproduce the Hα profile, with χ^2_ν values of $1.1 - 1.4$. Comparing to model including one narrow and one broad Gaussian, the differences in BIC (ΔBIC $= 108 - 469$) indicate that the three-Gaussian model is strongly preferred in fitting Hα of the four LRDs.

It has also been argued that the Balmer emission lines of LRDs can be broadened by electron scattering, and thus the broad Balmer lines show exponential wings (e.g., J. Matthee et al. 2024; V. Rusakov et al. 2026). We then consider this scenario by fitting the Hα profile with an exponential model following the methodology described in J. Matthee et al. (2026). This model can be described by the following equation:

$$I(\lambda) = N(\lambda) + (1 - f) \cdot G(\lambda) + f \cdot (G * E)(\lambda),$$

where $N(\lambda)$ is a Gaussian function describing the narrow emission, $G(\lambda)$ is a Gaussian with intermediate width describing the intrinsic (unscattered) emission from BLR. The exponential wing produced by electron scattering is described by $f \cdot (G * E)(\lambda)$, that a fraction (f) of intrinsic BLR emission is scattered, where E is an exponential convolution kernel:

$$E(\lambda) \equiv (1/2W) \cdot \exp\left(-|\lambda - \lambda_0|/W\right).$$

Where λ_0 is the centroid of Hα, W is the e-folding scale. The FWHM of the broad exponential wing can be expressed by FWHM $\approx 2 \ln 2 \cdot W$. Here we allow the centroids, peak fluxes, line widths of Gaussians, as well as the scattering fraction f and e-folding scale W to vary as free parameters.

We show the exponential model fitting results in Table B.1, and we plot the best-fit models in Figure B.2. The exponential model can also well reproduce the Hα

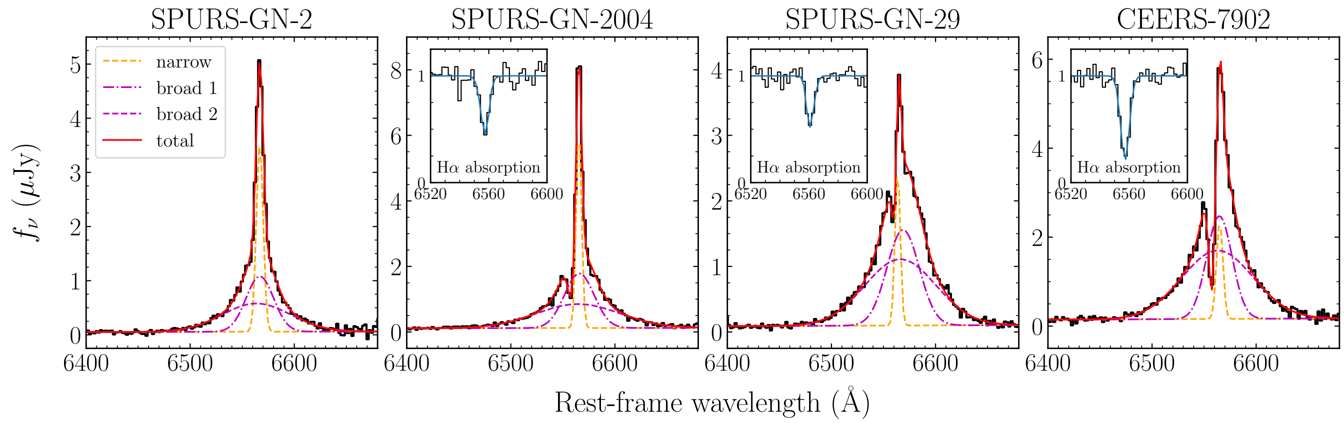

Figure B.1. Three-Gaussian fits to the Hα emission line profiles of the four LRDs. For each object, the narrow Hα emission component is shown as the orange dashed line. The broad Hα is described by the sum of two components (magenta dashed and dotted lines). In the upper left corner of GN-2004, GN-29, and CEERS-7902, we show the absorption components. The total best-fit Hα line profiles are shown as red solid lines.

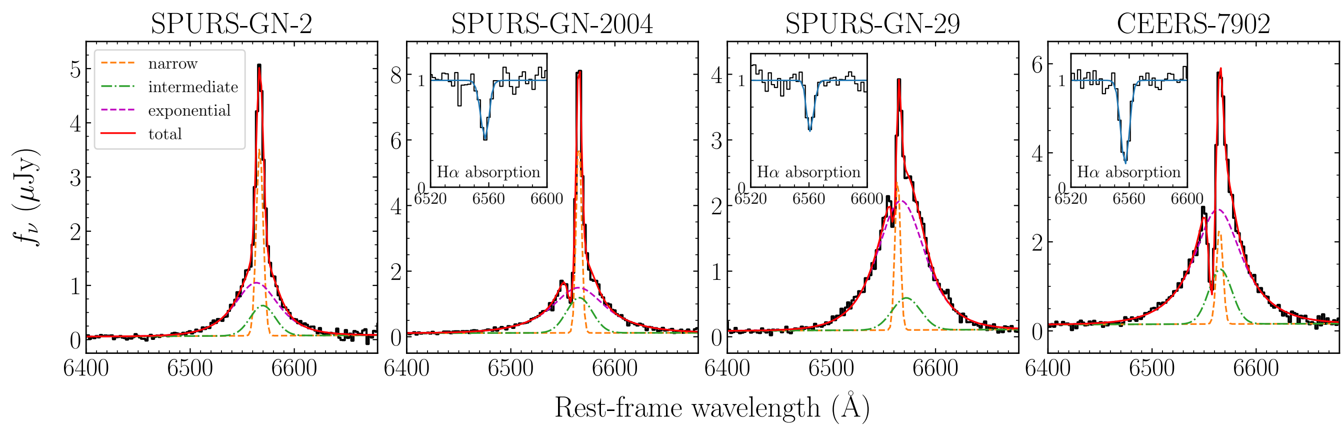

Figure B.2. Exponential model fits to the Hα emission line profiles of the four LRDs. The narrow emission component is shown as the orange dashed line. The intermediate component, which describes the unscattered BLR emission, is shown as green dash-dotted line. The broad exponential wing (convolution of intrinsic BLR emission with an exponential kernel) is shown as magenta dashed line. We also show the absorption components in the upper left corner of GN-2004, GN-29, and CEERS-7902. The total best-fit Hα line profiles are shown as red solid lines.

line profiles of the four LRDs ($\chi^2_\nu = 1.1 - 1.5$). With this model, the broad Hα lines have narrower FWHMs ($1180-1690$ km s^{-1}) than Gaussian fits. We derive that a large fraction ($76-88\%$) of the intrinsic BLR Hα emission experiences electron scattering. The total broad Hα EWs ($1181 - 1395$ Å) are similar to those derived from Gaussian fits. For narrow Hα emission lines, we find FWHMs ($275 - 356$ km s^{-1}) and EWs ($109 - 510$ Å) that are consistent with Gaussian fits (Table 2). The differences in BIC between exponential model fits and three-Gaussian model fits are very small (ΔBIC $= 1-3$), indicating that both models fit the Hα profiles equally well for the four LRDs.

C. METHODOLOGY OF DERIVING IONIZED GAS PROPERTIES

Using the narrow (FWHM $\simeq 330$ km s^{-1}) emission line detections in SPURS spectra, we derive the electron densities, temperatures, and chemical abundance ratios (O/H, N/O, N/C) of the ionized gas for the four LRDs. The derived narrow-line gas properties are presented in Table 5. Here we use the `Python` package `PyNeb` (V. Luridiana et al. 2015). The electron densities and temperatures are derived by jointly fitting the density-sensitive and temperature-sensitive line ratios. In each LRD, we derive the densities of the carbon, nitrogen, and silicon emitting gas with the available C III] λ1909/[C III] λ1907, N IV] λ1486/[N IV] λ1483, and Si III] λ1892/Si III] λ1883 ratios, respectively. For

Table B.1. Hα properties inferred from exponential model fits to the four LRDs.

Properties	SPURS-GN-2	SPURS-GN-2004	SPURS-GN-29	CEERS-7902
$\mathrm{FWHM_{narrow}}$ (km s^{-1})	356 ± 10	275 ± 7	276 ± 8	329 ± 7
$\mathrm{EW_{narrow}}$ (Å)	510 ± 19	335 ± 12	149 ± 32	109 ± 7
f	0.78 ± 0.12	0.76 ± 0.04	0.88 ± 0.15	0.83 ± 0.04
$\mathrm{FWHM_{int}}$ (km s^{-1})	1243 ± 211	1291 ± 87	1436 ± 330	1159 ± 95
$\mathrm{FWHM_{exp}}$ (km s^{-1})	1180 ± 95	1690 ± 74	1233 ± 70	1485 ± 59
$\mathrm{EW_{broad}}$ (Å)	1323 ± 185	1181 ± 67	1395 ± 277	1341 ± 89
$\mathrm{FWHM_{abs}}$ (km s^{-1})	–	355 ± 41	255 ± 15	333 ± 14
$\mathrm{EW_{abs}}$ (Å)	–	-93 ± 12	-106 ± 8	-146 ± 8
Δv_{abs} (km s^{-1})	–	-296 ± 50	-142 ± 48	-319 ± 48

NOTE—f is the fraction of intrinsic BLR emission being scattered. $\mathrm{FWHM_{int}}$ is the FWHM of the intermediate Gaussian which describes the intrinsic (unscattered) BLR emission. $\mathrm{FWHM_{exp}}$ is the FWHM of the broad exponential wing. $\mathrm{EW_{broad}}$ is the sum of the EWs of the intermediate component and the exponential wing, both contributed from the BLR emission.

temperature-sensitive line ratios we primarily focus on [O III] λ4363/[O III] λ5007, since both lines are close in wavelength and the ratio is less impacted by dust attenuation. We also derive temperatures using the O III] λ1666/[O III] λ5007 ratios.

We characterize the gas-phase oxygen abundances of the four LRDs following the methodology commonly used in recent LRD studies (e.g., Y. Isobe et al. 2025; G. P. Nikopoulos et al. 2026). The oxygen abundance O/H is estimated as the sum of O^{2+}/H and O^{+}/H. Based on the derived densities (inferred from C III] doublet ratios) and temperatures, we infer O^{2+}/H from the narrow [O III] λ5007/Hβ flux ratios. For the O^{+} zone, the temperature and density are likely different from those of the O^{2+} zone. Since we do not detect [O II] $\lambda\lambda$7320, 7330 auroral lines, we derive the O^{+} zone temperature following A. Campbell et al. (1986): $T(\mathrm{O^+}) = 0.7 \times T(\mathrm{O^{2+}}) + 3000$ K. For the O^{+} zone density, since we are not able to deblend the [O II] $\lambda\lambda$3727, 3729 doublet due to the resolution of the spectra and directly infer the density, we assume a typical value of the low-ionization zone ($n_\mathrm{e} \simeq 300$ cm^{-3}) derived in the literature (e.g., M. W. Topping et al. 2025a; R. L. Sanders et al. 2026). The singly ionized oxygen abundances (O^{+}/H) are inferred from the narrow [O II]/Hβ flux ratios based on the above O^{+} zone densities and temperatures.

We derive the nitrogen-to-oxygen abundance ratio following the similar procedures described in Z. Martinez et al. (2025). For the LRDs with both N IV] and N III] detections (GN-2, GN-29, CEERS-7902), we calculate the N/O ratios using (N^{3+}+N^{2+})/O^{2+} derived from (N IV]+N III])/O III] flux ratios. For GN-2004 whose N IV] is not available, we calculate N^{2+}/O^{2+} from the N III]/O III] ratio. To convert (N^{3+}+N^{2+})/O^{2+} or N^{2+}/O^{2+} to N/O abundance ratio, we apply an ionization correction factor (ICF) for each LRD. This step accounts for the contribution of ionic species that are not detected in the spectra (e.g., N^{+}, N^{2+} or N^{3+}). Following the equations presented in Z. Martinez et al. (2025), we compute the ICF for N/O as a function of metallicity and the N IV]/N III] (N43) ratio (or O32 ratio when N43 is not available). We also compute the nitrogen-to-carbon abundance ratios using the N IV] or N III] and C III] detections.

D. EMISSION LINES IN SPURS LRDS

D.1. *NUV Fe II Emission Line Measurements*

In Table D.1, we present the EWs of NUV Fe II emission lines of the four LRDs.

D.2. *Rest-frame optical spectra*

The full rest-frame optical spectra of the four LRDs are shown in Figure D.1. We present the optical emission line measurements (fluxes, EWs, FWHMs) in Table D.2. We also show the fits to the [O III] λ4959, λ5007 emission lines of the four LRDs in Figure D.2.

D.3. *Rest-frame UV Emission Lines of New SPURS LRDs*

In Figure D.3, we show the UV emission lines (N IV], N III], C III]) identified in the SPURS G140M spectra of LRDs listed in Table 7.

Table D.1. EW (Å) measurements of the NUV Fe II complexes.

	GN-2	GN-2004	GN-29	CEERS-7902
Fe II 2200–2660	202 ± 13	76 ± 8	40 ± 12	101 ± 14
Fe II UV62,63	70 ± 6	22 ± 2	13 ± 3	28 ± 5
Fe II UV61	44 ± 6	17 ± 2	5 ± 3	38 ± 6
Fe II UV60,78	28 ± 6	10 ± 2	7 ± 3	10 ± 6
Fe II (UV) 2200–3090	356 ± 24	141 ± 12	72 ± 16	194 ± 26
Fe II λ2508	9.4 ± 1.0	6.1 ± 1.0	2.9 ± 1.5	10.4 ± 1.5

NOTE—We report the rest-frame EWs of individual bands and the total value from $2200 - 3090$ Å, followed by the narrow Fe II λ2508 line.

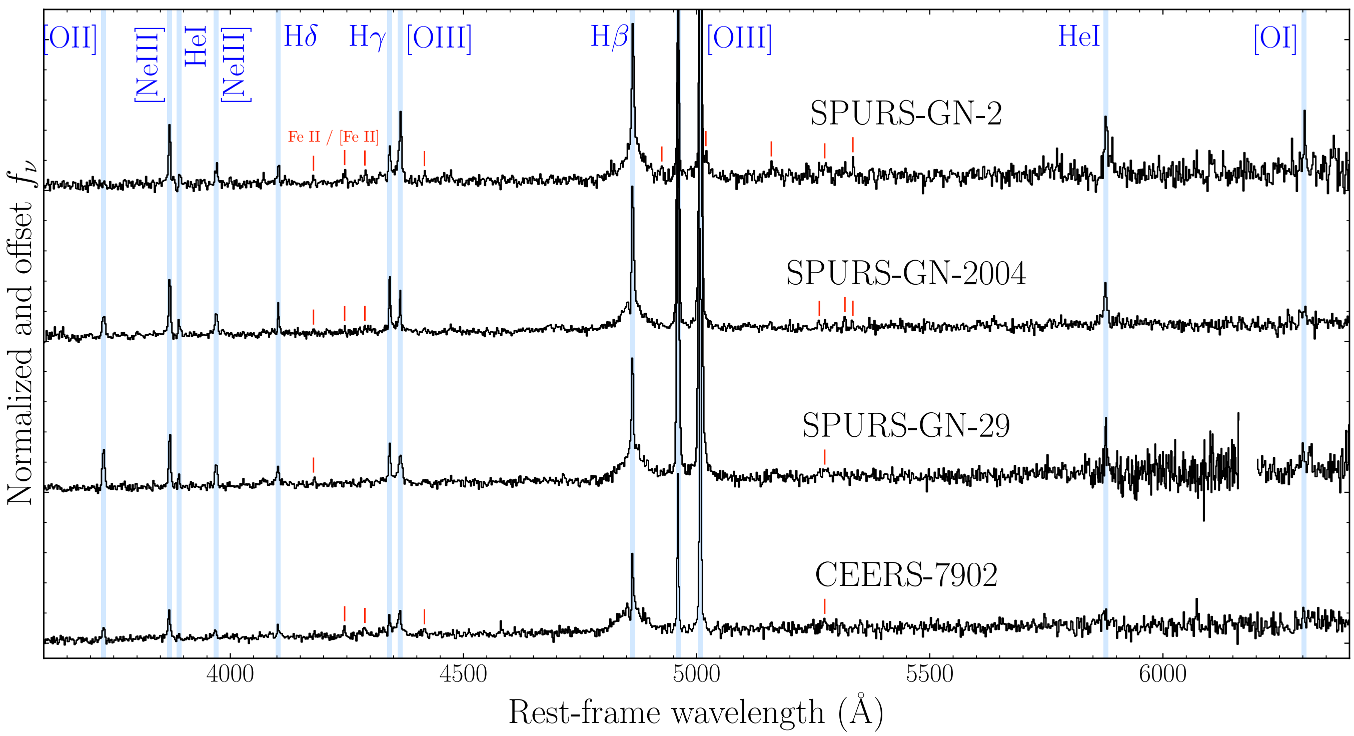

Figure D.1. SPURS rest-frame optical spectra of SPURS-GN-2, SPURS-GN-2004, SPURS-GN-29, and CEERS-7902. The figure is shown in the same way as Figure 4. We also mark the faint emission feature corresponding to Fe II or [Fe II] lines with red bars.

REFERENCES

Akins, H. B., Casey, C. M., Lambrides, E., et al. 2025, ApJ, 991, 37, doi: 10.3847/1538-4357/ade984

Ananna, T. T., Bogdán, Á., Kovács, O. E., Natarajan, P., & Hickox, R. C. 2024, ApJL, 969, L18, doi: 10.3847/2041-8213/ad5669

Ando, M., Harikane, Y., Katz, H., Inayoshi, K., & Tanaka, T. S. 2026, arXiv e-prints, arXiv:2606.03522, doi: 10.48550/arXiv.2606.03522

Asplund, M., Amarsi, A. M., & Grevesse, N. 2021, A&A, 653, A141, doi: 10.1051/0004-6361/202140445

Astropy Collaboration, Robitaille, T. P., Tollerud, E. J., et al. 2013, A&A, 558, A33, doi: 10.1051/0004-6361/201322068

Astropy Collaboration, Price-Whelan, A. M., Sipőcz, B. M., et al. 2018, AJ, 156, 123, doi: 10.3847/1538-3881/aabc4f

Astropy Collaboration, Price-Whelan, A. M., Lim, P. L., et al. 2022, ApJ, 935, 167, doi: 10.3847/1538-4357/ac7c74

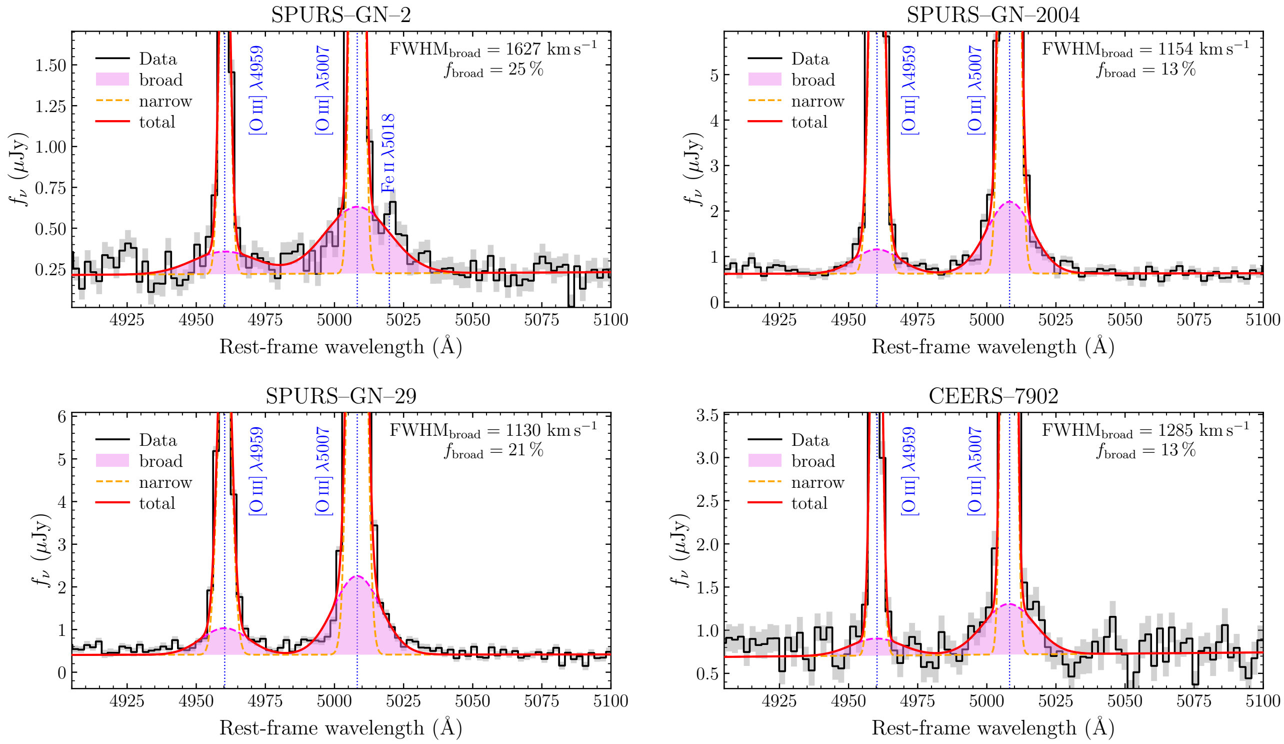

Figure D.2. [O III] $\lambda\lambda 4959, 5007$ emission lines of the four LRDs. We overplot the best-fit line profile to each spectrum (red), with the narrow components shown as orange dashed lines and the broad components as magenta shaded regions. The FWHM of the broad component (corrected for the instrumental resolution) and its contribution to the total [O III] line flux are quoted in each panel. A narrow Fe II $\lambda 5018$ line is marginally detected (2.8σ) on the red wing of [O III] $\lambda 5007$ in SPURS-GN-2, and adding it to the fit leaves the broad width unchanged and only slightly lowers the broad line fraction $f_{\rm broad}$ from 25% to 22%.

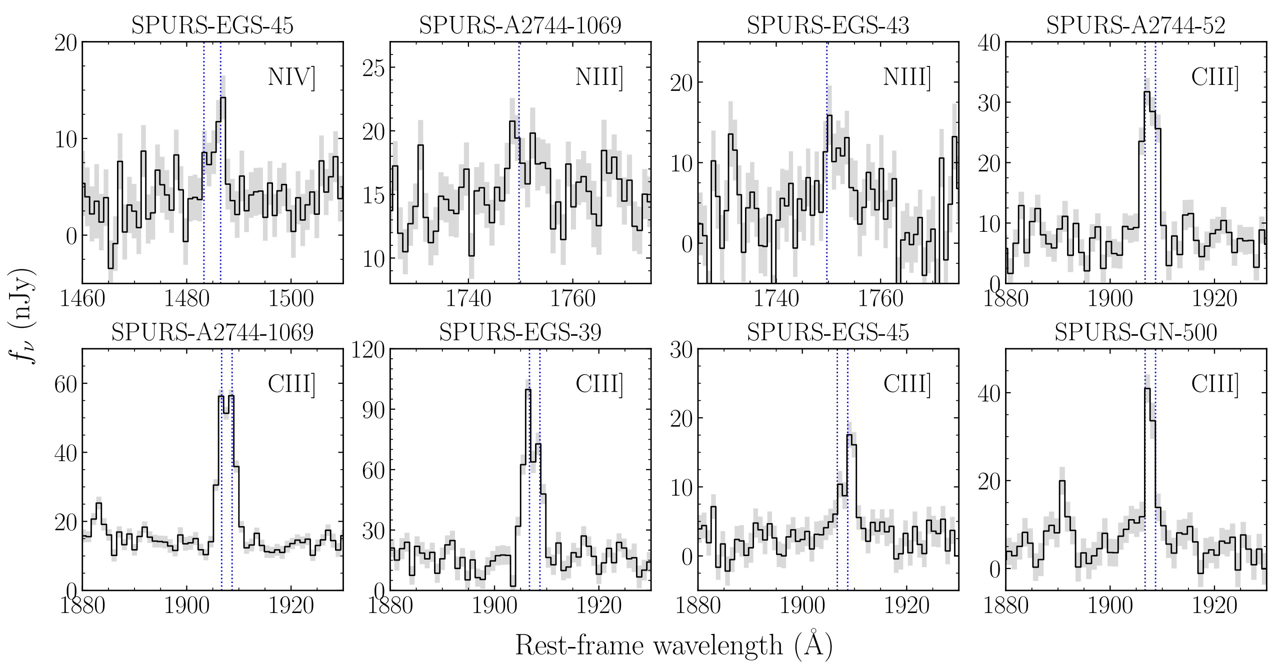

Figure D.3. N IV], N III], and C III] emission lines identified in SPURS G140M spectra of LRDs listed in Table 7.

Table D.2. Rest-frame optical emission line fluxes (10^{-19} erg s^{-1} cm^{-2}), EWs (Å), and FWHMs (km s^{-1}) of the four LRDs.

Line	SPURS-GN-2			SPURS-GN-2004			SPURS-GN-29			CEERS-7902		
	Flux	EW	FWHM	Flux	EW	FWHM	Flux	EW	FWHM	Flux	EW	FWHM
[O II] λ3728	2.5 ± 0.5	10.8 ± 2.2	363 ± 145	13.1 ± 1.2	22.8 ± 2.1	360 ± 24	18.6 ± 1.6	53.3 ± 4.6	380 ± 31	12.6 ± 2.7	34.3 ± 7.3	389 ± 80
[Ne III] λ3869	12.0 ± 0.8	43.7 ± 2.9	275 ± 13	26.6 ± 1.1	39.5 ± 1.7	273 ± 8	19.2 ± 1.4	48.4 ± 3.5	367 ± 19	21.5 ± 2.3	28.7 ± 3.1	457 ± 36
He I λ3890+H8	2.0 ± 0.9	7.7 ± 3.5	353 ± 123	6.8 ± 1.1	9.9 ± 1.6	266 ± 31	3.1 ± 1.0	7.8 ± 2.4	247 ± 59	1.4 ± 0.4	2.0 ± 0.5	244 ± 84
[Ne III] λ3968+Hϵ	4.7 ± 1.1	17.4 ± 3.9	467 ± 78	13.4 ± 1.4	18.1 ± 1.9	424 ± 33	9.5 ± 1.3	21.8 ± 3.1	448 ± 46	9.4 ± 0.9	13.3 ± 1.2	420 ± 65
H$\delta_{\rm total}$	3.1 ± 0.8	11.0 ± 2.9	–	9.2 ± 1.0	11.2 ± 1.2	–	7.9 ± 1.4	16.5 ± 2.9	–	21.3 ± 4.7	28.6 ± 6.4	–
H$\delta_{\rm narrow}$	3.1 ± 0.8	11.0 ± 2.9	296 ± 57	9.2 ± 1.0	11.2 ± 1.2	306 ± 17	7.9 ± 1.4	16.5 ± 2.9	469 ± 73	2.5 ± 0.7	3.4 ± 0.9	244 ± 31
H$\delta_{\rm broad}$	–	–	–	–	–	–	–	–	–	18.8 ± 4.7	25.2 ± 6.3	1974 ± 319
H$\gamma_{\rm total}$	17.9 ± 3.0	58.9 ± 9.8	–	44.6 ± 3.9	52.5 ± 4.6	–	24.0 ± 3.6	47.4 ± 7.0	–	38.9 ± 7.5	45.6 ± 8.8	–
H$\gamma_{\rm narrow}$	3.7 ± 0.8	12.2 ± 2.8	279 ± 47	16.6 ± 1.2	19.6 ± 1.4	306 ± 12	8.2 ± 0.9	16.2 ± 1.9	285 ± 24	5.6 ± 1.7	6.6 ± 2.0	244 ± 48
H$\gamma_{\rm broad}$	14.2 ± 2.9	46.7 ± 9.4	2745 ± 390	27.9 ± 3.7	32.9 ± 4.4	2375 ± 231	15.8 ± 3.4	31.2 ± 6.8	2781 ± 430	33.3 ± 7.3	39.0 ± 8.5	3083 ± 458
[O III] λ4363	11.5 ± 1.2	37.9 ± 4.0	427 ± 33	10.0 ± 1.0	11.8 ± 1.2	306 ± 16	10.8 ± 1.5	21.4 ± 3.0	476 ± 60	13.3 ± 2.7	15.5 ± 3.1	437 ± 67
H$\beta_{\rm total}$	61.3 ± 4.5	181 ± 13	–	139.4 ± 9.5	133 ± 9	–	91.0 ± 8.3	146 ± 13	–	146.2 ± 9.4	140 ± 9	–
H$\beta_{\rm narrow}$	17.6 ± 1.5	51.9 ± 4.4	337 ± 21	46.3 ± 3.3	44.3 ± 3.1	306 ± 16	20.3 ± 2.3	32.5 ± 3.8	274 ± 23	16.2 ± 1.9	15.5 ± 1.8	244 ± 3
H$\beta_{\rm broad}$	43.8 ± 4.2	129 ± 13	2955 ± 197	93.1 ± 8.9	89.1 ± 8.6	3125 ± 207	70.8 ± 7.9	113 ± 13	3357 ± 263	130.0 ± 9.2	125 ± 9	3982 ± 206
[O III] $\lambda4959_{\rm total}$	24.1 ± 0.4	74.1 ± 3.3	–	137.0 ± 1.1	139 ± 3	–	98.5 ± 1.8	159 ± 9	–	56.9 ± 0.9	52.9 ± 1.6	–
[O III] $\lambda4959_{\rm narrow}$	18.2 ± 0.4	55.7 ± 2.3	241 ± 5	119.6 ± 1.6	122 ± 3	315 ± 3	78.4 ± 6.3	126 ± 15	330 ± 16	49.9 ± 0.6	46.4 ± 1.2	236 ± 3
[O III] $\lambda4959_{\rm broad}$	6.0 ± 0.5	18.3 ± 1.8	1627 ± 181	17.3 ± 1.2	17.6 ± 1.2	1130 ± 117	20.1 ± 4.5	32.4 ± 6.2	1183 ± 306	7.0 ± 1.0	6.5 ± 1.0	1285 ± 135
[O III] $\lambda5007_{\rm total}$	70.5 ± 1.3	217 ± 9	–	400.4 ± 3.1	413 ± 9	–	287.9 ± 5.2	470 ± 24	–	166.4 ± 2.6	155 ± 4	–
[O III] $\lambda5007_{\rm narrow}$	53.1 ± 1.0	163 ± 6	241 ± 5	349.7 ± 4.6	361 ± 9	315 ± 3	229.2 ± 18.4	374 ± 42	330 ± 16	146.0 ± 1.8	136 ± 3	236 ± 3
[O III] $\lambda5007_{\rm broad}$	17.5 ± 1.3	53.6 ± 5.1	1627 ± 181	50.7 ± 3.6	52.3 ± 3.7	1130 ± 117	58.7 ± 13.3	95.9 ± 18.8	1183 ± 306	20.4 ± 2.9	19.0 ± 2.8	1285 ± 135
He I λ5876	10.6 ± 0.8	34.6 ± 2.8	432 ± 51	18.8 ± 1.4	22.9 ± 1.7	392 ± 45	8.4 ± 1.4	15.2 ± 2.5	360 ± 90	19.1 ± 3.4	19.0 ± 3.4	1531 ± 469
[O I] λ6302	3.9 ± 0.8	12.6 ± 2.6	281 ± 37	8.5 ± 1.4	10.9 ± 1.7	665 ± 181	5.2 ± 1.2	9.4 ± 2.1	343 ± 99	< 4.9	< 5.1	–

Note—For non-detections, 3σ upper limits of line fluxes and EWs are provided.

Baggen, J. F. W., Scoggins, M. T., van Dokkum, P., et al. 2026, ApJL, 1002, L4, doi: 10.3847/2041-8213/ae58a5

Bahcall, J. N., & Wolf, R. A. 1968, ApJ, 152, 701, doi: 10.1086/149589

Barkana, R. 2002, NewA, 7, 85, doi: 10.1016/S1384-1076(01)00091-4

Barro, G., Pérez-González, P. G., Kocevski, D. D., et al. 2024, ApJ, 963, 128, doi: 10.3847/1538-4357/ad167e

Barth, A. J., Pancoast, A., Bennert, V. N., et al. 2013, ApJ, 769, 128, doi: 10.1088/0004-637X/769/2/128

Bastian, N., & Lardo, C. 2018, Annual Review of Astronomy and Astrophysics, vol. 56, p.83-136, 56, 83, doi: 10.1146/annurev-astro-081817-051839

Berg, D. A., Chisholm, J., Erb, D. K., et al. 2019, ApJL, 878, L3, doi: 10.3847/2041-8213/ab21dc

Böker, T., Beck, T. L., Birkmann, S. M., et al. 2023, PASP, 135, 038001, doi: 10.1088/1538-3873/acb846

Brammer, G. 2023, msaexp: NIRSpec analyis tools, 0.6.17 Zenodo, doi: 10.5281/zenodo.8319596

Brazzini, M., D'Eugenio, F., Maiolino, R., et al. 2025, MNRAS, 544, L167, doi: 10.1093/mnrasl/slaf116

Brazzini, M., D'Eugenio, F., Maiolino, R., et al. 2026, arXiv e-prints, arXiv:2601.22214, doi: 10.48550/arXiv.2601.22214

Brinchmann, J., Pettini, M., & Charlot, S. 2008, MNRAS, 385, 769, doi: 10.1111/j.1365-2966.2008.12914.x

Brotherton, M. S., Tran, H. D., Becker, R. H., et al. 2001, ApJ, 546, 775, doi: 10.1086/318309

Bunker, A. J., Saxena, A., Cameron, A. J., et al. 2023, A&A, 677, A88, doi: 10.1051/0004-6361/202346159

Bushouse, H., Eisenhamer, J., Dencheva, N., et al. 2024, JWST Calibration Pipeline, 1.16.1 Zenodo, doi: 10.5281/zenodo.14153298

Cameron, A. J., Katz, H., Witten, C., et al. 2024, MNRAS, 534, 523, doi: 10.1093/mnras/stae1547

Cameron, A. J., Saxena, A., Bunker, A. J., et al. 2023, A&A, 677, A115, doi: 10.1051/0004-6361/202346107

Campbell, A., Terlevich, R., & Melnick, J. 1986, MNRAS, 223, 811, doi: 10.1093/mnras/223.4.811

Cardelli, J. A., Clayton, G. C., & Mathis, J. S. 1989, ApJ, 345, 245, doi: 10.1086/167900

Castellano, M., Napolitano, L., Fontana, A., et al. 2024, ApJ, 972, 143, doi: 10.3847/1538-4357/ad5f88

Chandar, R., Leitherer, C., & Tremonti, C. A. 2004, ApJ, 604, 153, doi: 10.1086/381723

Chang, S.-J., & Gronke, M. 2024, MNRAS, 532, 3526, doi: 10.1093/mnras/stae1664

Charbonnel, C., Schaerer, D., Prantzos, N., et al. 2023, A&A, 673, L7, doi: 10.1051/0004-6361/202346410

Chen, Z., Stark, D. P., Mason, C. A., et al. 2026a, arXiv e-prints, arXiv:2608.12699, doi: 10.48550/arXiv.2608.12699

Chen, Z., Stark, D. P., Mason, C. A., et al. 2026b, arXiv e-prints, arXiv:2604.21516, doi: 10.48550/arXiv.2604.21516

Chevallard, J., & Charlot, S. 2016, MNRAS, 462, 1415, doi: 10.1093/mnras/stw1756

Chisholm, J., Prochaska, J. X., Schaerer, D., Gazagnes, S., & Henry, A. 2020, MNRAS, 498, 2554, doi: 10.1093/mnras/staa2470

Chisholm, J., Rigby, J. R., Bayliss, M., et al. 2019, ApJ, 882, 182, doi: 10.3847/1538-4357/ab3104

Chisholm, J., Tremonti, C. A., Leitherer, C., et al. 2015, ApJ, 811, 149, doi: 10.1088/0004-637X/811/2/149

Chisholm, J., Berg, D. A., Boylan-Kolchin, M., et al. 2026, ApJL, 1004, L4, doi: 10.3847/2041-8213/ae6dae

Choe, S., Emil Rivera-Thorsen, T., Dahle, H., et al. 2025, A&A, 698, A16, doi: 10.1051/0004-6361/202450685

Chon, S., & Omukai, K. 2025, MNRAS, 539, 2561, doi: 10.1093/mnras/staf598

Clavel, J., Reichert, G. A., Alloin, D., et al. 1991, ApJ, 366, 64, doi: 10.1086/169540

Cloonan, A. P., Whitaker, K. E., Manning, S. M., et al. 2026, arXiv e-prints, arXiv:2603.24700, doi: 10.48550/arXiv.2603.24700

Crowther, P. A. 2007, ARA&A, 45, 177, doi: 10.1146/annurev.astro.45.051806.110615

Crowther, P. A., Caballero-Nieves, S. M., Bostroem, K. A., et al. 2016, Monthly Notices of the Royal Astronomical Society, 458, 624, doi: 10.1093/mnras/stw273

Curtis-Lake, E., Cameron, A. J., Bunker, A. J., et al. 2026, MNRAS, 549, stag836, doi: 10.1093/mnras/stag836

Davidson, K., Ebbets, D., Weigelt, G., et al. 1995, AJ, 109, 1784, doi: 10.1086/117408

de Graaff, A., Rix, H.-W., Naidu, R. P., et al. 2025a, A&A, 701, A168, doi: 10.1051/0004-6361/202554681

de Graaff, A., Hviding, R. E., Naidu, R. P., et al. 2025b, arXiv e-prints, arXiv:2511.21820, doi: 10.48550/arXiv.2511.21820

de Graaff, A., Brammer, G., Weibel, A., et al. 2025c, A&A, 697, A189, doi: 10.1051/0004-6361/202452186

D'Eugenio, F., Nelson, E., Ji, X., et al. 2025, arXiv e-prints, arXiv:2510.00101, doi: 10.48550/arXiv.2510.00101

D'Eugenio, F., Maiolino, R., Perna, M., et al. 2026, MNRAS, 547, stag401, doi: 10.1093/mnras/stag401

Eisenstein, D. J., Willott, C., Alberts, S., et al. 2026, ApJS, 283, 6, doi: 10.3847/1538-4365/ae3163

Endsley, R., Chisholm, J., Stark, D. P., Topping, M. W., & Whitler, L. 2025, ApJ, 987, 189, doi: 10.3847/1538-4357/addc74

Erb, D. K., Quider, A. M., Henry, A. L., & Martin, C. L. 2012, ApJ, 759, 26, doi: 10.1088/0004-637X/759/1/26

Feltre, A., Charlot, S., & Gutkin, J. 2016, MNRAS, 456, 3354, doi: 10.1093/mnras/stv2794

Finkelstein, S. L., Bagley, M. B., Arrabal Haro, P., et al. 2025, ApJL, 983, L4, doi: 10.3847/2041-8213/adbbd3

Flower, D. R., Nussbaumer, H., & Schild, H. 1979, A&A, 72, L1

Foreman-Mackey, D., Hogg, D. W., Lang, D., & Goodman, J. 2013, \pasp, 125, 306, doi: 10.1086/670067

Francis, P. J., Hewett, P. C., Foltz, C. B., et al. 1991, ApJ, 373, 465, doi: 10.1086/170066

Froese Fischer, C., & Saha, H. P. 1985, PhyS, 32, 181, doi: 10.1088/0031-8949/32/3/004

Fujii, M. S., Wang, L., Tanikawa, A., Hirai, Y., & Saitoh, T. R. 2024, Science, 384, 1488, doi: 10.1126/science.adi4211

Furtak, L. J., Zitrin, A., Plat, A., et al. 2023, ApJ, 952, 142, doi: 10.3847/1538-4357/acdc9d

Gardner, J. P., Mather, J. C., Abbott, R., et al. 2023, PASP, 135, 068001, doi: 10.1088/1538-3873/acd1b5

Geris, S., Maiolino, R., Ji, X., et al. 2026, arXiv e-prints, arXiv:2606.21614, doi: 10.48550/arXiv.2606.21614

Gibson, R. R., Jiang, L., Brandt, W. N., et al. 2009, ApJ, 692, 758, doi: 10.1088/0004-637X/692/1/758

Gieles, M., Padoan, P., Charbonnel, C., Vink, J. S., & Ramírez-Galeano, L. 2025, MNRAS, 544, 483, doi: 10.1093/mnras/staf1314

Glazer, K. S., Jones, T., Chen, Y., et al. 2025, ApJ, 992, 191, doi: 10.3847/1538-4357/ae0194

Gordon, K. D., Clayton, G. C., Misselt, K. A., Landolt, A. U., & Wolff, M. J. 2003, ApJ, 594, 279, doi: 10.1086/376774

Gräfener, G. 2021, A&A, 647, A13, doi: 10.1051/0004-6361/202040037

Greene, J. E., & Ho, L. C. 2005, ApJ, 630, 122, doi: 10.1086/431897

Greene, J. E., Labbe, I., Goulding, A. D., et al. 2024, ApJ, 964, 39, doi: 10.3847/1538-4357/ad1e5f

Gutkin, J., Charlot, S., & Bruzual, G. 2016, MNRAS, 462, 1757, doi: 10.1093/mnras/stw1716

Habing, H. J. 1968, BAN, 19, 421

Hainline, K. N., Maiolino, R., Juodžbalis, I., et al. 2025, ApJ, 979, 138, doi: 10.3847/1538-4357/ad9920

Hamann, F. 2012, in Astrophysics and Space Science Library, Vol. 384, Eta Carinae and the Supernova Impostors, ed. K. Davidson & R. M. Humphreys, 95, doi: 10.1007/978-1-4614-2275-4_5

Hamann, W.-R., Leuenhagen, U., Koesterke, L., & Wessolowski, U. 1992, A&A, 255, 200

Harikane, Y., Zhang, Y., Nakajima, K., et al. 2023, ApJ, 959, 39, doi: 10.3847/1538-4357/ad029e

Harris, C. R., Millman, K. J., van der Walt, S. J., et al. 2020, Nature, 585, 357, doi: 10.1038/s41586-020-2649-2

Hayes, M. 2015, PASA, 32, e027, doi: 10.1017/pasa.2015.25

Heintz, K. E., Watson, D., Brammer, G., et al. 2024, Science, 384, 890, doi: 10.1126/science.adj0343

Heintz, K. E., Brammer, G. B., Watson, D., et al. 2025, A&A, 693, A60, doi: 10.1051/0004-6361/202450243

Henry, A., Berg, D. A., Scarlata, C., Verhamme, A., & Erb, D. 2018, ApJ, 855, 96, doi: 10.3847/1538-4357/aab099

Henry, A., Scarlata, C., Martin, C. L., & Erb, D. 2015, ApJ, 809, 19, doi: 10.1088/0004-637X/809/1/19

Higgins, E. R., Vink, J. S., Hirschi, R., Laird, A. M., & Sabhahit, G. 2025, A&A, 699, A71, doi: 10.1051/0004-6361/202453472

Higgins, E. R., Vink, J. S., Hirschi, R., Laird, A. M., & Sabhahit, G. N. 2023, MNRAS, 526, 534, doi: 10.1093/mnras/stad2537

Hillier, D. J. 1989, ApJ, 347, 392, doi: 10.1086/168127

Horne, K. 1986, PASP, 98, 609, doi: 10.1086/131801

Howk, J. C., & Sembach, K. R. 1999, ApJL, 523, L141, doi: 10.1086/312284

Hunter, J. D. 2007, Computing in Science and Engineering, 9, 90, doi: 10.1109/MCSE.2007.55

Hviding, R. E., de Graaff, A., Miller, T. B., et al. 2025, A&A, 702, A57, doi: 10.1051/0004-6361/202555816

Ilić, D., Rakić, N., & Popović, L. Č. 2023, ApJS, 267, 19, doi: 10.3847/1538-4365/acd783

Inayoshi, K., & Maiolino, R. 2025, ApJL, 980, L27, doi: 10.3847/2041-8213/adaebd

Inayoshi, K., Murase, K., & Kashiyama, K. 2026, ApJ, 1000, 90, doi: 10.3847/1538-4357/ae42ce

Ishikawa, Y., Eilers, A.-C., Naidu, R. P., et al. 2026, arXiv e-prints, arXiv:2607.09647, doi: 10.48550/arXiv.2607.09647

Isobe, Y., Maiolino, R., D'Eugenio, F., et al. 2025, MNRAS, 541, L71, doi: 10.1093/mnrasl/slaf056

Jakobsen, P., Ferruit, P., Alves de Oliveira, C., et al. 2022, A&A, 661, A80, doi: 10.1051/0004-6361/202142663

James, B. L., Aloisi, A., Heckman, T., Sohn, S. T., & Wolfe, M. A. 2014, ApJ, 795, 109, doi: 10.1088/0004-637X/795/2/109

Jaskot, A. E., & Ravindranath, S. 2016, ApJ, 833, 136, doi: 10.3847/1538-4357/833/2/136
Jenkins, E. B. 2009, ApJ, 700, 1299, doi: 10.1088/0004-637X/700/2/1299
Ji, X., Maiolino, R., Übler, H., et al. 2025, MNRAS, 544, 3900, doi: 10.1093/mnras/staf1867
Ji, X., D'Eugenio, F., Juodžbalis, I., et al. 2026a, MNRAS, 545, staf2235, doi: 10.1093/mnras/staf2235
Ji, X., Pezzulli, G., D'Eugenio, F., et al. 2026b, arXiv e-prints, arXiv:2604.03370, doi: 10.48550/arXiv.2604.03370
Jiang, Y.-F., Stone, J. M., & Davis, S. W. 2014, ApJ, 796, 106, doi: 10.1088/0004-637X/796/2/106
Jiang, Y.-F., Stone, J. M., & Davis, S. W. 2019, ApJ, 880, 67, doi: 10.3847/1538-4357/ab29ff
Johansson, S., & Hamann, F. W. 1993, Physica Scripta Volume T, 47, 157, doi: 10.1088/0031-8949/1993/T47/025
Johansson, S., & Jordan, C. 1984, MNRAS, 210, 239, doi: 10.1093/mnras/210.2.239
Johansson, S., & Letokhov, V. S. 2001, A&A, 378, 266, doi: 10.1051/0004-6361:20011062
Johansson, S., Zethson, T., Hartman, H., et al. 2000, A&A, 361, 977
Jones, G. C., Bunker, A. J., Saxena, A., et al. 2025, MNRAS, 536, 2355, doi: 10.1093/mnras/stae2670
Jones, T., Stark, D. P., & Ellis, R. S. 2012, ApJ, 751, 51, doi: 10.1088/0004-637X/751/1/51
Jones, T., Stark, D. P., & Ellis, R. S. 2018, ApJ, 863, 191, doi: 10.3847/1538-4357/aad37f
Jones, T. A., Ellis, R. S., Schenker, M. A., & Stark, D. P. 2013, ApJ, 779, 52, doi: 10.1088/0004-637X/779/1/52
Juodžbalis, I., Ji, X., Maiolino, R., et al. 2024, MNRAS, 535, 853, doi: 10.1093/mnras/stae2367
Juodžbalis, I., Marconcini, C., D'Eugenio, F., et al. 2026a, Nature, 653, 1017, doi: 10.1038/s41586-026-10579-4
Juodžbalis, I., Ji, X., D'Eugenio, F., et al. 2026b, arXiv e-prints, arXiv:2607.19057, doi: 10.48550/arXiv.2607.19057
Kageura, Y., Ouchi, M., Yanagisawa, H., et al. 2026, arXiv e-prints, arXiv:2608.14534, doi: 10.48550/arXiv.2608.14534
Keerthi Vasan, G. C., Jones, T., Sanders, R. L., et al. 2023, ApJ, 959, 124, doi: 10.3847/1538-4357/acf462
Keerthi Vasan G., C., Senchyna, P., Mason, C. A., et al. 2026, arXiv e-prints, arXiv:2606.06609, doi: 10.48550/arXiv.2606.06609
Killi, M., Watson, D., Brammer, G., et al. 2024, A&A, 691, A52, doi: 10.1051/0004-6361/202348857
Kobayashi, C., & Ferrara, A. 2024, ApJL, 962, L6, doi: 10.3847/2041-8213/ad1de1
Kocevski, D. D., Onoue, M., Inayoshi, K., et al. 2023, ApJL, 954, L4, doi: 10.3847/2041-8213/ace5a0
Kocevski, D. D., Finkelstein, S. L., Barro, G., et al. 2025, ApJ, 986, 126, doi: 10.3847/1538-4357/adbc7d
Kocevski, D. D., Taylor, A. J., Onoue, M., et al. 2026, arXiv e-prints, arXiv:2609.00112, doi: 10.48550/arXiv.2609.00112
Kokorev, V., Caputi, K. I., Greene, J. E., et al. 2024, ApJ, 968, 38, doi: 10.3847/1538-4357/ad4265
Kokorev, V., Chisholm, J., Naidu, R. P., et al. 2026, ApJ, 1004, 153, doi: 10.3847/1538-4357/ae4ed7
Konstantopoulou, C., De Cia, A., Krogager, J.-K., et al. 2022, A&A, 666, A12, doi: 10.1051/0004-6361/202243994
Kornei, K. A., Shapley, A. E., Martin, C. L., et al. 2013, ApJ, 774, 50, doi: 10.1088/0004-637X/774/1/50
Kwan, J., & Krolik, J. H. 1981, ApJ, 250, 478, doi: 10.1086/159395
Labbé, I., van Dokkum, P., Nelson, E., et al. 2023, Nature, 616, 266, doi: 10.1038/s41586-023-05786-2
Labbé, I., Greene, J. E., Matthee, J., et al. 2024, arXiv e-prints, arXiv:2412.04557, doi: 10.48550/arXiv.2412.04557
Labbé, I., Greene, J. E., Bezanson, R., et al. 2025, ApJ, 978, 92, doi: 10.3847/1538-4357/ad3551
Lambrides, E., Larson, R. L., Garofali, K., et al. 2026, Nature Astronomy, 10, 868, doi: 10.1038/s41550-026-02813-w
Larson, R. L., Finkelstein, S. L., Kocevski, D. D., et al. 2023, ApJL, 953, L29, doi: 10.3847/2041-8213/ace619
Leethochawalit, N., Jones, T. A., Ellis, R. S., Stark, D. P., & Zitrin, A. 2016, ApJ, 831, 152, doi: 10.3847/0004-637X/831/2/152
Leighly, K. M., & Moore, J. R. 2004, ApJ, 611, 107, doi: 10.1086/422088
Leitherer, C., Ortiz Otálvaro, P. A., Bresolin, F., et al. 2010, ApJS, 189, 309, doi: 10.1088/0067-0049/189/2/309
Leitherer, C., Tremonti, C. A., Heckman, T. M., & Calzetti, D. 2011, AJ, 141, 37, doi: 10.1088/0004-6256/141/2/37
Leung, G. C. K., Finkelstein, S. L., Pérez-González, P. G., et al. 2025, ApJ, 992, 26, doi: 10.3847/1538-4357/adfcce
Liddle, A. R. 2007, MNRAS, 377, L74, doi: 10.1111/j.1745-3933.2007.00306.x
Lin, X., Wang, F., Fan, X., et al. 2024, ApJ, 974, 147, doi: 10.3847/1538-4357/ad6565
Liu, H., Jiang, Y.-F., Quataert, E., Greene, J. E., & Ma, Y. 2025, ApJ, 994, 113, doi: 10.3847/1538-4357/ae0c19
Luridiana, V., Morisset, C., & Shaw, R. A. 2015, A&A, 573, A42, doi: 10.1051/0004-6361/201323152

Madau, P., & Maiolino, R. 2026, arXiv e-prints, arXiv:2602.22386, doi: 10.48550/arXiv.2602.22386
Mainali, R., Stark, D. P., Tang, M., et al. 2020, MNRAS, 494, 719, doi: 10.1093/mnras/staa751
Maiolino, R., Scholtz, J., Curtis-Lake, E., et al. 2024a, A&A, 691, A145, doi: 10.1051/0004-6361/202347640
Maiolino, R., Scholtz, J., Witstok, J., et al. 2024b, Nature, 627, 59, doi: 10.1038/s41586-024-07052-5
Maiolino, R., Risaliti, G., Signorini, M., et al. 2025, MNRAS, 538, 1921, doi: 10.1093/mnras/staf359
Marques-Chaves, R., Martins, F., Schaerer, D., Dessauges-Zavadsky, M., & Palacios, A. 2026, A&A, 711, L3, doi: 10.1051/0004-6361/202660493
Marques-Chaves, R., Schaerer, D., Kuruvanthodi, A., et al. 2024, A&A, 681, A30, doi: 10.1051/0004-6361/202347411
Martinez, Z., Berg, D. A., James, B. L., et al. 2025, ApJ, 995, 204, doi: 10.3847/1538-4357/ae17c6
Martins, F., Palacios, A., Schaerer, D., & Marques-Chaves, R. 2025, A&A, 698, A262, doi: 10.1051/0004-6361/202554421
Martins, F., Schaerer, D., Marques-Chaves, R., & Upadhyaya, A. 2023, Astronomy and Astrophysics, 678, A159, doi: 10.1051/0004-6361/202346732
Mascia, S., Matthee, J., Torralba, A., et al. 2026, arXiv e-prints, arXiv:2608.25021, doi: 10.48550/arXiv.2608.25021
Mason, C. A., Chen, Z., Stark, D. P., et al. 2026, A&A, 705, A114, doi: 10.1051/0004-6361/202553820
Matsuoka, Y., Oyabu, S., Tsuzuki, Y., & Kawara, K. 2007, ApJ, 663, 781, doi: 10.1086/518399
Matthee, J., Naidu, R. P., Brammer, G., et al. 2024, ApJ, 963, 129, doi: 10.3847/1538-4357/ad2345
Matthee, J., Torralba, A., Pezzulli, G., et al. 2026, arXiv e-prints, arXiv:2603.17667, doi: 10.48550/arXiv.2603.17667
Mayer, L., van Donkelaar, F., Messa, M., Capelo, P. R., & Adamo, A. 2025, ApJL, 981, L28, doi: 10.3847/2041-8213/adadfe
McClymont, W., Tacchella, S., Smith, A., et al. 2026, MNRAS, 548, stag016, doi: 10.1093/mnras/stag016
Mesinger, A., & Furlanetto, S. R. 2008, MNRAS, 385, 1348, doi: 10.1111/j.1365-2966.2007.12836.x
Meyer, R. A., Oesch, P. A., Giovinazzo, E., et al. 2024, MNRAS, 535, 1067, doi: 10.1093/mnras/stae2353
Mignoli, M., Feltre, A., Bongiorno, A., et al. 2019, A&A, 626, A9, doi: 10.1051/0004-6361/201935062
Miralda-Escudé, J. 1998, ApJ, 501, 15, doi: 10.1086/305799
Mockler, B., Gallegos-Garcia, M., Götberg, Y., Miller, J. M., & Ramirez-Ruiz, E. 2024, ApJL, 973, L9, doi: 10.3847/2041-8213/ad6c34
Morishita, T., Stiavelli, M., Mason, C. A., et al. 2026, ApJ, 998, 175, doi: 10.3847/1538-4357/ae3a7c
Morton, D. C. 1991, ApJS, 77, 119, doi: 10.1086/191601
Murray, N., Chiang, J., Grossman, S. A., & Voit, G. M. 1995, ApJ, 451, 498, doi: 10.1086/176238
Naidu, R. P., Matthee, J., Katz, H., et al. 2026, Nature, 656, 329, doi: 10.1038/s41586-026-10846-4
Nakajima, K., Schaerer, D., Le Fèvre, O., et al. 2018, A&A, 612, A94, doi: 10.1051/0004-6361/201731935
Nakane, M., & Ouchi, M. 2026, arXiv e-prints, arXiv:2608.12466, doi: 10.48550/arXiv.2608.12466
Nanayakkara, T., Brinchmann, J., Boogaard, L., et al. 2019, A&A, 624, A89, doi: 10.1051/0004-6361/201834565
Nandal, D., Whalen, D. J., Latif, M. A., & Heger, A. 2025, ApJL, 994, L11, doi: 10.3847/2041-8213/ae1a63
Navarro-Carrera, R., Caputi, K. I., Iani, E., et al. 2025, ApJ, 993, 194, doi: 10.3847/1538-4357/adca35
Netzer, H. 1980, ApJ, 236, 406, doi: 10.1086/157757
Neufeld, D. A. 1990, ApJ, 350, 216, doi: 10.1086/168375
Niedzielski, A., & Rochowicz, K. 1994, A&AS, 108, 669
Nikopoulos, G. P., Watson, D., Pollock, C. L., et al. 2026, arXiv e-prints, arXiv:2606.31515, doi: 10.48550/arXiv.2606.31515
Nomoto, K., Tominaga, N., Umeda, H., Kobayashi, C., & Maeda, K. 2006, NuPhA, 777, 424, doi: 10.1016/j.nuclphysa.2006.05.008
Oesch, P. A., Brammer, G., Naidu, R. P., et al. 2023, MNRAS, 525, 2864, doi: 10.1093/mnras/stad2411
Oke, J. B., & Gunn, J. E. 1983, ApJ, 266, 713, doi: 10.1086/160817
Osterbrock, D. E., & Ferland, G. J. 2006, Astrophysics of gaseous nebulae and active galactic nuclei
Pacucci, F., & Urry, C. M. 2026, arXiv e-prints, arXiv:2608.23671, doi: 10.48550/arXiv.2608.23671
Pahl, A. J., Shapley, A., Faisst, A. L., et al. 2020, MNRAS, 493, 3194, doi: 10.1093/mnras/staa355
Papovich, C., Ronayne, K., Hu, W., et al. 2026, arXiv e-prints, arXiv:2608.04101, doi: 10.48550/arXiv.2608.04101
Parker, K. S., Berg, D. A., Gazagnes, S., et al. 2024, ApJ, 977, 104, doi: 10.3847/1538-4357/ad87cd
Pascale, M., & Dai, L. 2024, ApJ, 976, 166, doi: 10.3847/1538-4357/ad7732
Pasha, I., & Miller, T. B. 2023, The Journal of Open Source Software, 8, 5703, doi: 10.21105/joss.05703
Pérez-González, P. G., Barro, G., Rieke, G. H., et al. 2024, ApJ, 968, 4, doi: 10.3847/1538-4357/ad38bb
Pérez-González, P. G., Barro, G., Carniani, S., et al. 2026, arXiv e-prints, arXiv:2602.20247, doi: 10.48550/arXiv.2602.20247

Pettini, M., Rix, S. A., Steidel, C. C., et al. 2002, ApJ, 569, 742, doi: 10.1086/339355

Portegies Zwart, S. F., & McMillan, S. L. W. 2002, ApJ, 576, 899, doi: 10.1086/341798

Prantzos, N., Charbonnel, C., & Iliadis, C. 2007, A&A, 470, 179, doi: 10.1051/0004-6361:20077205

Prochaska, J. X., Chen, H.-W., & Bloom, J. S. 2006, ApJ, 648, 95, doi: 10.1086/505737

Prochaska, J. X., Kasen, D., & Rubin, K. 2011, ApJ, 734, 24, doi: 10.1088/0004-637X/734/1/24

Quider, A. M., Pettini, M., Shapley, A. E., & Steidel, C. C. 2009, MNRAS, 398, 1263, doi: 10.1111/j.1365-2966.2009.15234.x

Raiter, A., Schaerer, D., & Fosbury, R. A. E. 2010, A&A, 523, A64, doi: 10.1051/0004-6361/201015236

Rantala, A., Lahén, N., Naab, T., Escobar, G. J., & Iorio, G. 2025, MNRAS, 543, 2130, doi: 10.1093/mnras/staf1519

Rantala, A., Naab, T., & Lahén, N. 2024, MNRAS, 531, 3770, doi: 10.1093/mnras/stae1413

Rantala, A., Naab, T., Lahén, N., et al. 2026, MNRAS, 549, stag986, doi: 10.1093/mnras/stag986

Reines, A. E., & Volonteri, M. 2015, ApJ, 813, 82, doi: 10.1088/0004-637X/813/2/82

Rieke, M. J., Kelly, D. M., Misselt, K., et al. 2023, PASP, 135, 028001, doi: 10.1088/1538-3873/acac53

Rigby, J., Perrin, M., McElwain, M., et al. 2023, PASP, 135, 048001, doi: 10.1088/1538-3873/acb293

Rinaldi, P., Bonaventura, N., Rieke, G. H., et al. 2025, ApJ, 992, 71, doi: 10.3847/1538-4357/adfa10

Rix, S. A., Pettini, M., Leitherer, C., et al. 2004, ApJ, 615, 98, doi: 10.1086/424031

Roberts-Borsani, G., Treu, T., Shapley, A., et al. 2024, ApJ, 976, 193, doi: 10.3847/1538-4357/ad85d3

Robertson, B. E., Johnson, B. D., Tacchella, S., et al. 2026, arXiv e-prints, arXiv:2601.15956, doi: 10.48550/arXiv.2601.15956

Runco, J. N., Shapley, A. E., Sanders, R. L., et al. 2021, Monthly Notices of the Royal Astronomical Society, 502, 2600, doi: 10.1093/mnras/stab119

Rusakov, V., Watson, D., Nikopoulos, G. P., et al. 2026, Nature, 649, 574, doi: 10.1038/s41586-025-09900-4

Saldana-Lopez, A., Schaerer, D., Chisholm, J., et al. 2023, MNRAS, 522, 6295, doi: 10.1093/mnras/stad1283

Sanders, R. L., Shapley, A. E., Reddy, N. A., et al. 2020, MNRAS, 491, 1427, doi: 10.1093/mnras/stz3032

Sanders, R. L., Shapley, A. E., Topping, M. W., et al. 2026, ApJ, 1003, 228, doi: 10.3847/1538-4357/ae66e2

Savage, B. D., & Sembach, K. R. 1991, ApJ, 379, 245, doi: 10.1086/170498

Schaerer, D. 1996, A&A, 309, 129, doi: 10.48550/arXiv.astro-ph/9509079

Schaerer, D. 2002, A&A, 382, 28, doi: 10.1051/0004-6361:20011619

Schaerer, D., Marques-Chaves, R., Xiao, M., & Korber, D. 2024, A&A, 687, L11, doi: 10.1051/0004-6361/202450721

Scholtz, J., D'Eugenio, F., Maiolino, R., et al. 2026a, arXiv e-prints, arXiv:2603.22277, doi: 10.48550/arXiv.2603.22277

Scholtz, J., Carniani, S., Parlanti, E., et al. 2026b, MNRAS, 549, stag939, doi: 10.1093/mnras/stag939

Schwarz, G. 1978, Annals of Statistics, 6, 461

Senchyna, P., Plat, A., Stark, D. P., et al. 2024, ApJ, 966, 92, doi: 10.3847/1538-4357/ad235e

Senchyna, P., Stark, D. P., Charlot, S., et al. 2021, MNRAS, 503, 6112, doi: 10.1093/mnras/stab884

Senchyna, P., Stark, D. P., Charlot, S., et al. 2022, ApJ, 930, 105, doi: 10.3847/1538-4357/ac5d38

Shapley, A. E., Steidel, C. C., Pettini, M., & Adelberger, K. L. 2003, ApJ, 588, 65, doi: 10.1086/373922

Shi, Y., Dai, L., Murray, N., et al. 2026, ApJ, 997, 309, doi: 10.3847/1538-4357/ae3150

Shore, S. N., & Wahlgren, G. M. 2010, A&A, 515, A108, doi: 10.1051/0004-6361/201014271

Sigut, T. A. A., & Pradhan, A. K. 2003, ApJS, 145, 15, doi: 10.1086/345498

Sigut, T. A. A., Pradhan, A. K., & Nahar, S. N. 2004, ApJ, 611, 81, doi: 10.1086/422027

Singh Rai, R., & Roberts-Borsani, G. 2026, arXiv e-prints, arXiv:2608.10063. https://arxiv.org/abs/2608.10063

Sądowski, A., & Narayan, R. 2016, MNRAS, 456, 3929, doi: 10.1093/mnras/stv2941

Smith, L. J., Crowther, P. A., Calzetti, D., & Sidoli, F. 2016, ApJ, 823, 38, doi: 10.3847/0004-637X/823/1/38

Sneppen, A., Matthews, J. H., Watson, D., et al. 2026a, arXiv e-prints, arXiv:2604.09399, doi: 10.48550/arXiv.2604.09399

Sneppen, A., Watson, D., Matthews, J. H., et al. 2026b, arXiv e-prints, arXiv:2601.18864, doi: 10.48550/arXiv.2601.18864

Sok, V., Nelson, E. J., Begelman, M. C., et al. 2026, arXiv e-prints, arXiv:2606.23778, doi: 10.48550/arXiv.2606.23778

Steidel, C. C., Erb, D. K., Shapley, A. E., et al. 2010, ApJ, 717, 289, doi: 10.1088/0004-637X/717/1/289

Steidel, C. C., Strom, A. L., Pettini, M., et al. 2016, ApJ, 826, 159, doi: 10.3847/0004-637X/826/2/159

Sun, W. Q., Naidu, R. P., Matthee, J., et al. 2026, The Open Journal of Astrophysics, 9, 62505, doi: 10.33232/001c.162505

Tacchella, S., Eisenstein, D. J., Hainline, K., et al. 2023, ApJ, 952, 74, doi: 10.3847/1538-4357/acdbc6

Tang, M., Stark, D. P., Chevallard, J., et al. 2021, MNRAS, 501, 3238, doi: 10.1093/mnras/staa3454

Tang, M., Stark, D. P., Mason, C. A., et al. 2026a, ApJ, 1001, 38, doi: 10.3847/1538-4357/ae4edb

Tang, M., Stark, D. P., Topping, M. W., Mason, C., & Ellis, R. S. 2024, ApJ, 975, 208, doi: 10.3847/1538-4357/ad7eb7

Tang, M., Stark, D. P., Plat, A., et al. 2025, ApJ, 991, 217, doi: 10.3847/1538-4357/adfd57

Tang, M., Stark, D. P., Mason, C. A., et al. 2026b, arXiv e-prints, arXiv:2604.03563, doi: 10.48550/arXiv.2604.03563

Taylor, A. J., Finkelstein, S. L., Kocevski, D. D., et al. 2025, ApJ, 986, 165, doi: 10.3847/1538-4357/add15b

Telfer, R. C., Zheng, W., Kriss, G. A., & Davidsen, A. F. 2002, ApJ, 565, 773, doi: 10.1086/324689

Topping, M. W., Shapley, A. E., Reddy, N. A., et al. 2020, MNRAS, 495, 4430, doi: 10.1093/mnras/staa1410

Topping, M. W., Stark, D. P., Senchyna, P., et al. 2024, MNRAS, 529, 3301, doi: 10.1093/mnras/stae682

Topping, M. W., Sanders, R. L., Shapley, A. E., et al. 2025a, MNRAS, 541, 1707, doi: 10.1093/mnras/staf903

Topping, M. W., Stark, D. P., Senchyna, P., et al. 2025b, ApJ, 980, 225, doi: 10.3847/1538-4357/ada95c

Torralba, A., Matthee, J., Pezzulli, G., et al. 2026a, A&A, 707, A75, doi: 10.1051/0004-6361/202557537

Torralba, A., Matthee, J., Pezzulli, G., et al. 2026b, A&A, 705, A147, doi: 10.1051/0004-6361/202555596

Treiber, H., Greene, J. E., Weaver, J. R., et al. 2025, ApJ, 984, 93, doi: 10.3847/1538-4357/adc38f

Tripodi, R., Martis, N., Markov, V., et al. 2025a, Nature Communications, 16, 9830, doi: 10.1038/s41467-025-65070-x

Tripodi, R., Bradač, M., D'Eugenio, F., et al. 2025b, ApJL, 994, L6, doi: 10.3847/2041-8213/ae13a9

Umeda, H., Ouchi, M., Nakajima, K., et al. 2026, arXiv e-prints, arXiv:2607.15515, doi: 10.48550/arXiv.2607.15515

Valentino, F., Heintz, K. E., Brammer, G., et al. 2025, A&A, 699, A358, doi: 10.1051/0004-6361/202553908

Vanden Berk, D. E., Richards, G. T., Bauer, A., et al. 2001, AJ, 122, 549, doi: 10.1086/321167

Vanzella, E., Caminha, G. B., Calura, F., et al. 2020, MNRAS, 491, 1093, doi: 10.1093/mnras/stz2286

Verhamme, A., Schaerer, D., & Maselli, A. 2006, A&A, 460, 397, doi: 10.1051/0004-6361:20065554

Vestergaard, M., & Wilkes, B. J. 2001, ApJS, 134, 1, doi: 10.1086/320357

Vidal-García, A., Charlot, S., Bruzual, G., & Hubeny, I. 2017, MNRAS, 470, 3532, doi: 10.1093/mnras/stx1324

Vink, J. S. 2023, A&A, 679, L9, doi: 10.1051/0004-6361/202347827

Viotti, R., Rossi, L., Cassatella, A., Altamore, A., & Baratta, G. B. 1989, ApJS, 71, 983, doi: 10.1086/191405

Virtanen, P., Gommers, R., Oliphant, T. E., et al. 2020, Nature Methods, 17, 261, doi: 10.1038/s41592-019-0686-2

Vladilo, G., Centurión, M., Bonifacio, P., & Howk, J. C. 2001, ApJ, 557, 1007, doi: 10.1086/321650

Wang, B., Leja, J., de Graaff, A., et al. 2024, ApJL, 969, L13, doi: 10.3847/2041-8213/ad55f7

Wang, B., Leja, J., Katz, H., et al. 2026, ApJ, 1003, 10, doi: 10.3847/1538-4357/ae5bab

Watanabe, K., Ouchi, M., Nakajima, K., et al. 2026, arXiv e-prints, arXiv:2603.21570, doi: 10.48550/arXiv.2603.21570

Weymann, R. J., Morris, S. L., Foltz, C. B., & Hewett, P. C. 1991, ApJ, 373, 23, doi: 10.1086/170020

Williams, C. C., Alberts, S., Ji, Z., et al. 2024, ApJ, 968, 34, doi: 10.3847/1538-4357/ad3f17

Wills, B. J., Netzer, H., & Wills, D. 1985, ApJ, 288, 94, doi: 10.1086/162767

Wofford, A., Leitherer, C., Chandar, R., & Bouret, J.-C. 2014, The Astrophysical Journal, 781, 122, doi: 10.1088/0004-637X/781/2/122

Xiao, M., Oesch, P. A., Bing, L., et al. 2025, A&A, 700, A231, doi: 10.1051/0004-6361/202554361

Xu, X., Heckman, T., Henry, A., et al. 2022, ApJ, 933, 222, doi: 10.3847/1538-4357/ac6d56

Xu, X., Henry, A., Heckman, T., et al. 2023a, ApJ, 943, 94, doi: 10.3847/1538-4357/aca89a

Xu, X., Heckman, T., Henry, A., et al. 2023b, ApJ, 948, 28, doi: 10.3847/1538-4357/acbf46

Yang, D., Hennawi, J. F., Bosman, S. E. I., et al. 2026, arXiv e-prints, arXiv:2608.18212, doi: 10.48550/arXiv.2608.18212

Yue, M., Eilers, A.-C., Ananna, T. T., et al. 2024, ApJL, 974, L26, doi: 10.3847/2041-8213/ad7eba

Zhang, J., Egami, E., Sun, F., et al. 2026, ApJ, 997, 250, doi: 10.3847/1538-4357/ae2681

Zhang, L., Stone, J. M., Mullen, P. D., et al. 2025, ApJ, 995, 26, doi: 10.3847/1538-4357/ae0f91